Development and Modeling of Multi-scale Continuous High Gradient Magnetophoretic Separator for Malaria-infected Red Blood Cells

Submitted in partial fulfillment of the requirements for

the degree of

Doctor of Philosophy

in

Biomedical Engineering

Andrea Blue Martin

B.S., Bioengineering, University of Pittsburgh (2012)

Carnegie Mellon University
Pittsburgh, PA

May, 2017

ABSTRACT

According to the World Health Organization, nearly 3.2 billion people are at risk of malaria. The most deadliest form of human malaria is caused by the pathogen Plasmodium falciparum, which has claimed over 400,000 lives worldwide in 2015[1]. Even when optimally treated with drug and donor blood therapies, severe malaria has a high mortality rate. The parasites target a patient's red blood cells and convert them into paramagnetic units before eventually rupturing the host cell, further spreading the infection. Combination drug therapies using quinine and artemisinin derivatives are common but are either expensive or have associated toxicities from mis-dosing. Moreover, antimalarial drugs are becoming increasingly ineffective against the growing number of drug-resistant malaria strains. Combination drug and blood exchange therapies are often implemented to flush out malaria-infected red blood cells (iRBC) but consume a great quantity of donor blood, carry a high risk of transmitting other blood-borne diseases, and have no agreed upon advantage or disadvantage among clinicians. Due to the relative disadvantages of other treatment methods, small scale high gradient magnetic separation (HGMS) devices, used in a variety of biological applications, may be another treatment option to consider. mPharesis ("magnetic apheresis") is a proposed low-cost, disposable magnetic blood filtration device which continually removes iRBCs from a patient's whole blood by capitalizing on the iRBC's unique magnetic properties. The proposed treatment-scale system will provide emergency care with parameters similar to continuous hemofiltration systems in terms of blood flow rates (up to approximately 500 mL min^{-1}), vascular access, and treatment times (up to about 3 hours).

A novel medium-scale high gradient magnetic separation device is detailed here. The device consists of a disposable photo-etched embedded wire array and acrylic layered housing on an external permanent magnet set. The magnetic force and flow field design were computationally optimized. In-vitro feasibility experiments were conducted at several flow rates and physiological hematocrits (Hct) using a blood mixture composed of healthy RBCs and a non-pathogenic paramagnetic blood analog called methemoglobin RBCs (metRBCs). The device was able to selectively remove paramagnetic RBCs

without excessive loss of healthy RBCs. Simplified experiments were performed with 30% Hct with 20% metRBCs. At steady state, the concentration of metRBCs was reduced by 27.0±2.2% in a single pass at a flow rate of 77 μL min^{-1} as compared to 1.6±0.7% in control experiments without a magnet present. The experimental paramagnetic RBC removal rate was over 380 times greater than similar published HGMS devices.

These successful results were applied to a theoretical transport model. The model was designed to compare the parasite removal and Hct level changes between combination drug and exchange transfusion (ET) therapy versus treatment-scale mPharesis-drug therapy. When the mPharesis flow rate was set to typical continuous dialysis rates, treatment times and donor blood volumes were reduced for all 10 cases. Calculated treatment times were all less than 60% of the reported ET-drug treatments, with times ranging from 47 to 71 minutes. The mPharesis-drug treatment was calculated to need between 4% and 53% less donor blood than the reported ET-drug treatments. Between 775 and 1772 mL of packed donor RBCs (3 to 6 units of whole blood) were estimated for the mPharesis-drug treatments, versus the average 5 to 20 units used during ET[2]. Treatment reference charts were generated to provide time and donor blood volume estimates for a range of patient sizes and disease severities. Based on the maximum flow rate of 500 mL min^{-1}, a treatment-scale mPharesis system was estimated to be the size of three stacked briefcases, which is a feasible size for deployment in a clinical setting.

Finally, the design, fabrication, and microscopic visualization of a simple, benchtop-fabricated continuous HGMS device was detailed. This proof-of-concept microfluidic device was implemented to test the effect of hematocrit and flow rate on the separation of mixtures of metRBCs (heat-treated and un-heated) and transparent ghost RBCs. An automated image processing protocol provided feasible cell concentration profiles for each flow and rheological condition with a 6.5 to 9.7% lower sum than manual counting for three samples. For the no magnet conditions, the average near-magnet concentration of paramagnetic RBCs at the outlet (within 10% of 130 μm channel height adjacent to the wire array) was between 1.3 and 2.4 times greater than the average of the rest of the flow field (degree of separation, DOS). The most

effective separation was found to occur at the lowest flow rate 0.4 μL min^{-1} and with the 0.5% Hct metRBC sample with DOS=26. The addition of 30% ghost RBCs reduced the efficiency for all flow rates, with DOS=7.4 for best flow rate of 0.4 μL min^{-1}. Heat treatment did not significantly affect separation with DOS=7.3, likely due to the low impact of the relatively low concentration of metRBCs (0.5%).

The mesoscale fabrication and design process, clearance model, cell counting algorithm, and HGMS fabrication protocol and microscopy study described in this thesis provides a useful framework for future HGMS optimization and the further development of a clinical treatment system for severe malaria patients with often limited treatment options.

ACKNOWLEDGEMENT

I would like to thank Dr. James Antaki, is my thesis advisor, for seeing potential in me so many years ago. With him, I have learned countless talents, subject matters, and a totally new and amazing way of solving problems. He has helped me find answers to the endless problems I faced with fascinating, and often surprising, solutions. And, course of, it is because of him that I was able to walk the halls as a proud CMU graduate student for so many years. I am incredibly grateful to my committee members Drs. Keith Cook, Mehrdad Massoudi, and Marina Kameneva: Dr. Cook for his medical device knowledge and piles of useful lab tools, Dr. Massoudi for patiently help me understand the constitutive side of the engineering world, and Dr. Marina Kameneva, and her students, for teaching me absolutely everything I know about blood rheology.

I thank Dr. Alberto Gandini with AccelDiagnostics for whom gave life to this whole project with a unique idea years ago. Thank you Dr. Wei-tao Wu for your invaluable CFD knowledge and giving me some awesome design results. Special thanks to Dr. Joie Marhefka who has been with me throughout my entire research career, giving me advice and her friendship through the toughest spots.

I also wish to thank the Department of Biomedical Engineering in CMU and Dr. Yu-li Wang for giving me the chance to pursue my PhD study at the best university in the world.

Finally, this work was supported by NIH grant 1 R01 HL089456.

TABLE OF CONTENTS

LIST OF FIGURES

LIST OF TABLES

NOMENCLATURE

BAR	blood access rate
CFD	computer fluid dynamics
deoxyRBC	deoxygenated RBC
DOS	degree of separation
ET	exchange transfusion
FFP	fresh frozen plasma
Hct	hematocrit
HGMS	high gradient magnetic separator
hRBC	healthy red blood cell
iRBC	malaria infected red blood cell
metRBC	methemoglobin-containing red blood cell
mP	mPharesis
P.	*Plasmodium*
Para	parasitemia
PBS	phosphate-buffered saline
PM	permanent magnet
PRR	parasite reduction ratio
PVR	packed volume ratio
RBC	red blood cell
SD	standard deviation
SR	split ratio
WHO	World Health Organization

1 INTRODUCTION

Malaria, caused by the protozoan parasite *Plasmodium,* infects 300-500 million people worldwide and causes an estimated half a million deaths annually[1]. Of the four types of human malaria species, *Plasmodium (P.) falciparum* is the most deadly. Severe falciparum malaria leads to a poor prognosis in African children under 5 years old, non-immune travelers, and pregnant women. Infected patients present symptoms such as impaired consciousness, repeated convulsions, respiratory distress, substantial bleeding, organ failure, and shock which often leads to death within 6 hours of hospital admission[3,4]. The membrane of the infected host red blood cells becomes rigid and will adhere to capillary endothelium, compromising microcirculation[3–6]. Late-stage infected red blood cells (iRBCs) sequester in neural capillary bed (cerebral malaria) leading to encephalopathy, coma, and approximately 20% mortality of children and adults[7–10].

Combination drug therapies using quinine and artemisinin derivatives are common but are expensive, have an associated toxicities from mis-dosing. Drug therapies are becoming increasingly ineffective due to the rising number of drug-resistant malaria strains[11,12]. Combination drug and blood exchange therapies are implemented to rapidly reduce parasite load and attempt to resolve malaria-induced anemia. Exchange transfusion (ET) is used also flush out the sequestered late-stage iRBC "sludge" from the microvasculature while preventing younger iRBCs from sequestering[14]. However, blood exchanges are expensive and risk fluid overload, immune reactions in patients, and transmission of other blood-borne diseases. Clinical studies and retrospective reports cannot agree as to whether there is a clear advantage or disadvantage to using ET with severely ill malaria patients[2,13–22]. During *P. falciparum*'s 48 hour intra-erythrocytic cycle, the parasite feeds off the host RBC's protein and iron-rich hemoglobin for nourishment. The parasite produces a weakly magnetic (paramagnetic) crystal byproduct, called hemozoin, which imparts paramagnetic properties to the iRBC[23–25].

In research settings, various methods have been designed to concentrate and synchronize paramagnetic targets such as *E. coli*, healthy RBCs, iRBCs, and sexual *P. falciparum* stages[26–39]. However, all of these

methods have a low throughput and require additives. This thesis aims to develop a continuous high gradient magnetophoretic separation (HGMS) device to selectively remove iRBCs from blood at physiological concentrations without additives. The strong magnetic force is generated by an external permanent magnet set and an embedded ferromagnetic wire array adjacent to the blood flow path. The resulting proof-of-concept prototype has demonstrated a high paramagnetic RBC removal throughput. These results were scaled into a theoretical treatment-sized system with a corresponding iRBC clearance model to compare the system's performance against reported clinical combination ET-drug therapy. A miniaturized HGMS device was also developed to provide microscopic visualization of the mPharesis flow field in real time with different rheological conditions. The combined efforts detailed in this thesis offer significant progress towards future clinical implementation. The specific aims of this thesis are as follows:

Specific Aim 1: Develop a mesoscale continuous magnetophoretic separator for malaria-infected red blood cells

A novel mesoscale (medium scale) HGMS device was designed, fabricated and verified. The magnetic force field was maximized using magnetic modeling software for a given wire array and commercially available high strength permanent magnet sets. The blood flow path was optimized with computational fluid dynamic (CFD) simulations to ensure homogeneous flow at a creeping rate. Optimized features included the inlet and outlet manifolds, magnetic separation area, and the waste collection exit width. A non-pathogenic paramagnetic iRBC analog (methemoglobin-containing RBCs) was used for micro and mesoscale experiments. A simple, easily repeatable fabrication protocol was developed to enable quick iterative design changes with respect to micron-scale surface smoothness and flow field homogeneity. The final device was verified experimentally using a mixture of heathy RBCs and metRBCs to represent the average parasite load for a severely infected-malaria patient.

Specific Aim 2: Perform simulations to compare the parasite clearance and hemodilution with combination Exchange Transfusion-drug and mPharesis-drug therapies

A theoretical, compartmental model was developed to compare the parasite clearance and Hct level changes between combination ET-drug therapy and a treatment-scale mPharesis system combined with drug therapy. The model was calibrated and compared to 10 case studies of severe malaria patients successfully treated with ET-drug therapies. Reference tables were generated to enable quick reference to treatment times and donor blood volumes for a range of patient sizes and disease severities. This analysis provided insights for desiring a treatment-scaled system.

Specific Aim 3: Perform a parametric study of key rheologic and fluid dynamic factors affecting the efficiency of HGMS with paramagnetic red blood cells using a novel HGMS device

An inexpensive, benchtop-fabricated continuous HGMS device fabrication protocol was developed. A series of in-vitro microfluidic studies were performed to quantify the effect of various rheological parameters on the continuous separation of paramagnetic RBCs. Proof-of-concept experiments were performed using mixtures of metRBCs and transparent ghost RBCs, at various flow rates, hematocrits (Hct), and metRBC membrane stiffening by heat treatment. An automated image processing protocol was implemented to analyze the videos.

2 BACKGROUND

2.1 Malaria Epidemic

Malaria continues to be a devastating global burden. An estimated 438,000 deaths were reported in 2015 by the World Health Organization in almost 100 countries[1]. Humans can be infected by four protozoan parasite species: *P. falciparum, P. vivax, P. ovale* and *P. malariae* with falciparum malaria causing the majority of reported deaths. The disease is transmitted by the bite of infected female anopheline mosquitoes (Figure 1). During the mosquito's blood meal, sporozoites enter into the host's bloodstream. Within an hour, the sporozoites enter hepatocytes and begin to divide mitotically into asexual blood-stage merozoites which then enter circulation to infect the host's red blood cells (RBCs). During the 48 hour intra-erythrocytic life cycle, the parasite develops into early ring-shaped trophozoites, enlarges into a metabolic trophozoite, followed by several rounds of nuclear division without cytokinesis into schizonts, which then bud into multiple daughter merozoites. Finally, the daughter merozoites rupture the host RBC and subsequently invade new RBCs in the next blood cycle. In nonimmune humans, the infection is amplified about 20-fold each cycle. The malaria infected host red blood cell (iRBC) maintains osmotic and membrane stability throughout this cycle[40]. After several cycles, some of the merozoites divide meiotically into non-symptomatic sexual gametocytes and are picked up by the next biting mosquito[10].

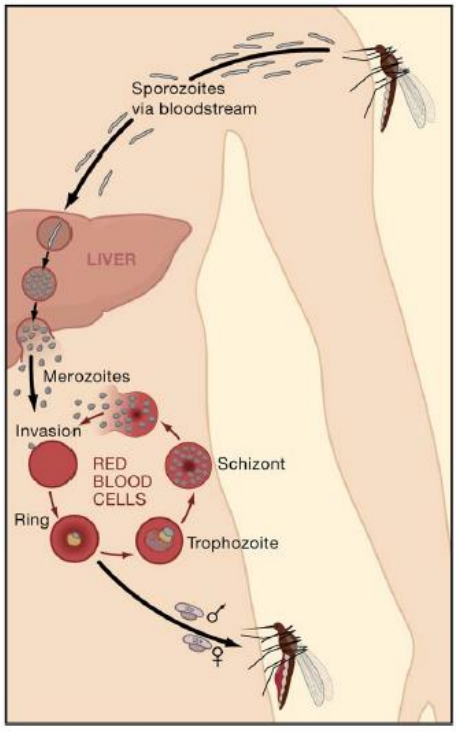

Figure 1. Life cycle of *P. falciparum* malarial parasite[40].

Indigenous mosquito-driven falciparum malaria infection is most common, but the disease can be transmitted via infected blood products or by congenital transmission. In developed countries, most malaria cases occur among travelers, immigrants, or military personnel returning from areas endemic for malaria. With more than

200,000 cases of fetal loss and more than 10,000 maternal deaths reported annually, children under 5 years old and pregnant women are most at risk[41]. Infected patients most often experience fever, impaired consciousness, anemia, repeated convulsions, respiratory distress, substantial bleeding, organ failure, and shock[16,21]. These symptoms are mostly caused by red blood cell morphological changes, such progressively increased membrane rigidity, shape changes, and "stickiness" to capillary endothelium. During its intra-erythrocytic stage, the parasite grows and the host RBC becomes near spherical in shape. The host red blood cell loses deformability due to decreased elasticity of the membrane's spectrin scaffolding caused by chemical factors excreted by the parasite[42]. The membrane surface becomes more reactive to other surfaces and will often form stable "knob-like" structures that are antigenically different than healthy cells[43]. Late-stage iRBCs sequester in neural capillary beds, referred to as cerebral malaria, leading to encephalopathy, coma, and approximately 20% mortality of children and adults[7–10].

2.2 Current treatments for severe falciparum malaria

2.2.1 Treatment Limitations in Endemic Regions

The standard method for diagnosing malaria is light microscopy of thick and thin stained blood smears[44]. Thin smears allow for assessment of *Plasmodium* species while thick smears are more sensitive at detecting the degree of the malaria infection. However, because blood smear diagnosis requires trained personnel and expensive equipment, there has been a growing interest in developing Rapid Diagnostic Tests (RDTs) for malaria. RDTs are a new and evolving technology in endemic regions, but are often ineffective due to user errors. Quality assurance with RDT production is still a prevalent issue[10,45].

Most malaria endemic regions lack comprehensive medical treatment facilities. A visit to The Gambia in 2012 by two members of my lab (Dr. Molly Blank and Jaqueline Bracket) confirmed this sentiment; the country's largest, most sophisticated medical facility visibly suffered from staffing, technical, and supply limitations. The photo shown in Figure 2 is of a filthy delivery room in a maternity clinic, not an uncommon sight in many developing countries. Often, complex surgeries and cancer patients are referred to neighboring countries due to a lack of sufficient lab equipment and expertise. Many of these referred

patients will never seek the necessary treatment and are left without any other feasible treatment options. If a patient has enough money to pay for private care, scarcely available private practitioners still may decline treatment due to post-operative risks. Infrastructural issues, such as loss of electrical power, are common. The need for bed-sharing among pediatric patients often leads to cross-contamination. Nurses must often clean equipment by hand with soap, water, and ethanol, which is time-consuming and ineffective against most diseases. Pathogen-free blood supplies for transfusion are in constant shortage. The true underlying issue with these patients is not necessarily the treatment of their severe malaria, but rather effectively treating these people before their illness passes the "point of no return," leading to a preventable death.

Figure 2. A delivery room at a high traffic hospital in The Gambia (photo courtesy of Molly Blank).

These first-hand observations in The Gambia provided invaluable insight into what must be considered to successfully design and implement a new treatment system in these malaria endemic regions. The system must minimize electricity usage and be simple, inexpensive, and disposable to avoid sterility issues. These considerations were upheld during the development of this thesis work.

2.2.2 Drug Therapies for Malaria

Intravenous and oral quinine is currently the most widely used agent in the treatment of severe falciparum malaria and has been used for over a century. Quinine acts by binding to hemozoin crystal faces like a cap[46]. By inhibiting hemozoin growth, toxic heme builds up and eventually kills the parasite. However, quinine and its derivatives are difficult to dose and often lead to toxicity in patients[47]. Quinine overdosing may cause cardiac arrhythmias, hypotension, blindness, deafness, and hyperinsulinemic hypoglycemia[48]. Artemisinin and its derivatives is more modern drug type, is well tolerated in patients, and recently has become more commonly given due to its effectiveness at killing the falciparum malaria parasite[49]. In cell

free conditions, artemisinin forms covalent bonds with free heme, inhibiting hemozoin formation, and thus leading to the parasite's death[46]. At present, combination drug therapies featuring artemisinin derivatives are recommended for treatment of quinine-resistant falciparum infections. Side effects include nausea, vomiting, skin itchiness, and fever; however, unlike quinine therapies, bleeding and cardiac arrhythmias rarely occur. A greater problem is the emergence of artemisinin-resistant strains of the malaria parasite, which have been reported in Southeast Asia[11,12]. One study showed 20% of 80 severely infected malaria patients in western Cambodia and northern Thailand. Patients were treated with a standard artemisinin which failed to reduce parasitemia to manageable levels after 4 days compared to the normal maximum two day period[11]. Another study showed the half-life of the same artemisinin-resistant parasite strains is almost four times greater than sub-Saharan strains[12]. For these reasons, additional treatment methods often must be considered for severely ill malaria patients.

2.2.3 Exchange Transfusions

Exchange transfusion (ET, also referred to as erythrocytapheresis or red cell exchange) was introduced in 1974 as an addition to drug therapy for the most severe cases of malaria infection[50]. ET can be automated or manual and uses a combination of packed RBCs, fresh frozen platelets (FFP), or whole blood. ET is effective in alleviating malaria-induced anemia and often rapidly reduces parasite load. This treatment is thought to "flush out" the sequestered iRBCs "sludge" from the microvasculature while preventing younger iRBCs from sequestering[2]. ET is also believed to remove the inflammatory mediators and cytotoxins that stiffen healthy RBCs in plasma[3,51]. However, blood exchanges require a great amount of donor blood which is a scarce commodity in many under-resourced locations. ET also carries risks of fluid overload, immune reactions in patients, and transmission of other blood-borne diseases[17]. Blood exchange is often only available to patients in western countries where cross-matched and pathogen-free blood products are available[20].

Despite the long history of ET, there still remains a controversy as to its effectiveness. The World Health Organization stated "there is no consensus on the indications, benefits and dangers involved, or on

practical details such as the volume of blood that should be exchanged. It is therefore not possible to make any recommendation regarding the use of exchange blood transfusion."[52] Several groups have published positive clinical results with ET with respect to mortality and consistent decreases in parasitemia (up to 90% decrease) when compared to controls[2,13,19,21,53–59]. However, numerous clinical groups have found no clear advantage or disadvantage with combination ET-drug therapies[14–16,18,22,60]. In a retrospective study, Burchard et al. evaluated 61 cases of severe malaria patients treated successfully with ET. They found no clear benefit using large volumes of blood during ET to attempt to clear the disease compared to patients who survived with drug therapy and smaller blood transfusion volumes, enough to alleviate anemia, alone[61]. The rate of failure could be in fact greater since it is possible that clinicians do not publish when patients died with combination ET-drug therapies.

2.3 Paramagnetic Properties of Malaria Red Blood Cells

When drug and ET therapies prove ineffective, there is another potential treatment solution for severely infected patients by capitalizing on a unique property of iRBCs. During the parasite's intra-erythrocytic asexual stage, the parasite digests up to 80% of the host red blood cell's iron-rich hemoglobin to satisfy its metabolic needs[62]. The parasite oxidizes hemoglobin (HbO_2) low spin ferrous form (Fe^{2+}) to a high spin ferric form (Fe^{3+}) called heme. The free heme, which is highly toxic to the parasite, is then restructured into an iron crystal called hemozoin (Figure 3). Before the parasite causes the host RBC to rupture, hemozoin imparts a paramagnetic property to the cell[23–25]. This phenomena was first published in 1946 when malaria infected RBCs were concentrated from whole blood using a simple experiment of placing a large external permanent magnet adjacent to a capillary tube[63]. This unique property can be capitalized upon to create a novel magnetic treatment system.

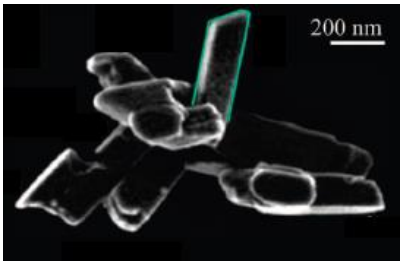

Figure 3. Scanning electron microscopy micrograph of hemozoin crystals purified from *P. falciparum*[127].

2.4 Magnetic Separators

Selective separation of cells and pathogens is critical in numerous medical and microbiological applications such as

bulk water purification[64], cancer cell detection[26], and apheresis of paramagnetic cells like iRBCs[65]. Magnetic separators offer the advantage of a concentrating paramagnetic targets using a large, non-hydrolytic separation forces without the use of additives. Non-magnetic cells or pathogens like *E. coli*, fungi, or CD4 cancer cells can be separated magnetically by first conjugating them to magnetic nano- and microparticles[26–39].

The separation efficiency of a magnetic separator is related to the strength of the applied magnetic force. Macroscale magnetophoretic separators, in which the sole source of magnetic force is a centimeter or larger, can generate small forces over great distances and are useful for capturing highly magnetic targets. Some targets include ferromagnetic metal sludge in waste water purification[64] or superparamagnetic magnetic particles with magnetic susceptibilities in the range of 10^2 to 10^6 (SI units)[66–72]. While these macroscale separators can attract macro-size, ferromagnetic objects over relative large distances, they are ineffective on weak magnetic targets such as deoxyRBCs, which are 1000 times less susceptible than magnetic microparticles of similar size.

High gradient magnetic separators (HGMS) utilize a combination of large external permanent magnets and secondary micron-sized ferromagnetic pole structures such as beads and wires to focus or concentrate the magnetic flux. MetRBCs and late stage iRBCs are often concentrated using HGMS in batches with capture-rinse cycles. The source of strong magnetic force can be an external permanent magnet with a single ferromagnetic wire, steel wool packed columns, magnetic bead-packed MACs columns (Miltenyi Biotec Inc., San Diego, CA, USA), or micro-patterned ferromagnetic metal shapes[23,25,73–81]. Though the capture percentage of these devices can be greater than 90%, they are limited due to hemodilution (from the rinse step), sterility and fouling issues, and low throughput. Also, these batch devices are not ideal to capture early-stage ring iRBCs, which are less paramagnetic than late stage iRBCs, as the ferromagnetic elements are unable generate sufficient magnetic force to overcome the shear force due to flow[82]. Using smaller particles (compared to the approximately 200 μm sized MAC beads) to amplify the magnetic force leads to smaller inter-spatial voids which generate large amounts of hemolytic shear stresses. This

was experienced in pilot studies using metRBCs and a 5 mL syringe packed with S70 steel shot (approximately 175 μm diameter, Kramer Industries, Inc., Piscataway, NJ, USA) and smooth spherical ferrite beads (40 μm, and 100 μm, Powdertech International, Valparaiso, IN, USA).

Continuous HGMS devices offer the advantage of increased throughput, continuous processing, and minimal fouling. In these continuous systems, the shape, placement, and inclusion of the secondary ferromagnetic elements directly adjacent to the flow field is essential for effective magnetic separation. Due to micron-scale fabrication limitations, the production of quality continuous microfluidic HGMS systems is laborious and expensive. The ability to view HGMS systems via microscopy, which is valuable for research and optimization purposes, is an additional fabrication challenge. In HGMS devices, opacity is greatly diminished by magnets and secondary ferromagnetic elements adjacent to the flow field. The above challenges are addressed as part of the research reported in this thesis.

2.5 Problem Statement

A continuous HGMS device which efficiently and selectively removes paramagnetic RBCs from whole blood has great potential to be applied to a clinical apheresis system for severely malaria-infected patients. To our knowledge, no published HGMS device can selectively remove paramagnetic RBCs at a sufficient throughput or physiological concentration for potential clinical application. There is a need for the development of a mesoscale HGMS device that can readily be scaled into a treatment system. Our target user is a severely ill malaria infected patient for whom drug therapy has failed and the amount of donor blood needed for ET exceeds what is available.

2.6 Design Specifications: Objectives and Constraints

A novel magnetic apheresis (mPharesis) device for selective removal of iRBCs from whole blood is described here. In this study, a scalable, low-cost, benchtop-fabricated mesoscale device for magnetophoretic extraction of paramagnetic RBCs has been designed and fabricated. For mPharesis to be clinically useful and usable, several challenges must be met. The amount of donor blood needed must be

less than is needed for ET. The system will have similar treatment times and blood access flow rates as hemofiltration continuous renal replacement therapy (CRRT), which is up to 3 hours at a rate of 500 mL min^{-1} for an average adult[83]. Additionally, the system should produce shear stresses significantly less than the critical threshold for hemolysis, which was measured in vitro as approximately 150 Pa[84] (estimated in mesoscale). It must use very little electricity, possibly provided by a small long-lasting battery. The total system should be of comparable size, or smaller, than common CRRT systems which are approximately the size of a water cooler.

3 Develop a Mesoscale Continuous Magnetophoretic Separator for Malaria-infected Red Blood Cells

3.1 Introduction

Continuous HGMS devices reported by several research groups feature various designs in order to capture paramagnetic targets. All HGMS microfluidic devices reported to date have a low throughput, only processing several microliters of diluted blood a minute. This gap in technology motivated Dr. Alberto Gandini in 2008 to invent a mesoscale HGMS device, titled mPharesis, for continuous removal of paramagnetic RBCs without use of a saline buffer layer (Figure 4a)[85]. It employs a combination of a precisely designed ferromagnetic wire array and strong external permanent magnet. The patient's infected blood enters through the inlet. The paramagnetic iRBCs are deflected towards the wire array by the magnetic force. The concentrated iRBC layer is then skimmed off by the waste and the remaining filtered blood leaves the outlet. The design is shown in Figure 4b. This concept was the basis for the mPharesis device developed in this project. The mesoscale device developed in this aim will maximize flow field width with considerations for flow field fabrication restrictions and commercially available permanent magnet availability. Our treatment system must selectively remove iRBCs without excessive loss of healthy blood (i.e. no increase in concentration of healthy RBCs in waste drainage). The paramagnetic RBC removal rate must be significantly greater than similar devices (i.e. more than 100 times greater)[65,86,87].

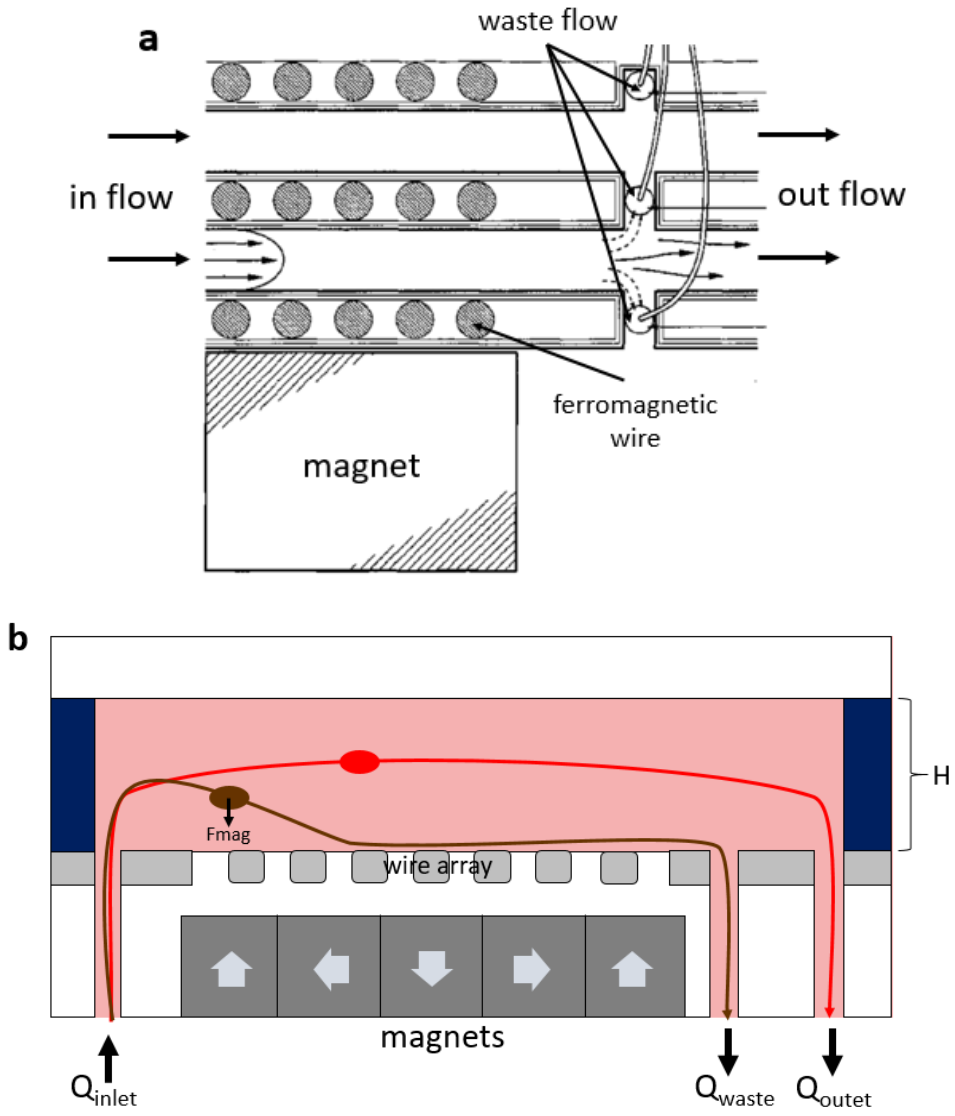

Figure 4. a) Original mPharesis patent concept[85]. b) Current design diagram, the heathy RBCs are red and paramagnetic iRBCs are brown.

H is the height of the flow path. Q is the flow. The ratio between Q_{waste}:Q_{inlet} is the split ratio (SR) which determines what percentage of the flow field height was skimmed off via the waste exit.

3.2 Materials and Methods

3.2.1 Magnetic Force Description

An objective for this HGMS device was to create a large magnitude magnetic force across the entire flow field width and length. The force should also be large enough to capture iRBCs across the full height of

the flow path which has a minimum constraint due to fabrication limitations. A large and far reaching magnetic force are contradicting objectives. When magnetic flux is highly concentrated from a small magnetic source (i.e. very small ferromagnetic wire with a permanent magnet), the magnetic field is large at the source's surface but then decreases rapidly. Thus, a large magnitude, very local magnetic force is created. For a larger magnetic source (i.e. a large wire with the same permanent magnet), the field decreases gradually away from the surface. This creates a farther reaching, yet weaker magnetic force. This concept is simulated using a 2D finite element software for magnetic systems called FEMM (QinetiQ North America, Waltham, MA, USA) for a 12.7 mm permanent magnet, a 0.25 mm (30 AWG), and 1.8 mm (14 AWG) nickel wires in Figure 5.

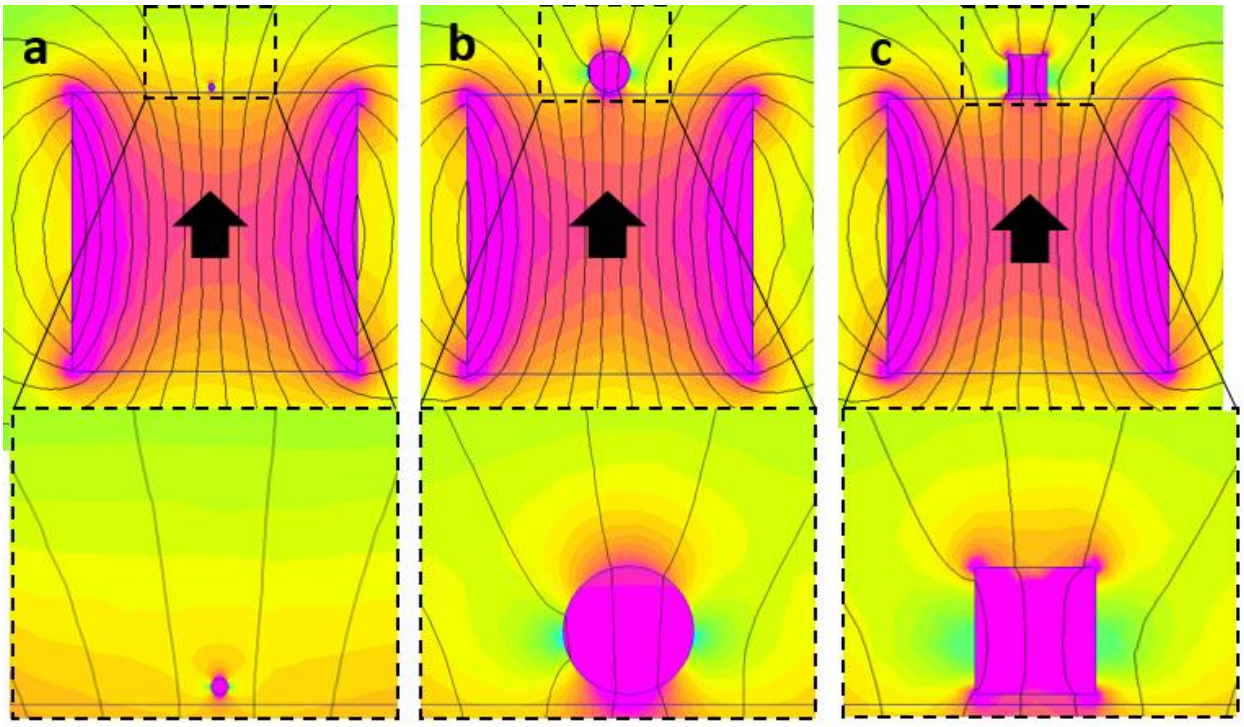

Figure 5. Magnetic field density plots produced in FEMM for a 12.7 mm cube N40 magnet with a) a 0.25 mm (30 AWG) round nickel wire, b) 1.8 mm (14 AWG) round nickel wire, and c) 1.8 mm square nickel wire. Flux density ranges from 0 to 0.73 Tesla (blue to pink). Quick color changes over a short distance indicate strong magnetic force.

Magnetic field is plotted with FEMM with a range of colors and how quickly the colors change across a distance represents magnetic force (i.e. the magnetic gradient). A faster color change means a large magnetic force. The small wire in Figure 5 has a much shorter region of color change than the large wire, thus the force is stronger for the small wire but not as far reaching as the large wire for the same magnetic

flux source. Magnetic flux is most concentrated in sharp corners of magnetic objects, least at flat edges. This is demonstrated in Figure 5 with a 1.8 mm round and square wire where the large square wire, similar to the small wire, produces strong, local magnetic forces at the corners. In addition to geometry considerations, the secondary elements should be made from a highly-permeable ferromagnetic material, such as low carbon steels or ferritic stainless steels. Here, a type 410 stainless steel was chosen for its magnetic property and corrosion resistance. The material does not saturate fully in the given magnetic field and thus was able to concentrate nearly all of the magnetic flux from the permanent magnet set.

The magnetic force produced by a variety of magnet set arrangements was compared. Magnets included neodymium magnets (type N40 K&J Magnetics) with a thickness of 12.7 and 6.3 mm, chosen as the strongest commercially available magnets which could be safely assembled into different configurations by hand. The magnet array arrangements tested included a single 76.2 mm x 12.7 mm, alternating 50.8 mm x 12.7 mm, 12.7 mm x 12.7 mm, and 6.3 mm x 6.3 mm; and Hallbach arrangements of the 12.7 mm and 6.3 mm magnets. Alternating arrays are one way to arrange multiple magnets in parallel. A more homogeneous magnetic field can be generated using a Hallbach array, which features a set of adjacent magnets where each subsequent magnet is rotated 90 degrees from the last (i.e. ↑←↓→↑). With this configuration, the majority of the magnetic flux is directed to one face of the array increasing the flux density, and thus magnetic force, on one face of the array. This theory was confirmed in the results section.

The 60 mm by 60 mm wire array was a photoetched 125 μm thick piece of SS410 with 200 μm wide wires with a 400 μm pitch (Kemac Technology Inc., Azusa, CA, USA) mounted on a 1.5 mm acrylic place against the magnet array. The wire array geometry was chosen based on fabrication availability, limitations, and designs of published HGMS devices[65,86–88]. The various magnet and wire array combinations were processed in FEMM and the magnetic field density (B) was simulated with an example for the single magnet is shown in Figure 6. The simulation was assumed to be symmetric to economize computational cost.

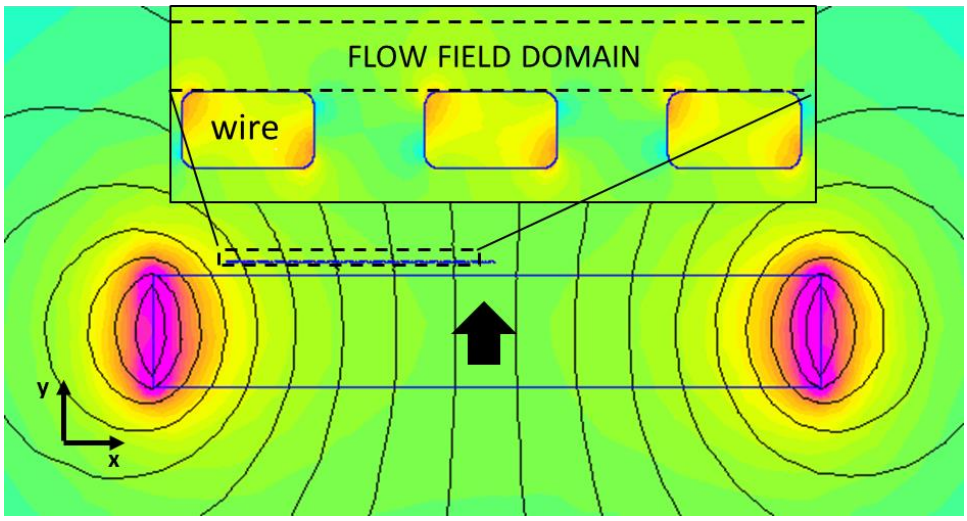

Figure 6. Representation of the magnetic field density field (B) produced in FEMM for the mesoscale HGMS device with a single 76.2 mm x 25.4 mm N40 permanent magnet in cross-section. Flux density ranges from 0 to 0.56 Tesla (blue to pink). The black dash box indicates the flow field domain where magnetic force was calculated.

The simulated B field was discretized into a 5 μm by 5 μm point within the mPharesis flow field domain (100 μm across the entire 60 mm wide wire array) for each magnet arrangement. dB/dx and dB/dy was calculated using the finite difference method. The magnetic force (|grad(B)|) calculated using Equation 1 and was plotted for each array using Matlab (The MathWorks, Inc., Natick, MA, USA).

$$\left|\mathrm{grad}\left(\mathrm{B}(\mathrm{x},\mathrm{y})\right)\right| = \sqrt{\frac{\partial \mathrm{B}}{\partial \mathrm{x}}^2 + \frac{\partial \mathrm{B}}{\partial \mathrm{y}}^2} \qquad [1]$$

The array with the greatest average magnetic force within the flow field domain of interested was chosen.

3.2.2 Flow Manifold Design Optimization

A flow manifold was designed to produce a wide, homogenous flow field (i.e. constant centerline flow velocity across flow field width) within a device with creeping flow in a short distance. This was necessary to assure uniform velocity field across the width of the device, prevent cell sedimentation, and minimize device volume for future scaling. A multi-level, orthogonal bifurcation manifold was adopted for this purpose (Figure 7).

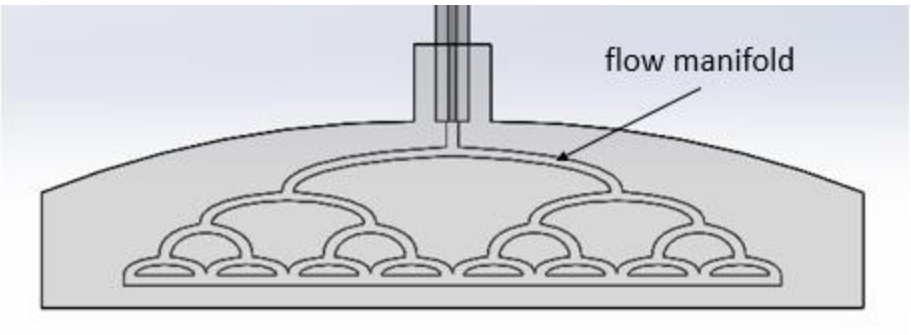

Figure 7. Orthogonal bifurcation flow manifold designed for mPharesis mesoscale device.

Design parameters included channel width, number of bifurcations, and shape of transitions and were optimized through iterative computational fluid dynamic (CFD) simulations using commercial software (Fluent, ANSYS Inc., Canonsburg, PA, USA). The inlet condition was average flow velocity of 0.3 mm s^{-1}, a pressure drop of 9.42 kPa, fluid viscosity of 4 cP at room temperature, and fluid density of 1045 kg m^{-3}. The target average flow velocity was chosen from common velocities in reported in similar continuous RBC HGMS devices[65,86–88] and was assessed in later experiments. The inlet flow rate was set as 77 µL min^{-1} from the 0.3 mm s^{-1} target average flow velocity through the 100 µm tall 43 mm wide separation area entrance. The velocity towards the flow field should be within of 5% of 0.3 mm s^{-1} and the orthogonal velocities should be within 5% of 0 mm s^{-1} across the entire flow field inlet width, with 5% chosen as an acceptable range of error.

Reynolds number (Re) was calculated using Equation 2[89]. For this device, flow is creeping and determined fully developed if the length before the separation area greater than the entrance length ($L_{entrance}$) using Equation 3 (when Re is less than 2300)[89].

$$\mathrm{Re} = \frac{D_H \rho v}{\mu} = \frac{D_H \rho Q}{\mu A} \quad [2]$$

$$L_{entrance} = \frac{0.32 {D_H}^2 \rho v}{\mu} + 1.4 D_H \quad [3]$$

D_H is the hydraulic diameter (4*area/perimeter), ρ is density, µ is dynamic viscosity, v is average flow velocity, and A is area.

3.2.3 Pilot Study for Optimal Channel Height

An initial microscopy study was performed prior to development of the mesoscale device. A drop of 0.5% Hct paramagnetic metRBCs and a single wire (SS 410 125 μm thick x 200 μm wide x 20 mm long, Kemac) were sandwiched between a glass slide and coverslip. A 12.7 mm cube neodymium N40 permanent magnet (K&J Magnetics, Pipersville, PA, USA) was placed on the coverslip just out of the inverted microscope's view (IX-70, Olympus Corporation, Tokyo, Japan) (Figure 8). The maximum distance metRBCs could be captured from the wire was approximately 50 to 70 μm, measured with a microscope reticule. However, at physiological RBC concentrations in whole blood, an H greater than 70 μm is necessary to allow for heathy RBCs to escape from the separated iRBCs and reduce cell-cell collisions from crowding. Therefore, a height constriction along the separation area in the mesoscale device was proposed.

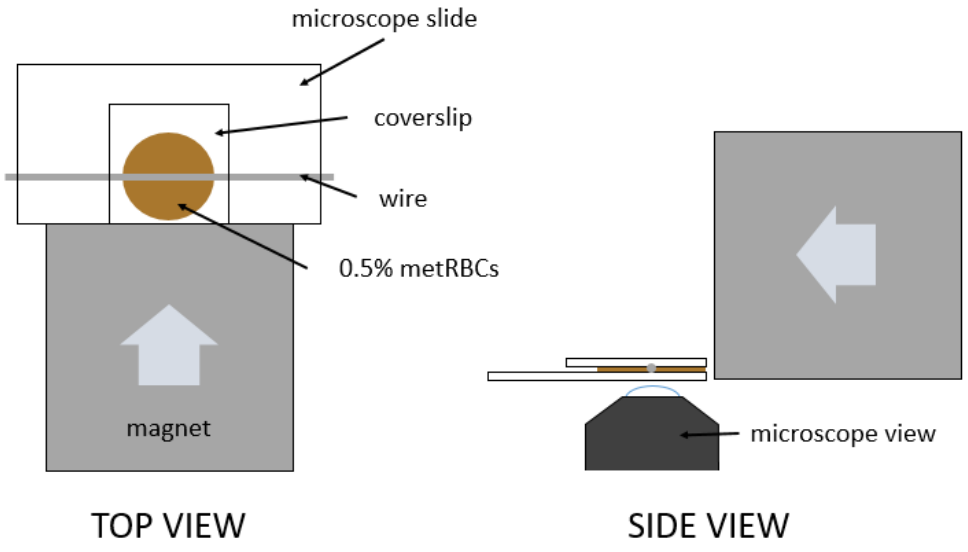

Figure 8. Setup for pilot study to determine capture distance for metRBCs.

3.2.4 CFD Simulation of RBC and iRBC Motion

Wu and Martin et al. developed a numerical method which predicts the motion of paramagnetic and non-magnetic RBCs in a HGMS flow field[90]. This section was directly taken from their publication. They investigated introducing a constriction to force all paramagnetic RBCs within the distance of greatest

magnetic force adjacent to the wire array. Their simulations compared the efficacy of various constriction geometries upon the separation efficiency of the iRBCs. Numerical simulations were performed with two computational domains, depicted in Figure 9 and Figure 10. Figure 9 depicts a three-way magnetophoretic separator in a previously reported experiment by Han et al.[86] which was used for validation of the computational model described here. For economy of computational cost, a symmetry condition was assumed, reducing the domain to half the width. Figure 10 represents the mPharesis device flow field (not drawn to scale). In both devices, blood flows within the channel along the positive x-direction. A magnetic force is generated by an external uniform magnetic field, provided by an infinitely long permanent magnet (not shown) in proximity with a single ferromagnetic wire. The solutions to the equations of motion were solved using computational fluid dynamics discrete element method (CFD-DEM). This was chosen as a reasonable alternative to mesoscale simulations, such as the Lattice Boltzmann and/or immersed boundary methods, but with more economical computational cost. The details of the constitutive models and numerical methods are provided below.

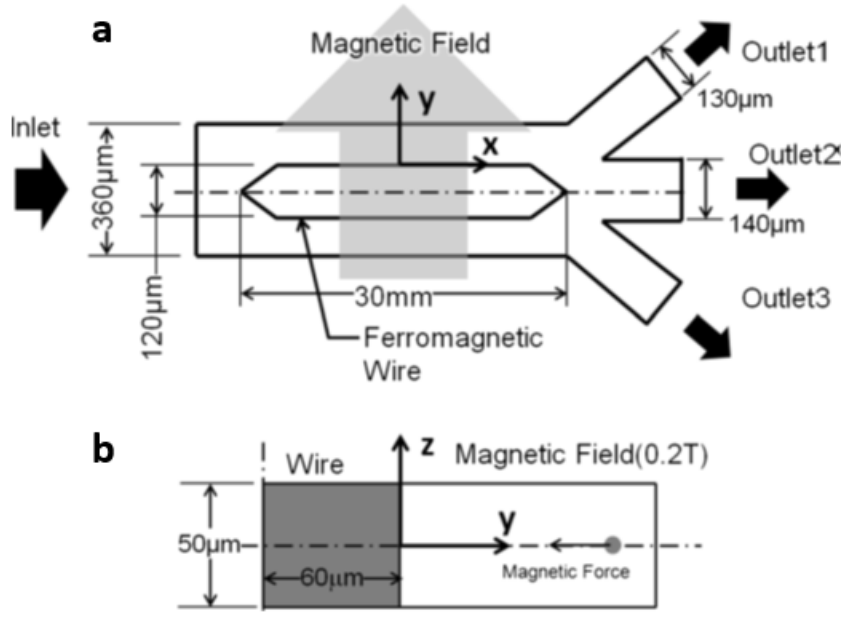

Figure 9. Schematic of the magnetophoretic separator with a rectangular ferromagnetic wire. a) Top view and b) cross-sectional view of the microchannel[86]

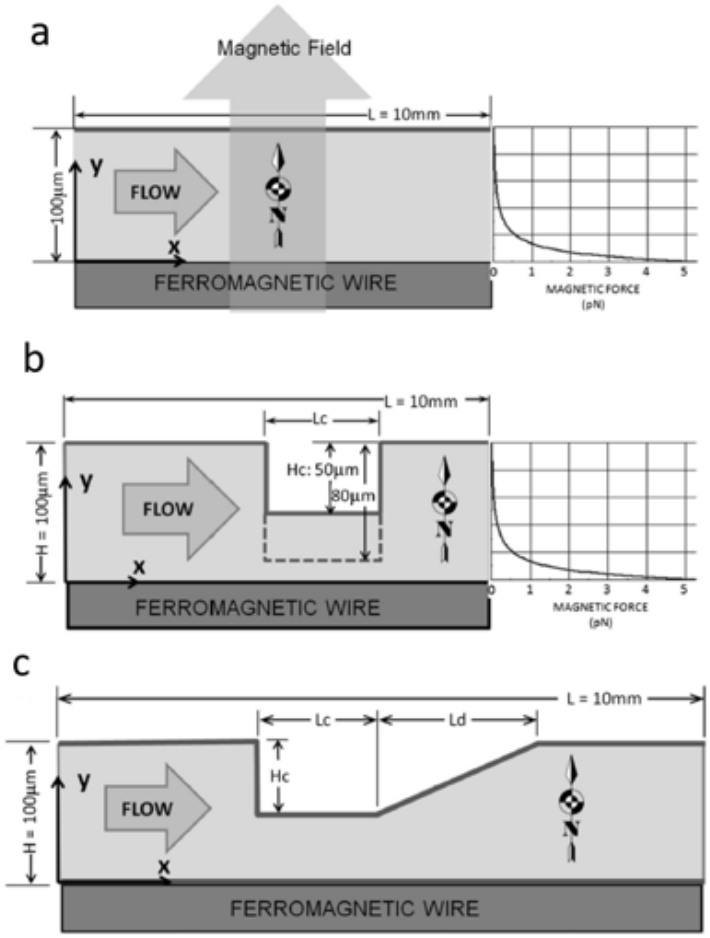

Figure 10. Wu et al.'s simulation descriptions for mPharesis (not drawn to scale) with a) no modifications, b) the addition of a constriction, and c) the addition of a constriction-diffuser[90]. All simulations were 2D.

Hc is the constriction height, L is total length of the flow field, Lc is constriction length, and Ld is the diffuser length.

3.2.4.1 CFD Simulation Governing Equations for Blood Flow

Blood was treated as a multi-component system, comprised of RBCs and plasma. White cells are considered too dilute to affect the flow system. The plasma was treated as a Newtonian fluid, obeying conservation of mass (Equation 4).

$$\frac{\partial \rho_p}{\partial t} + \mathrm{div}(\rho_p v_p) = 0 \qquad [4]$$

$\frac{\partial}{\partial t}$ is the derivative with respect to time, div is the divergence operator, $\rho_p = \varepsilon\rho_p 0$ is the density of plasma, ρ_{p0} is the density of the plasma in the reference configuration, ε is the volume fraction of plasma (1-hematocrit), and $\mathbf{v_p}$ is the velocity field. ε in turn is computed using the method introduced by Link et al.[91] The corresponding balance of linear momentum is calculated in Equation 5.

$$\rho_p \frac{D^p \mathbf{v}_p}{Dt} = \mathrm{div}(\mathbf{T}_p) + \rho_p \mathbf{b}_p + \mathbf{F}_{pr} \quad [5]$$

$\mathbf{T}_p = [-\varepsilon p + \varepsilon\lambda_p \mathrm{tr}\mathbf{D}_p]\mathbf{I} + 2\mu_p\varepsilon\mathbf{D}_p$, p is the pressure of the mixture, λ_p and μ_p are the (constant) first and second coefficients of viscosity of the pure plasma, where $\mathbf{D}_p = \frac{1}{2}\left[(\mathrm{grad}\,\mathbf{v}_p) + (\mathrm{grad}\,\mathbf{v}_p)^T\right]$. In general for any scalar β, $\frac{D^\alpha \beta}{Dt} = \frac{\partial \beta}{\partial t} + \mathbf{v}^\alpha \cdot \nabla\beta, \alpha = f, s$, and (for any vector **w**), $\frac{D^\alpha \mathbf{w}}{Dt} = \frac{\partial \mathbf{w}}{\partial t} + (\nabla \mathbf{w})\mathbf{v}^\alpha$, $\mathbf{T}_p$ represents the Cauchy stress tensors, $\mathbf{F}_{pr}$ represents the interaction forces (exchange of momentum) between the plasma and RBCs, and $\mathbf{b}_p$ refers to the body force. The balance of the angular momentum implies that, in the absence of couple stresses, the total Cauchy stress tensor is symmetric. The equation of motion of the RBC component is represented in Equation 6.

$$m_r \frac{D^2 \mathbf{x}_r}{Dt} = \mathbf{F}_{contact} + \mathbf{F}_{pr} + \mathbf{F}_{ext} \quad [6]$$

m_r is the mass of a RBCs, $\mathbf{x}_r$ is the instantial space position of RBCs, $\mathbf{F}_{contact}$ is the force of collision with other RBCs or boundaries, $\mathbf{F}_{pr}$ is the interaction force with continuous phase (plasma) and $\mathbf{F}_{ext}$ is the external force field, in this case the magnetic force. Here, $\mathbf{F}_{pr}$ includes only the drag force, and is represented by the drag model of Rusche and Issa.[92]

The soft-sphere model incorporates multiple particle-particle interactions with the trajectories determined by integrating Newton's second law. According to Cundall and Strack[93], the normal component of the contact force, $\mathbf{F}_{contact}^{m,n}$, acting on particle i by particle j (or wall) is described in Equation 7.

$$\hat{\mathbf{F}}_{contact}^{m,n} = -\hat{k}\delta\mathbf{n}^{m,n} - \hat{\eta}\mathbf{v}_r^{m,n} \quad [7]$$

where $\hat{k}$ and $\hat{\eta}$ are the normal "spring" stiffness and damping coefficient respectively, $\delta = (R_m + R_n) - |\mathbf{r}_m - \mathbf{r}_n|$ is a (fictitious) overlap between two RBCs, R is the radius of a RBC, $\mathbf{n}^{m,n} = (\mathbf{r}_m - \mathbf{r}_n)/|\mathbf{r}_m - \mathbf{r}_n|$ is the normal unit vector between two RBCs, $\mathbf{v}_r^{m,n} = (\mathbf{v}_m - \mathbf{v}_n) + (R_m\boldsymbol{\omega}_m + R_n\boldsymbol{\omega}_n) \times \mathbf{n}^{m,n}$ is the relative velocity, $\hat{\mathbf{v}}_r^{m,n} = (\mathbf{v}_r^{m,n}.\mathbf{n}^{m,n})\mathbf{n}^{m,n}$ is the normal relative velocity, and $\boldsymbol{\omega}$ is the angular velocity. The tangential component of the contact force between particles is given in Equation 8.

$$\tilde{\mathbf{F}}_{contact}^{m,n} = \begin{cases} -\tilde{k}\tilde{\delta} - \tilde{\eta}\tilde{\mathbf{v}}_r^{m,n} \text{ for } \left|\tilde{\mathbf{F}}_{contact}^{m,n}\right| \le \mu_f\left|\hat{\mathbf{F}}_{contact}^{m,n}\right| \\ -\mu_f\left|\hat{\mathbf{F}}_{contact}^{m,n}\right|\mathbf{t}^{m,n} \text{ for } \left|\tilde{\mathbf{F}}_{contact}^{m,n}\right| > \mu_f\left|\hat{\mathbf{F}}_{contact}^{m,n}\right| \end{cases} \quad [8]$$

where $\tilde{k}$, $\tilde{\eta}$, and μ_f are the tangential spring stiffness, tangential damping coefficient, and friction coefficient, respectively, $\tilde{\mathbf{v}}_r^{m,n} = \mathbf{v}_r^{m,n} - \hat{\mathbf{v}}_r^{m,n}$is the relative tangential velocity. The tangential displacement $\tilde{\delta}$ is given by Equations 9 and 10.

$$\tilde{\delta} = \begin{cases} \hat{\delta}_0\mathbf{H} + \int_{to}^{t} \tilde{\mathbf{v}}_r^{m,n}dt \text{ for } \left|\tilde{\mathbf{F}}_{contact}^{m,n}\right| \le \mu_f\left|\hat{\mathbf{F}}_{contact}^{m,n}\right| \\ -\mu_f\left|\hat{\mathbf{F}}_{contact}^{m,n}\right|\mathbf{t}^{m,n}/k_t \text{ for } \left|\tilde{\mathbf{F}}_{contact}^{m,n}\right| > \mu_f\left|\hat{\mathbf{F}}_{contact}^{m,n}\right| \end{cases} \quad [9]$$

$$\mathbf{H} = \begin{bmatrix} qh_x^2 + c & qh_xh_y - sh_z & qh_xh_z + sh_y \\ qh_xh_y + sh_z & qh_y^2 + c & qh_yh_z - sh_x \\ qh_xh_z - sh_y & qh_yh_z + sh_x & qh_z^2 + c \end{bmatrix} \quad [10]$$

$\mathbf{t}^{m,n} = \tilde{\mathbf{v}}_r^{m,n}/|\tilde{\mathbf{v}}_r^{m,n}|$ is the tangential unit vector, $\mathbf{h} = (\mathbf{n}^{m,n} \times \mathbf{n}_0^{m.n})/|\mathbf{n}^{m,n} \times \mathbf{n}_0^{m.n}|$, $c = \cos\varphi$, $s = \sin\varphi$, $q = 1 - c$, $\varphi = \arcsin|\mathbf{n}^{m,n} \times \mathbf{n}_0^{m.n}|$, $\hat{\delta}_0$ and $\mathbf{n}_0^{m.n}$are the tangential displacement and normal direction in the previous time step, respectively and μ_f is the frictional coefficient. The mechanism of the particle-wall collision is same to the particle-particle collision. The determination of the stiffness and damping coefficient can be found in Tsuji et al.[94] or Van der Hoef et al.[95]

3.2.4.2 CFD Simulation Magnetic Field Description

According to Han and Frazier[86,96], the expression for the magnetic force produced by a magnetically saturated, ferromagnetic rectangular wire placed under a uniform external magnetic field, referenced to a coordinate system centered at the origin as shown in Figure 9 is described in Equation 11.

$$\mathbf{F}_{\text{magnetic}}(z', y')$$

$$= \mu_0 M_s(\chi_{rbc} - \chi_p) V_{rbc} a^2 H_0 \frac{\left(\frac{M_s}{2H_0} a^2 + 3(a + y')^2 - z'^2\right) z'}{\left(z'^2 + (a + y')^2\right)^3} \mathbf{e}_{z'}$$

$$+ \mu_0 M_s(\chi_{rbc} - \chi_p) V_{rbc} a^2 H_0 \frac{\left(\frac{M_s}{2H_0} a^2 - 3z'^2 + (a + y')^2\right)(a + y')}{\left(z'^2 + (a + y')^2\right)^3} \mathbf{e}_{y'} \quad [11]$$

$\mathbf{e}_{z'}$ and $\mathbf{e}_{y'}$ are the unit vectors in the z' and y' directions, respectively, and $y' \geq 0$; $k = \frac{\mu_w - \mu_0}{\mu_w + \mu_0}$=1 here, μ_w and μ_0 are the magnetic permeability of the ferromagnetic wire and free space, respectively; χ_p and χ_{rbc} are the magnetic susceptibilities of the plasma and the paramagnetic RBCs; V_{rbc} is the volume of the paramagnetic RBCs; and a is the nominal radius of the wire, which for a rectangular wire is half of the wire height, 25 μm. The above governing equations were implemented in OpenFOAM (OpenCFD 2011), and solved on a PC workstation (Dell T7910). For all the cases, we have taken advantage of symmetric characteristics during the simulations. The mesh dependency studies were performed and discussed in detail in channel optimization part of the results section.

Simulations of the magnetophoretic HGMS device used by Han and Frazier were performed for four flow rates, corresponding to average velocity of 0.1, 0.2, 0.4 and 0.6 mm s^{-1}. The hematocrit was assumed to be 4%, based on the reported 1:10 dilution of bovine whole blood in saline, and assuming a nominal hematocrit of 44%[97]. Additional physical parameters are provided in Table 1.

Table 1. Physical properties and flow condition. To economize computational cost the diameter of the RBCs are specified as 8 μm.

Plasma viscosity (room temperature)	0.96 cP
Plasma density	1027 kg m^{-3}
Diameter of RBCs	8 μm
Young's modules of RBCs	26 kPa[98]
Poisson's ratio of RBCs	0.5[98]
Friction coefficient between RBCs, and between RBCs and wall	0.08[99]

The initial condition for all the simulations was a cell-free domain. A uniform inlet boundary condition was applied. All simulations were run for a duration of five times the length of the channel over mean velocity (L/v) to assure steady state conditions. To save computational cost, all simulations were performed in 2D on x-y plane at z=0, with coordinates shown in Figure 10. Accordingly, the inlet velocity boundary condition was assumed to be 1.5 times the average velocity, to correspond with the centerline velocity. The magnetic field was described by Equation 12, at z=0, corresponding to the centerline of the channel.

$$\mathbf{F}_{\text{magnetic}}(y') = \mu_0 M_s(\chi_{rbc} - \chi_p) V_{rbc} a^2 H_0 \frac{\left(\frac{M_s}{2H_0}a^2 + (a+y')^2\right)}{(a+y')^5} \mathbf{e}_{y'} \quad [12]$$

Figure 11 shows the distribution of deoxyhemoglobin RBCs passing through the separator near the outlet region. Both simulations and experiments show an obvious effect of applied magnetic force on the distribution of RBCs. Figure 12 compares the simulated versus measured percentage of RBCs exiting the central outlet (outlet2 in Figure 12) for the four velocities considered as well as the control case in which there is no magnet. There was a small systematic overestimation of RBC percentage by simulation of 0.8% to 4.7%, which was observed to be a function of flow rate.

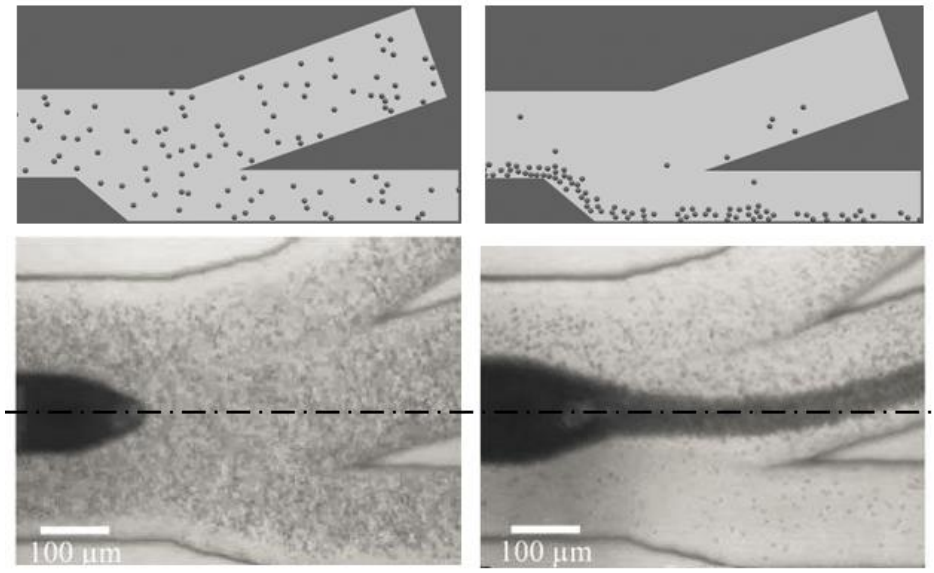

Figure 11. Comparison of simulated to experimentally observed deoxyRBCs passing through the micro-channel magnetic separator at an average flow velocity of 0.1 mm s^{-1} (a) with and (b) without applied magnetic flux (0.2 T). Experimental figures were reused with permission[86].

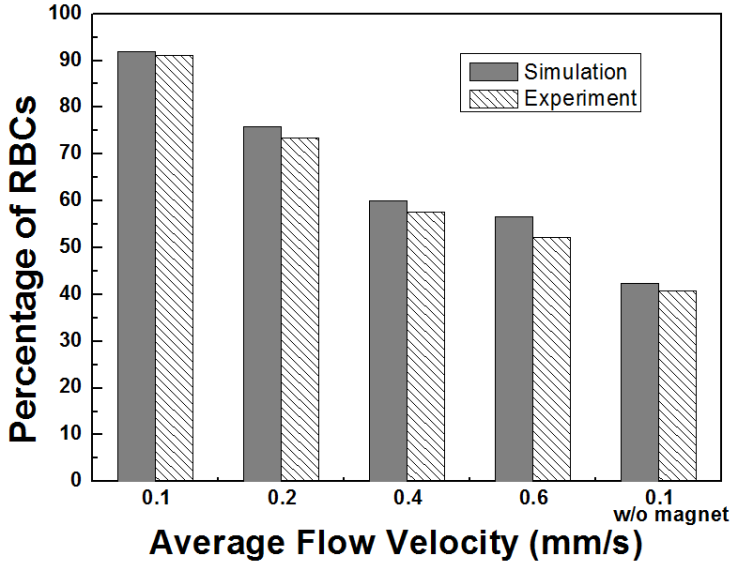

Figure 12. Comparison of simulated and experimental separation percentage of deoxyhemoglobin RBCs at outlet2 of the micro-separator for various average flow velocities[86].

3.2.5 Constriction Optimization

Based on the excellent agreement between the numerical and experimental results in the above case, the CFD-DEM model and method described in previous sections was applied to a parametric study of the mPharesis separation channel. Rheological values were applied to match clinically observed conditions, such as 40% Hct and 10% iRBCs. Also, the magnetic volumetric susceptibility difference between the

iRBCs (χ_{iRBC}=-6.2x10^{-6}) and plasma was prescribed as 1.5x10^{-6} (SI units), approximately 2.5 times less than deoxyhemoglobin RBCs ($\chi_{deoxyRBC}$=-3.8x10^{-6}) used by Han et al. All simulations were performed in 2D to economize computational costs, similar to the previous simulation. Furthermore the domain was limited to the middle region of the channel, which excluded entrance effects and the waste exit. To account for the discretization of the iRBC and RBC phases, all data shown in the following sections are averaged from 100 different time steps. Prior to simulations of the various geometries of the channels, a mesh dependency study was first performed using the 10 mm long rectangular channel (Figure 10a). It was found that meshes of 18288 and 31248 nodes both closely approximated the theoretical (Newtonian) prediction, therefore a mesh with 18288 nodes was chosen. Mesh dependency studies were confirmed for the other geometries as well.

For quantifying the separation efficiency, the iRBC density distribution across the channel was evaluated at the outlet. To accommodate the discrete size of the cells, the outlet was partitioned into 20 bins, each 5 μm in height. Two metrics were used to assess the degree of separation: iRBC capture (the relative quantity of iRBCs captured within the 20 μm bin at the outlet) and iRBC enrichment (the relative increase in concentration of iRBCs in the sub-layer compared to the bulk) described in Equations 13 and 14.

$$\text{iRBC Capture\%} = \frac{\text{iRBCs near wall}}{\text{total iRBCs}} \quad [13]$$

$$\text{iRBC enrichment} = \frac{\text{iRBCs concentration near wall}}{\text{bulk iRBCs concentration}} - 1 \quad [14]$$

3.2.6 Waste Exit Width Optimization

The width of the waste exit was any important consideration for the removal of the concentrated iRBC layer. The concentrated layer is skimmed off and is dependent on the throughput of the waste width and SR. The effect of the waste width and iRBC removal, and select the ideal width, was investigated using Wu et al.'s method from the previous section. Simulations were performed for a channel length of 10 mm, flow field height of 100 μm, and outlet width of 1 mm (Figure 13). The waste collector widths were 1, 0.4, 0.1, 0.04, and 0.01 mm. The inlet condition was an average flow velocity of 0.3 mm s^{-1} and a

pressure drop of 7.09 kPa.

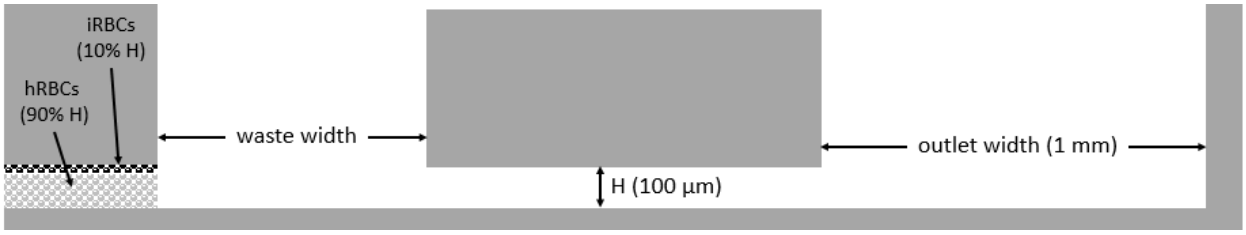

Figure 13. Simulation description for waste exit width simulations. Flow enters from the left and exits through the waste and outlet. Gray dots are healthy RBCs, black dots are iRBCs.

3.2.7 Device Fabrication Iterations

The work described in this thesis began with version 2.0 (Figure 14a). This version featured a wire array embedded in the surface of a custom machined acrylic bottom plate with inlet, waste, and outlet manifolds on a single PM. The array was heat bonded to the acrylic using an industrial cast iron heat press with 200 kPa pressure and 68 °C for 2 minutes. The top plate was attached with socket head cap screws to the bottom plate. The flow field, inlet, outlet, and waste were sealed with O-rings. The results of heat-bonding were inconsistent, so version 3.0 (Figure 14b) used double-sided pressure sensitive adhesive tape (444, 3M, St. Paul, MN, USA) to mount the wire array to the bottom plate. Version 3.0 also featured a layered laser cut acrylic bottom plate solvent bonded with dichloromethane which enabled inexpensive, rapid design changes during the prototyping process. The use of O-rings in previous versions limited the ability to precisely set the flow field height. In version 3.0, the flow field was sealed with double-sided pressure sensitive adhesive tape (444, 3M) and the height was maintained by polyethylene shim stock cut with an electronic cutting machine (Silhouette). The flow field height of assembled prototypes was estimated using Plastigauge (Plastigauge USA, Paso Robles, CA, USA) for all proceeding devices In version 3.1, the double-sided tape did not provide the target flow field height or seal well, thus was replaced with a laser cut high-purity silicone gasket (McMaster-Carr, Aurora, OH, USA) (Figure 14b).

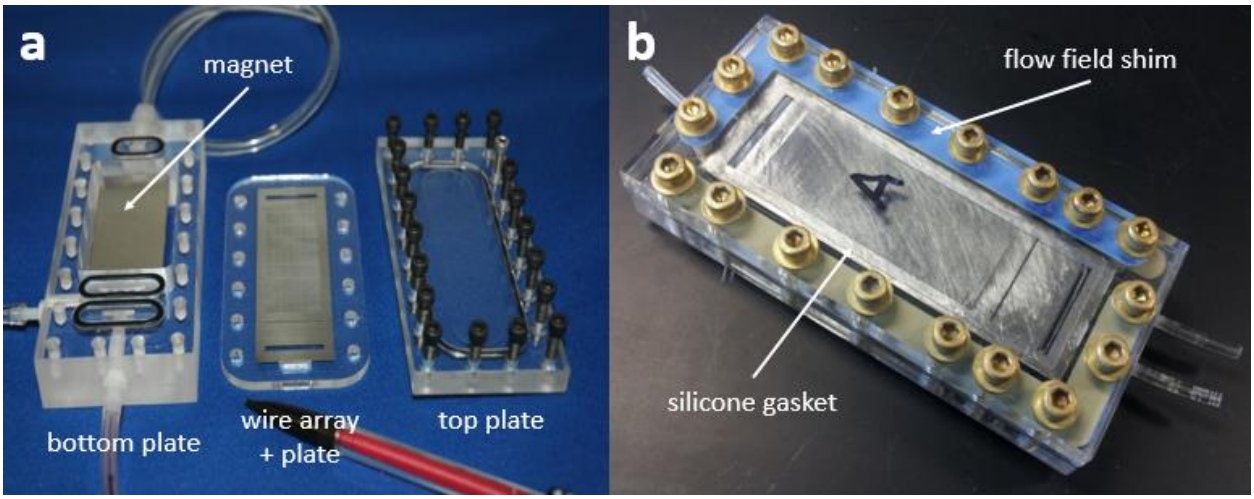

Figure 14. a) Versions 2.0 and b) 3.1 of the mesoscale mPharesis prototypes. A single PM is mounted under the wire array in version 3.1.

Version 4.0 (Figure 15) featured a larger wire array to increase throughput, designed to fit with the widest, strongest commercially available permanent magnets (discussed previously). The inlet and outlet manifolds were incorporated into the top plate to provide more room for the magnet array and remove the need to include the inlet and outlet in the photoetched wire array design. The waste exit was also removed. The wire array was separated into two pieces, the wire array and the post-waste section, to allow for the waste slit width to be modified and made thin than allowed by photoetching (1.1 times the thickness minimum, 138 μm here). The magnet array was redesigned to maximize the magnetic force across the entire flow field (discussed previously). A persisting problem for each prototype involved creating a seal: the combination of screws and an elastic gasket created a bowed flow field across the channel and made sealing the device inconsistent. This problem was solved by removing any clamping mechanisms, sealing the edges with cyanoacrylate (Loctite 430), wicked into the gap between at the wire array and top plate adjacent to the flow field shim edge, and reinforced with thin solvent-bonded acrylic pieces.

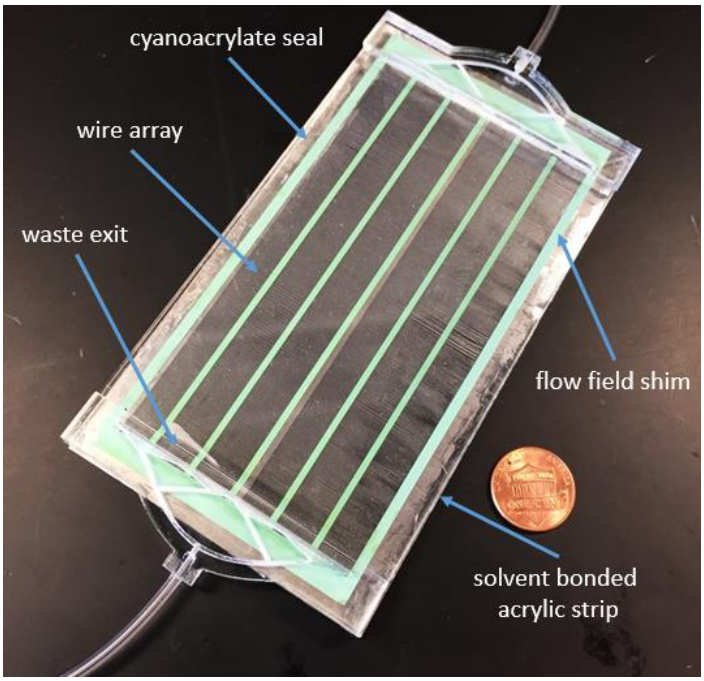

Figure 15. Version 4.0 of the mesoscale mPharesis prototype. The magnet array is not shown here.

Initial experiments with the version 4.0 mesoscale prototype revealed a problem of metRBCs collecting in the crevices between ferromagnetic wires that then became nearly impossible to flush. Multiple thin coatings were tried to prevent the metRBCs from sticking to the wire surface, such as a zwitterionic silanated phosphorylcholine (used for blood-contacting devices)[100], nano-plated gold and titanium applied via electron beam physical vapor deposition (6J and 8L Perkin Elmer Sputtering Systems, Allwin21 Corp., Morgan Hill, CA, USA), Teflon® spray (DuPont, Wilmington, DE, USA), and skived PTFE sheeting (12.7 μm thick, DeWal Industries, Narragansett, RI, USA). The gold, titanium, and zwitterionic coatings showed no improvement in reducing metRBC adhesion. The spray Teflon was easily washed away. The skived PTFE sheeting was difficult to adhere to the grid surface and formed large interstitial air bubbles. This problem was solved in version 5.0.

3.2.8 v5.0 Device Fabrication

The most recent prototype of this device (version 5.0, Figure 16) consists of five parts: a top plate with inlet flow manifold and outlet collector, a flow path shim, a constriction, a photoetched stainless steel ferromagnetic wire array mounted to a bottom plate with waste manifold and an external neodymium

permanent magnet array. The flow channel with wire array is disposable while the permanent magnet can be reused.

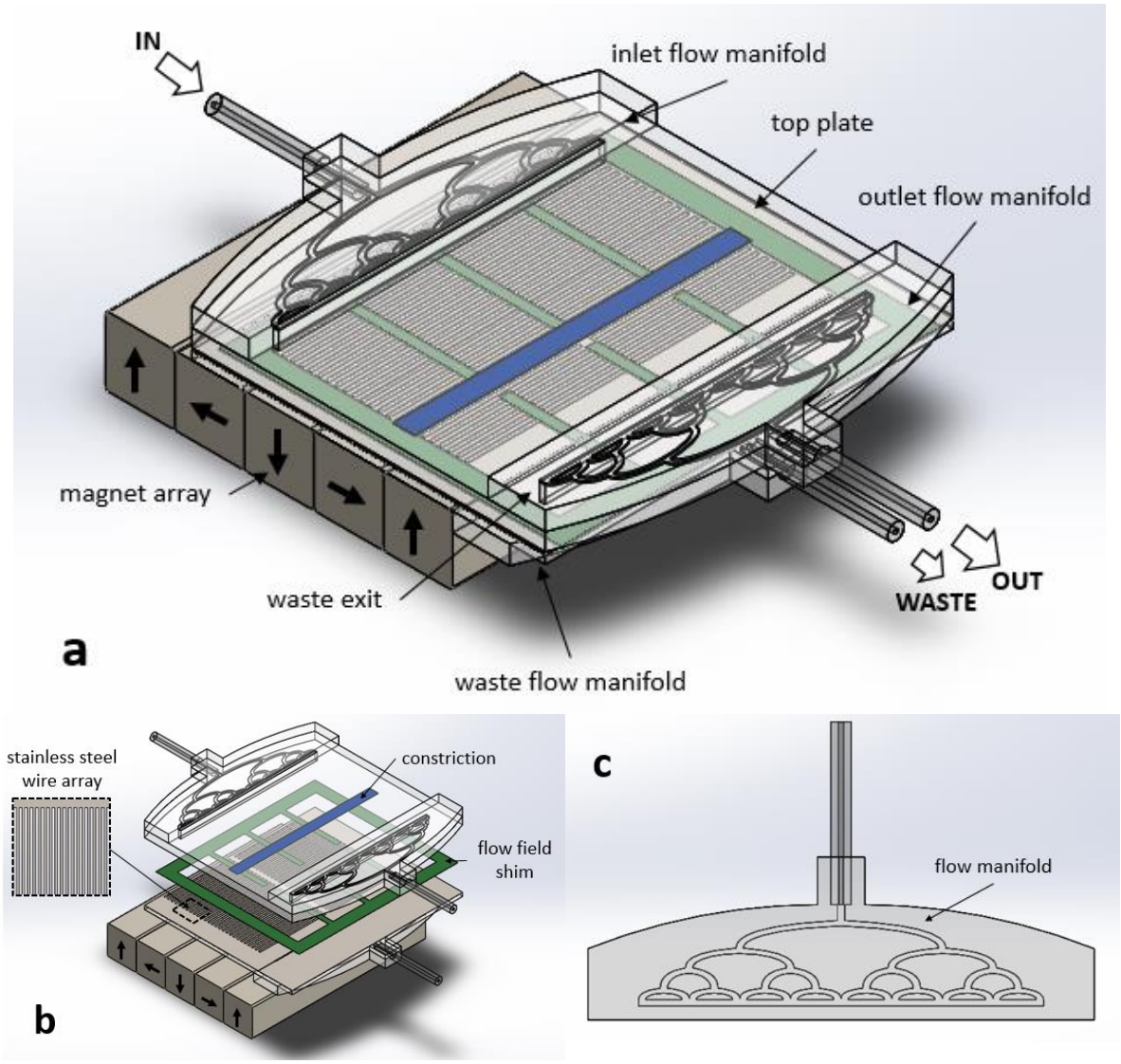

Figure 16. a) Schematic of proposed mPharesis lab-scale device and b) exploded view c) close-up of the flow manifold.

The combination of the ferromagnetic wire array, arranged perpendicular to the direction of flow, and strong permanent magnets creates a HGMS force applied orthogonal to the blood flow direction. As blood flows through the device, the paramagnetic cells are continuously deflected towards the wire array attached to the bottom plate and then removed by the thin waste exit. The remaining filtered blood exits through the outlet.

The device was primarily comprised of cast acrylic layers (McMaster-Carr, Aurora, OH, USA) laser cut (Epilog Laser, Golden, CO, USA) and solvent bonded together with dichloromethane. The flow manifold flow paths were laser engraved into 3 mm thick cast acrylic pieces. The wire array was photo-etched from 125 µm thick SS410 stainless steel (Kemac Technology Inc., Azusa, CA, USA). The photoetched wire array was attached to the 1.5 mm thick mount plate with 3M 444 double-sided pressure sensitive adhesive tape. The target 40 µm waste exit width was created using metal shims during the array attachment. The wire array crevices were filled with adhesive (Loctite 290 Threadlocker and 7469 Primer, Henkel Corporation, Weirton, WV, USA). A thin 13 µm thick polytetrafluoroethylene (PTFE) sheet was smoothed over the surface to remove excess adhesive and bubbles before curing overnight. The cured array was carefully planed flat with a chisel knife blade to remove excessive adhesive.

A flow gasket was made from 100 µm thick polyethylene shim stock cut with a CNC cutting machine (Cameo, Silhouette America, Lehi, Utah, USA). Three evenly-spaced 2 mm wide strips were incorporated into the shim to help maintain flow field height in the slight vacuum created from pulling fluid through the device. The assembly was aligned and the device edges were sealed with cyanoacrylate adhesive (Loctite 430, Henkel Corporation, Weirton, WV, USA) and reinforced with overlapping 0.8 mm thick acrylic strips. The constriction-diffuser step was made using a precision ground drawdown bar (Dura-Metal Products Corp., Irwin, PA, USA) made from high density zirconia ceramic with the step's profile cut radially into the shaft. Fast drying nail polish was chosen as the constriction material for its useful viscosity, work handling time, and durability. The polish was applied to the top plate piece and spread with the drawdown bar to produce the constriction (see Figure 17). A 2 mm margin at the plate's edge was removed to accommodate the flow field shim. Figure 17 shows the final device.

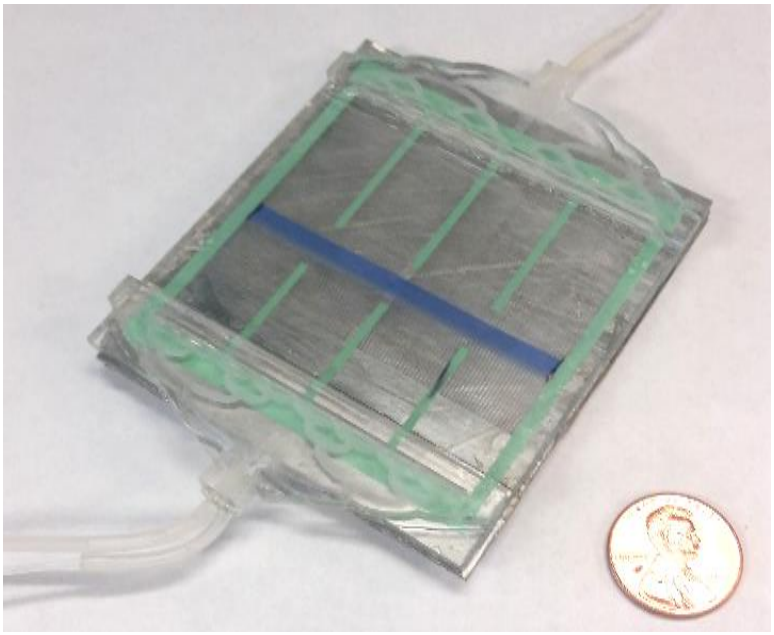

Figure 17. Assembled mPharesis device. The flow field shim is green and constriction-diffuser step is blue.

A quality control step was performed to ensure the planed surface was free of micron-sized irregularities which can cause remixing. A Surftest SJ-210- Series 178-Portable Surface Roughness Tester (Mitutoyo America Corporation, Aurora, IL, USA) was implemented. The Surftest has a 2 µm wide stylus head, 360 µm roughness range, and 0.02 µm resolution at two readings per µm. Nine randomly spaced lines were tested, each transverse to the wire array and 2.7 mm long. Measurements of roughness by profilometry verified that the surface finish variation was within 2.37±0.770 µm with an overall maximum of 10.2 µm.

3.2.9 Shear Stress Calculation

Physical forces in blood contacting devices, such as large shear stresses, are strongly believed to lead to hemolysis (i.e. the fragmentation of red blood cells). In vitro, hemolysis has been reported to occur above shear stresses of 150 Pa[84]. Shear stress (τ) for Newtonian Stokes flow (i.e. RBC-saline suspension, creeping flow) in the mesoscale mPharesis device was calculated with Equation 15.

$$\tau = \frac{\mu v}{D_H} \qquad [15]$$

Figure 18 shows the flow field through the mesoscale device, without inlet and outlet tubing, with numbered segments. Shear stress was calculated for each segment at the maximum experimental flow rate.

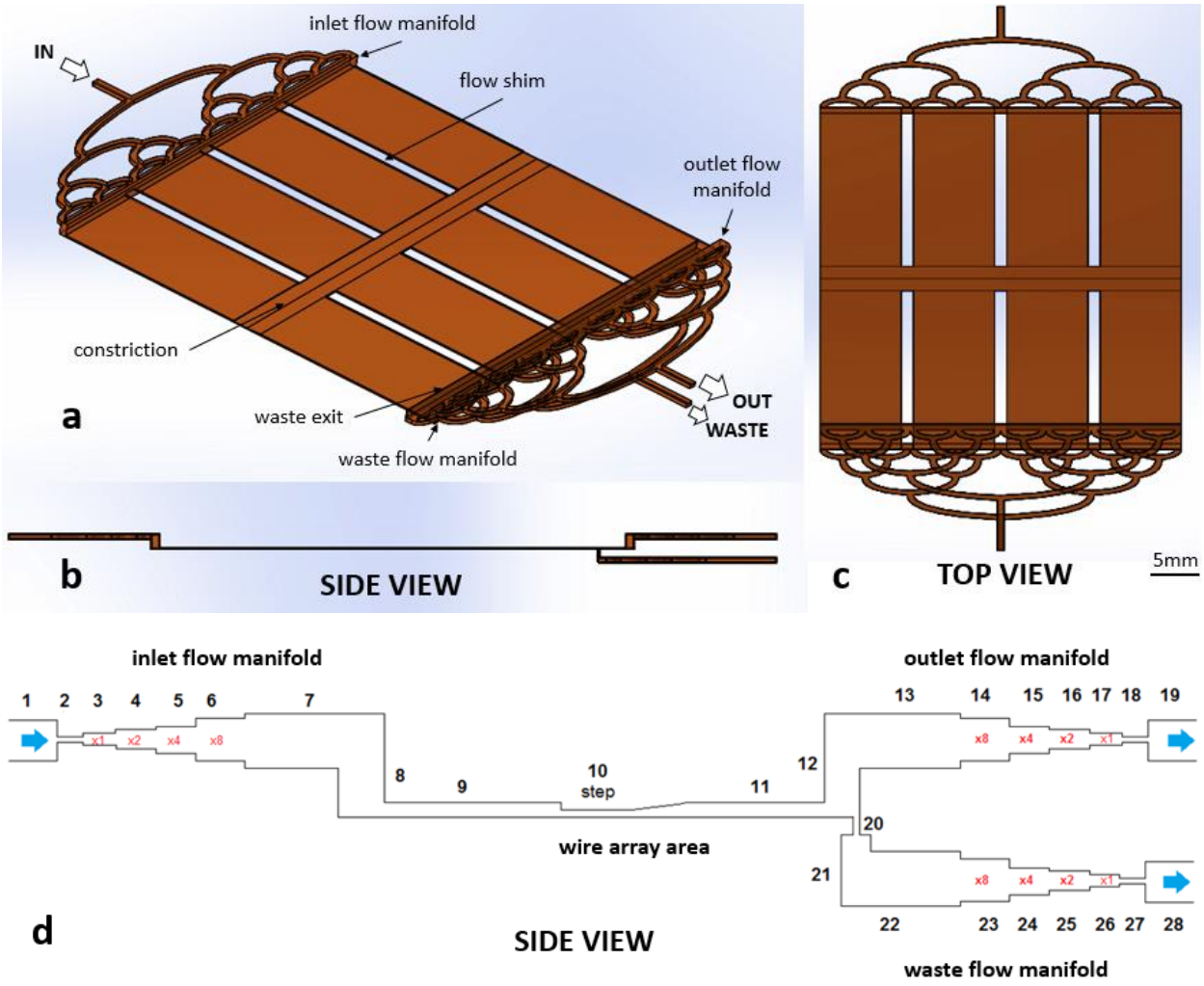

Figure 18. Flow field for v5.0 mesoscale mPharesis device in a) isometric, b), side, and c) top views (does not include tubing connecting to inlet, waste, or outlet. d) Numbered diagram of mesoscale flow path with numbered segments (not to scale).

3.2.10 metRBC Preparation

Although the asexual stage of iRBCs is noninfectious, the iRBC cultures have a small chance of containing infectious sexual stage *P. falciparum* parasites. Also, physiological iRBC cultures are very difficult to maintain and require special Biosafety Lab (BSL-2) certifications. Methemoglobin-containing RBCs (metRBCs), which occur naturally in humans in very low amounts, also feature a high spin ferric iron and can be made in-lab using a sodium nitrite oxidation. MetRBCs remain stable when stored

properly[74]. MetRBCs and iRBCs also have similar cell wall rigidity and approximate magnetic susceptibility, though the susceptibility of iRBCs steadily increases from near-zero as the parasite grows[101]. Deoxygenated RBCs (deoxyRBC) are similarly paramagnetic with a high spin ferrous form, though they quickly lose that property in the presence of oxygen, and can be made benchtop via sodium dithionite, sodium hydrosulfite, or nitrogen gas to reduce iron atom content[86,88,102]. Oxygenated RBCs are slightly diamagnetic and can be repelled by a magnetic field. Late-stage iRBCs, metRBCs, deoxyRBC, and oxyRBCs have magnetic volumetric susceptibilities of 1.89×10^{-6}, 0.28×10^{-6}, 0.265×10^{-6}, and -0.0147×10^{-6} respectively (SI units, $\Delta\chi$ volumetric compared to water)[74,101] with a negative value indicating repulsion to a magnetic field. MetRBCs, thus, can be used as a paramagnetic analog as they have a similar magnetic susceptibility as early-stage iRBCs.

MetRBCs were prepared using fresh whole blood from an adult donor obtained via venipuncture with a protocol approved by the Institutional Review Board (IRB) for use of human subjects in research. The RBCs were washed three times in Phosphate-Buffered Saline (PBS) (P4417, Sigma-Aldrich Corp., St. Louis, MO). The buffy coat and plasma were removed, then the RBCs were re-suspended in PBS to 50% hematocrit (Hct) with 1% v/v of Gentamycin (Gentamax 100). Solid $NaNO_2$ (0.069g per 1mL of RBC suspension) (237213 Sigma-Aldrich) and 1X PBS (10 mL per 1 mL of RBC suspension) were vortexed together then added to the RBC suspension. The mixture was incubated in a closed, rocked container at room temperature for 90 minutes, and then washed three times. RBCs used in Specific Aim 3 were further rigidified separately in a 48 °C water bath for one hour. All RBCs were stored at 4°C. The concentration of converted metRBCs was verified using a hemoximeter (OSM-3, Radiometer, Brønshøj, Denmark) to measure %metHb, $\%HbO_2$, and %RHb (accurate to within approximately ±0.1 g/dL or about ±0.3% Hct). RHb is reduced hemoglobin. The rigidity of the metRBCs (heat treated and un-heated) and healthy RBCs (hRBC) were compared qualitatively by deforming the cell membrane at shear rates of 0, 33.3, 133.3, and 266.7 s^{-1} via an Optical Shearing System (CSS450, LinkamScientific Instruments Ltd, UK) at 6% Hct in 5.6% Polyvinylpyrrolidone (PVP).

3.2.11 Experimental Setup

The full experimental setup for verification of the mPharesis mesoscale device is shown in Figure 19. The device and magnet array was mounted to a scissor jack with a laboratory rocker which actively mixed the inlet syringe containing a 6 mm stainless steel BB throughout the experiments. The outlet and waste flows were pulled through the device and controlled by a syringe pump (Pump 33, Harvard Apparatus, Holliston, Massachusetts, USA).

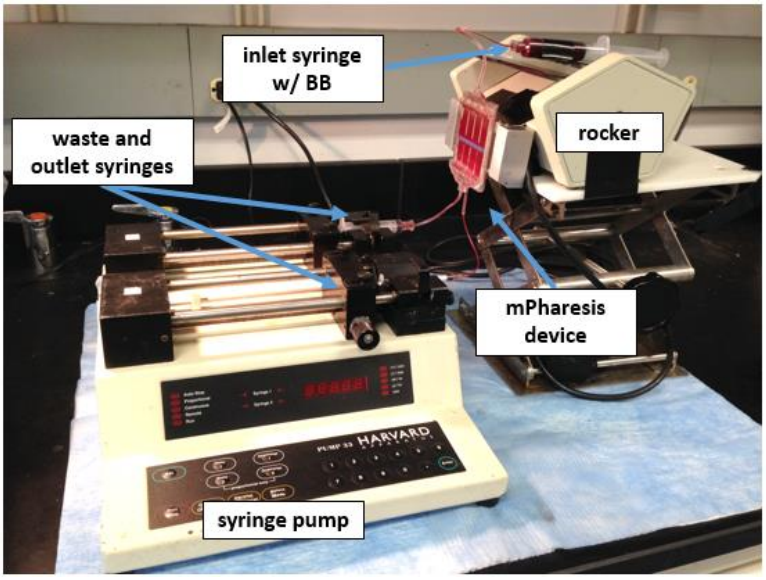

Figure 19. Experimental setup for an mPharesis device verification experiments.

The inlet syringe contained a mixture of metRBCs and hRBCs with a target inlet Hct of 30% and metRBC percent of 20%. This mixture was chosen for these studies to mimic average clinical parameters reported for an anemic patient with severe hyperparasitemia[21,52,55,103–107]. The relatively high inlet parasitemia, compared to World Health Organization's 5% lower limit for definition of hyperparasitemia, also reduces the contribution of error in measured hemoximeter values[52]. Table 2 lists the experimental parameters flow rate (Q) and SR implemented. Repeated experiments were performed for the condition which produced the best results (described in the next section). To minimize experimental error, the waste and outlet flow manifold dead volumes were drained and discarded before proceeding.

Table 2. Experimental parameters for mesoscale device verification

Condition	n	Q (μL min^{-1})	SR
1	3	77	5%
2	21		10%
3	3		20%
4	3	39	10%
5	3	154	
6	3	231	
7	3	308	
8	3	385	

The initial inlet, final inlet, waste and outlet were sampled and processed by a hemoximeter to measure hematocrit, %HbO_2, %metHb, and %RHb. Samples were randomly checked for hemolysis by visually qualifying plasma-free hemoglobin in the supernatant in a 9 μL capillary tube after centrifugation for 3 minutes at 14,000 g (Model C-MH30, UNICO, Dayton, NJ, USA). At the end of an experiment set, the device was flushed with 30 mL each of 1X PBS, 10% Tergazyme, 10% Simple Green, and distilled water in sequence. it was then dried with house air and stored at 4 °C for later use.

3.2.12 v5.0 Device Performance Metrics

Two metrics were defined to evaluate the performance of the device: conservation of mass through the device, the reduction of metRBCs returned to the patient, metRBC removal efficiency (Equation 16, $\eta_{removal}$) and hRBC rescue efficiency (Equation 17, η_{rescue}), the percentage of healthy RBCs recovered in the outlet. Standard deviation for multiple measurements of one sample (SD) was calculated with Equation 18. The propagation of error for averaged measurements from different experiments for the same test condition (pooled variance, SD,total) was calculated with Equation 19.

$$\eta_{removal} = 1 - \frac{Q_{in}*[metRBC]_{in} - Q_{out}*[metRBC]_{out}}{Q_{in}*[metRBC]_{in}} = \left(1 - \frac{(1-SR)*\%metHb_{out}*Hct_{out}}{\%metHb_{in}*Hct_{in}}\right) * 100\% \quad [16]$$

$$\eta_{rescue} = \frac{Q_{in}*[hRBC]_{in} - Q_{out}*[hRBC]_{out}}{Q_{in}*[hRBC]_{in}} = \frac{(1-SR)*\%HbO_{2,out}*Hct_{out}}{\%HbO_{2,in}*Hct_{in}} * 100\%$$

[17]

$$SD_i = \sqrt{\frac{1}{n-1}\sum_{i=1}^{n}(m_i - \bar{m}_i)^2} \quad [18]$$

$$SD, total = \sqrt{\frac{1}{N}\sum_{j=1}^{N} SD_j^{\,2}} \quad [19]$$

[metRBC] and [hRBC] are metRBC and hRBC concentration, respectively. n is the number of measurements of one sample (always three), i and j are the indices of summation, m is the indexed measurement (e.g. Hct, $\%HbO_2$, or %metHb), $\bar{m}$ is the mean of multiple measurements of one sample, and N is the number of measurements from different experiments for the same test condition.

3.3 Results and Discussion

3.3.1 Magnetic Force Description Results

Error! Reference source not found.

Table **3** lists the average magnetic force within the flow field domain for each wire and magnet array combination. The goal was to produce a large magnetic force homogenously across the entire array. The single magnet showed large forces only at the corners while the multi-magnet arrays showed spikes at every interface where flux was most concentrated. The Hallbach arrangement shows a more homogenous averaged force across the array face and a larger magnitude overall. The three 50.8 mm x 25.4 mm alternating array plus the two arrangements of the five 12.7 mm magnets and nine 6.3 mm magnets had comparable peak magnitudes. However, the five 12.7 mm magnet Hallbach arrangement was chosen for its greatest average magnetic force across the array. **Error! Reference source not found.**Figure 20 shows the magnetic force plots for the five magnet Hallbach arrangement (FEMM simulation results and

magnetic force plots for all six arrays are shown in Appendix A). The five-magnet Hallbach array was found to produce greatest average magnetic gradient of 0.33×10^{-2} T μm^{-1} with a local maximum of 5.7×10^{-2} T μm^{-1}. For comparison, previously reported experiments using a single magnet were able to concentrate metRBCs or late-stage iRBCs employing a magnetic gradient of the order 1×10^{-6} to 6×10^{-6} T μm^{-1} [4,14], a factor of over thousand less.

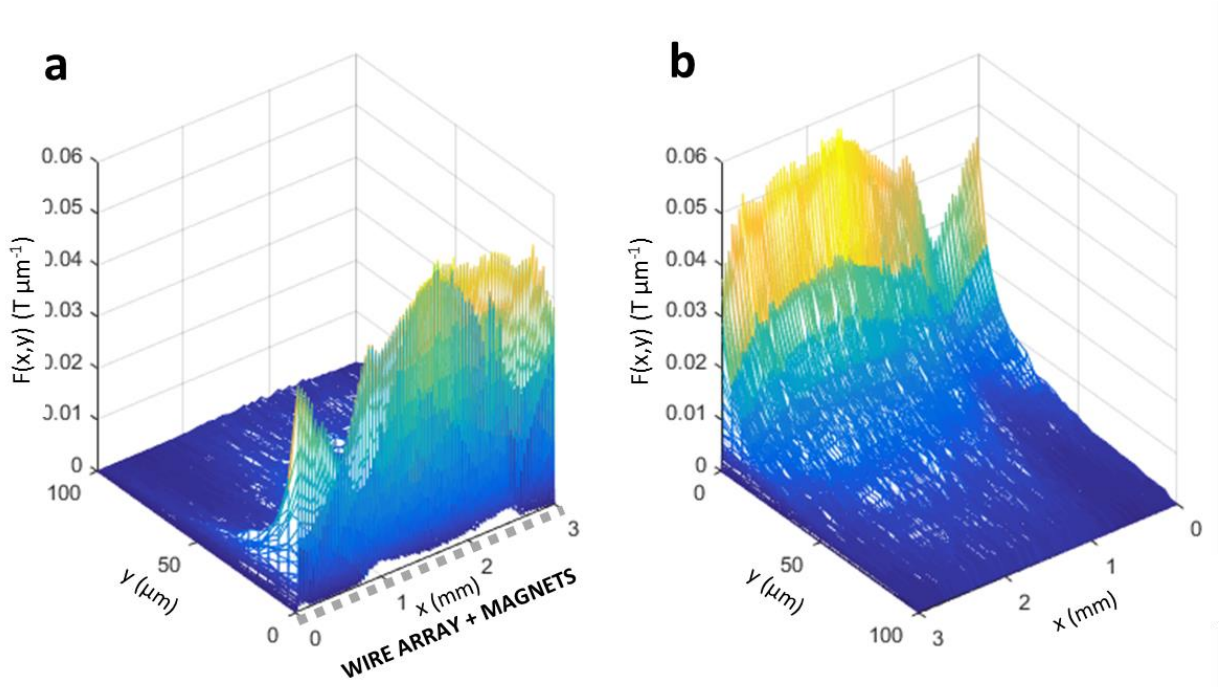

Figure 20. The magnetic force (|grad(B)|) plotted across the flow field domain (**Error! Reference source not found.**) for the ive Hallbach magnet arrangement and wire array combination a) viewed at x=y=0 and b) x=100 μm y=3 mm.

Table 3. Average magnetic force across mPharesis wire array 1.5 mm away from six magnet array configurations.

Magnet array configuration	Average magnetic force in x-direction (10^{-2} T μm^{-1})
one 76.2 mm x 12.7 mm	0.63
three 25.4 mm x 12.7 mm	2.6
five alternating 12.7 mm x 12.7 mm	2.9
five Hallbach 12.7 mm x 12.7 mm	3.3
nine alternating 6.3 mm x 6.3 mm	2.2
nine Hallbach 6.3 mm x 6.3 mm	3.2

Five long 76.2 mm x 12.7 mm x 12.7 mm magnets in a "washboard" arrangement were implemented. These long magnets were more than 27% wider than the flow field width to minimize edge effects. Long

magnets were used rather than a checkerboard pattern of magnet cubes. The reasoning is illustrated in Figure 21. A checkboard pattern inhibits the implementation of Hallbach arrays across the entire magnetic surface as adjacent magnetic poles cannot readily be placed in parallel, only orthogonal or anti-parallel. An inversed (i.e. upside down indicated in red in Figure 21) Hallbach array is weaker than a standard alternating array because the flux is concentrated on the opposite face. Also, magnetic force produced by magnetic flux concentrated along the length of a wire is much weaker than across the wire transversely (shown in Figure 21). Thus, it was best to use a washboard magnet array design that limited flux in the direction along the length of the wires.

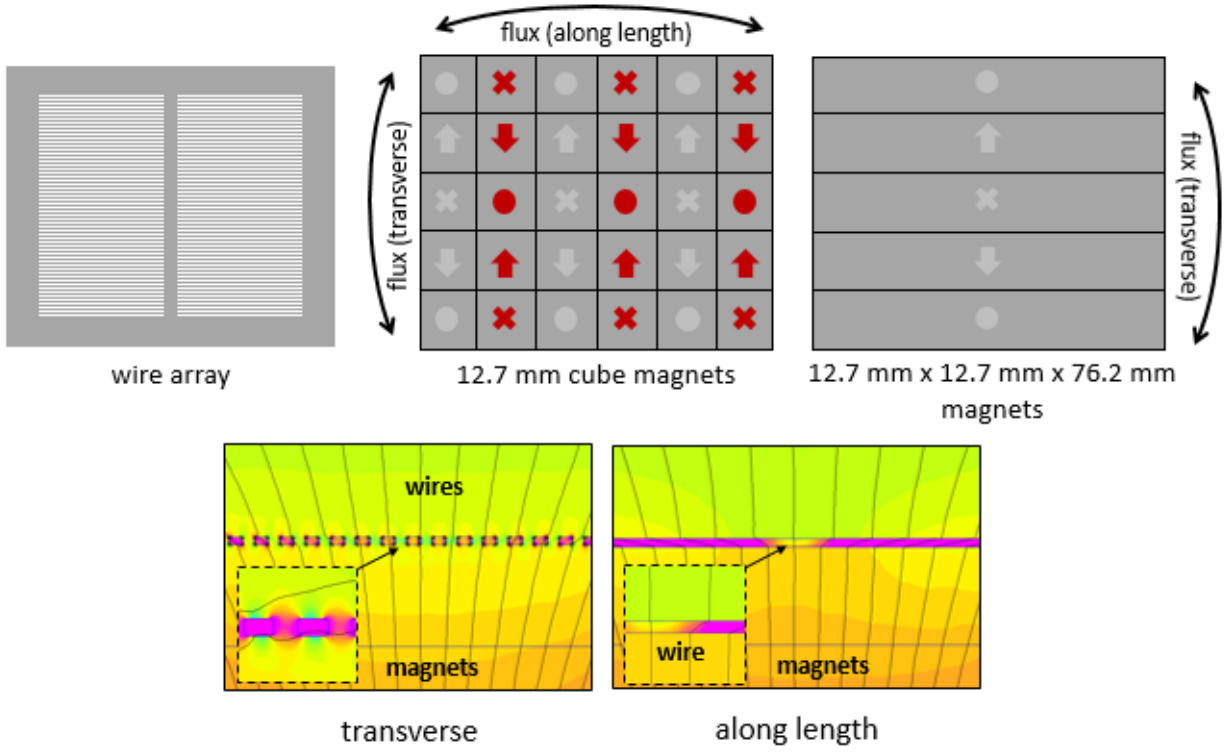

Figure 21. Illustration of the principal difference in magnetic force design for a checkboard and washboard magnet pattern. Gray arrows, circles, and x's represent a standard Hallbach array, red shapes represent an anti-parallel (inverse) Hallbach array. FEMM plots, flux density ranges from 0 to 0.76 Tesla (blue to pink)

While it is imperative that the flow field be directly adjacent to the secondary element where the force is strongest, simulations proved the distance between the primary permanent magnet and secondary element is less sensitive. The difference in resultant magnetic force produced when the wire array was mounted to

a 0.5 mm versus 1.5 mm thick piece of acrylic was not substantial. Thus, the 1.5 mm piece of acrylic was chosen because it was easier to assemble and prevent warping of the wire array during cleaning.

3.3.2 Inlet Manifold Design Optimization Results

The challenge of creating a homogeneous, laminar flow field with a large height to width ratio (360:1) was solved while limiting dead volume and enabling a quick benchtop fabrication protocol with off-the-shelf materials. The flow was calculated to be fully developed before the separation area ($L_{entrance}$=0.2 mm for v=0.3 mm s^{-1}). Figure 22 shows the velocity streamline color plot and plots for the custom designed flow manifold created with ANSYS. Figure 22c shows a uniform streamline distribution through the outlet area with an average flow velocity of 0.31±0.045 mm s^{-1} in the exiting z-direction. The calculated velocities in the orthogonal directions x and y were 0.00±0.0090 and 0.0078±0.00075 mm s^{-1}, respectively, each deemed within an acceptable range of error.

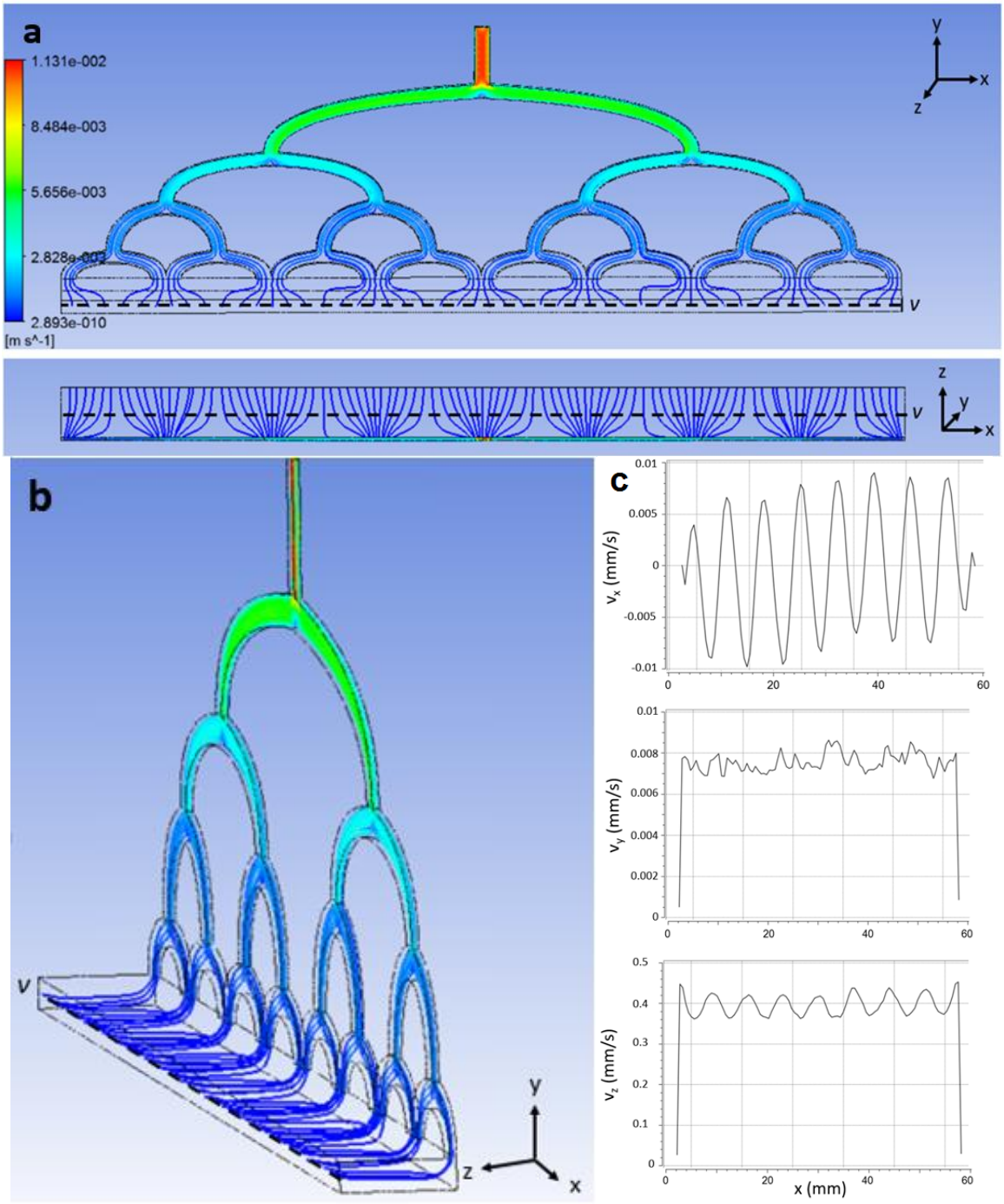

Figure 22. a) Streamlines within inlet manifold (front and bottom view). b) Isometric view. c) 2D velocity plots in the x, y, and z-directions along the dotted line indicated in a and b.

3.3.3 Constriction Optimization Results

3.3.3.1 Effect of Constriction Height H_c (L_c=2 mm)

The iRBC distributions are provided in Table 4 for rectangular constrictions of 50% and 80%, 2 mm in length, and are compared with the baseline (no constriction). Figure 23 shows the percentage of the iRBCs in the near-wall bin. A value of 20% would imply no stratification of iRBCs, and 100% would correspond to complete stratification. The above index ranges from 0% for no stratification to a maximum of 400% if all cells are stratified to the sub-layer (i.e. iRBC concentration from 4% to 16%).

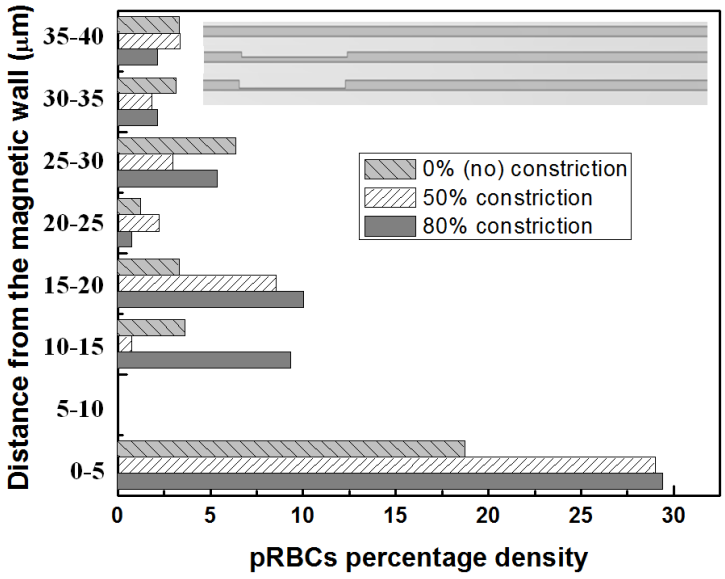

Figure 23. Percentage density distribution at the outlet along the y direction, effect of H_c (Wu et al.[90]).

Table 4. Effect of constriction height on iRBCs separation rate.

Constriction (H_c)	iRBC Capture	iRBC Enrichment	ΔP (Pa)
No constriction	26%	28%	17
50% (50 μm)	38%	92%	41
80% (80 μm)	49%	139%	442

As contrasted to the channel without constriction, which provided very limited enrichment (28%) the channels with constrictions were markedly more efficient (91.5% and 139% for the 50 μm and 20 μm constriction respectively.)

3.3.3.2 Effect of Constriction Length L_c (H_c=80%)

To evaluate the relative benefit of lengthening the constriction L_c, six different lengths were evaluated (0.2, 0.5, 1.0, 2.0, 4.0 and 8.0 mm) each with a height of 20 μm. These results are provided in Table 5 and Figure 24. It can be seen that there is a slight improvement with length from 0.2 mm up to 4 mm, beyond which further extension to 8 mm yields diminishing returns.

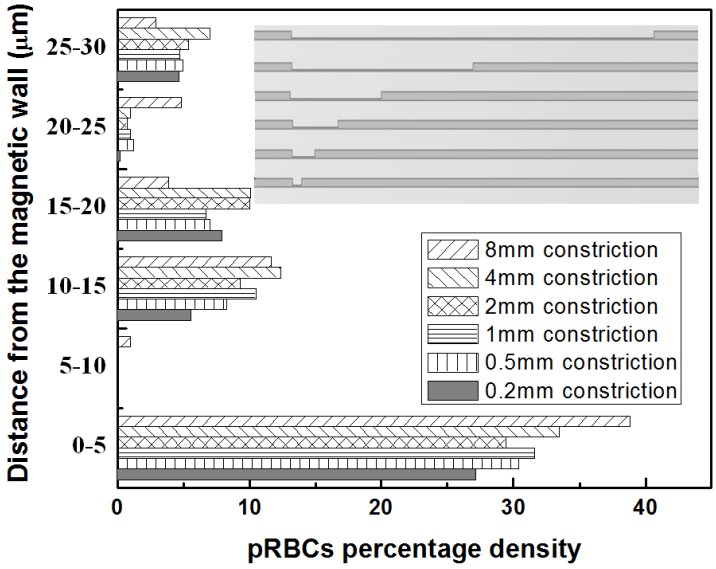

Figure 24. Percentage density distribution at the outlet along the y direction, effect of L_c (Wu and Martin et al.[90]).

Table 5. Effect of constriction length on iRBCs separation rate (H_c=80 μm).

Length of the constriction (L_c)	iRBC Capture	iRBC Enrichment	ΔP (Pa)
8 mm	55%	177%	1727
4 mm	56%	180%	872
2 mm	49%	139%	442
1 mm	49%	144%	235
0.5 mm	46%	128%	128
0.2 mm	41%	103%	64

3.3.3.3 Effect of the Diffuser after the Constriction L_d (L_c=2 mm, H_c=80%)

Following the constriction, RBCs should gradually separate from the wall, leaving the iRBCs trapped in the magnetic boundary layer. However a sudden expansion was observed to cause a flow disturbance that draws iRBCs away from the wall (Figure 25a). Therefore a tapered diffuser was introduced for the case of 80 μm tall and 2 mm long constriction (Figure 25b). The corresponding concentration profiles at the exit

of the channel are provided in Table 6 and Figure 26 which reveals a dramatic improvement (from 139% to 261%) by introducing a diffuser of just 1 mm. The incremental improvement by extending the diffuser to 2 mm was negligible.

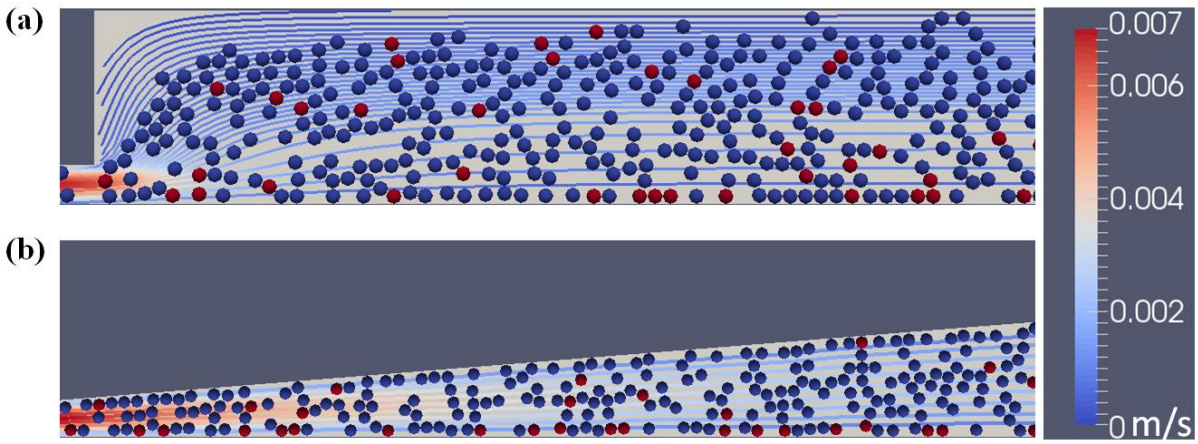

Figure 25. Snapshot of RBCs distribution in the channel region near the outlet of the constriction. Healthy RBCs are blue and iRBCs are red. (a) Channel with H_c=80 μm, L_c=2 mm constriction and no diffuser; (b) Channel with H_c=80 μm, L_c=2 mm constriction and L_d=1 mm diffuser (Wu et al.[90]).

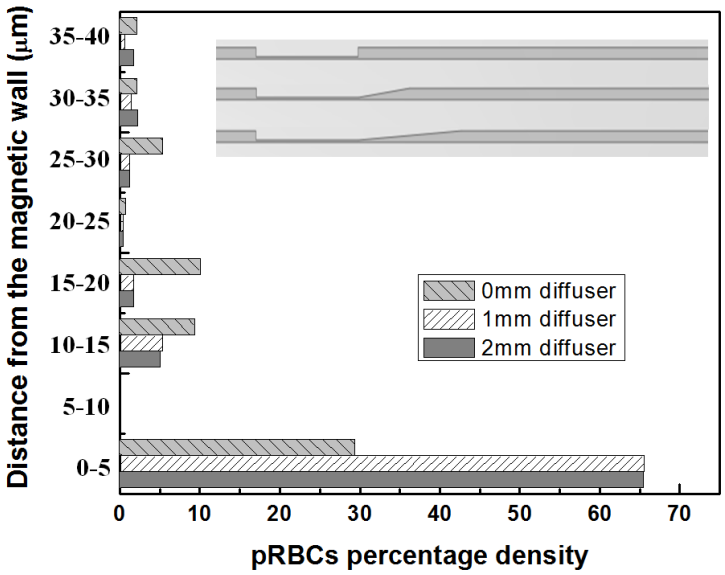

Figure 26. Percentage density distribution at the outlet along the y direction, effect of L_d (Wu et al.[90]).

Table 6. Effect of diffuser length on iRBCs separation rate (H_c=80 μm)

Length of the diffuser (L_d)	iRBC Capture	iRBC Enrichment	ΔP (Pa)
None (sudden expansion)	49%	139%	441.94
1 mm	73%	263%	468.20
2 mm	72%	261%	495.91

For a flow field with nominal height of 100 μm, the addition of a 50 μm constriction improved iRBC separation by 80%, 26% to 49%, compared to one without. The addition of a diffuser immediately after the constriction prevented large pressure-gradients post-constriction, which cause re-mixing, further improving separation to 72%. Figure 10 shows Wu et al.'s simulations as three diagrams. Wu et al. reported the optimal step shape found was a 2 mm long 50 μm constriction followed by a 2 mm long diffuser (α=1.43°). For an average flow velocity of 0.3 mm s^{-1} in the wire array flow field, Re was calculated as $3.9x10^{-3}$ and $L_{entrance}$ was calculated as less than 0.2 mm. The constriction was placed approximately 18 mm from the inlet and outlet manifolds for ease of handling and fabrication as well as ensuring the flow was fully developed in case calculations were underestimated.

3.3.4 Waste Exit Width Optimization Results

The simulation results of the parametric study of waste exit widths are presented in Figure 27. The 1, 0.4, and 0.1 mm wide waste widths failed due to recirculation from the waste region causing iRBCs from the waste region to enter the outlet exit. The recirculation was due to the outlet generating a higher pressure drop than the waste (H=0.1 mm before the outlet). This was most pronounced for the widest 1 mm width and least for the 0.1 mm width. The 0.04 and 0.01 mm wide waste exit widths did not show recirculation issues. The thinnest 0.01 mm waste exit did not have sufficient throughput to skim off the entire paramagnetic RBC layer. The 0.04 mm waste exit width had sufficient throughput and lack of recirculation and was therefore chosen to be implemented in the mesoscale device.

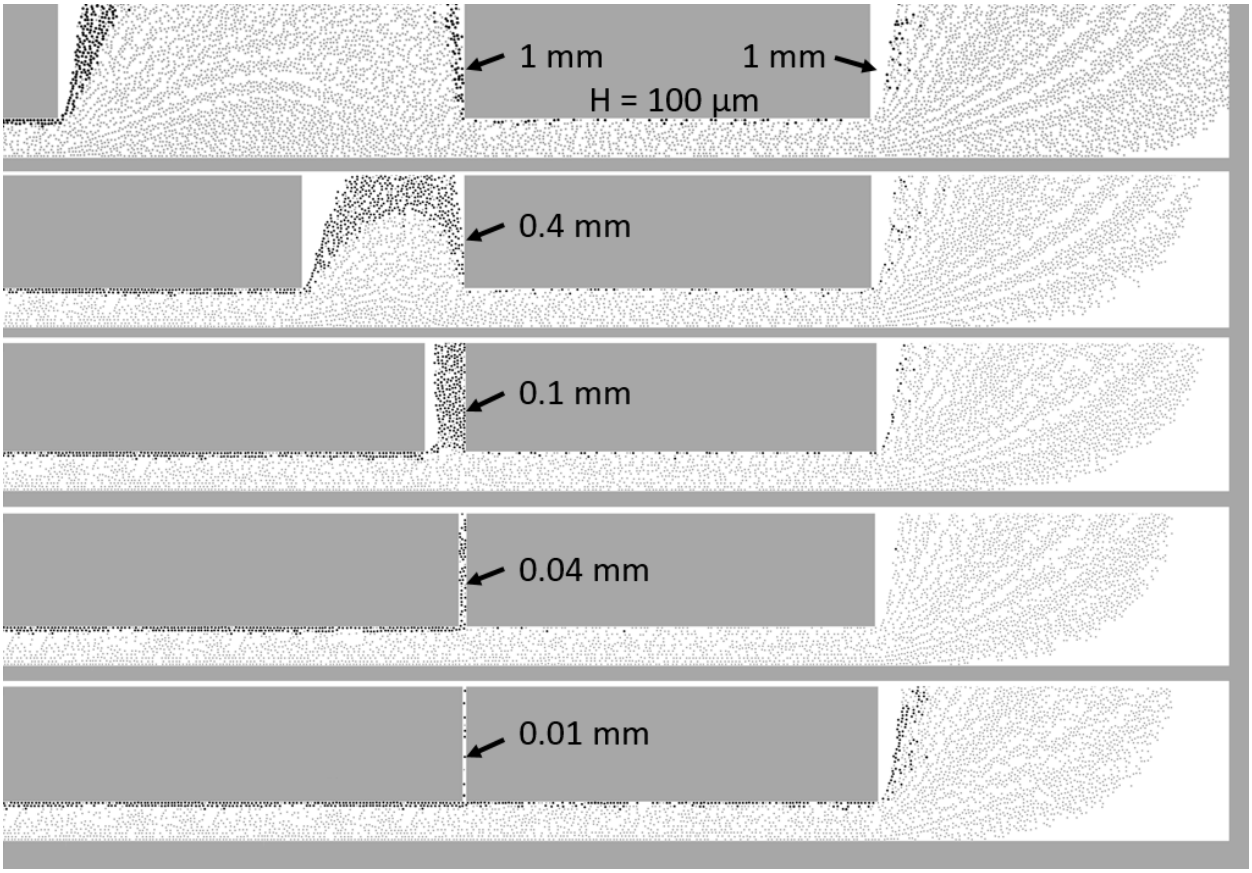

Figure 27. Simulation results for 1, 0.4, 0.1, 0.04, and 0.01 mm wide waste exits. Gray dots are healthy RBCs, black dots are paramagnetic RBCs.

3.3.5 Shear Stress Calculation Results

Table 7 lists the geometry specifications, the estimated Re, and τ for each segment (referenced in Figure 18) along the mesoscale mPharesis device from inlet to waste and outlet for Q=385 µL min^{-1} (maximum experimental flow rate). Dynamic viscosity (μ) was set to 4 cP and density (ρ) was set to 1025 kg m^{-3}, as in previous chapters.

Table 7. Reynolds number and shear stress calculations for each segment of mesoscale mPharesis device (# references segment numbering in Figure 18.)

	#	QTY	height (mm)	width (mm)	Dh (mm)	A (mm^2)	Re,max	τ,max (Pa)
INLET	**1**	1	-	-	0.79	0.49	2.6	0.064
	2	1	0.50	1.0	0.67	0.50	2.2	0.077
	3	2	0.50	1.0	1.3	1.0	2.2	0.019
	4	4	0.50	1.0	2.7	2.0	2.2	$4.8x10^{-3}$
	5	8	0.50	1.0	5.3	4.0	2.2	$1.2x10^{-3}$
	6	16	0.50	1.0	11	8.0	2.2	$3.0x10^{-4}$
	7	1	0.50	60	0.99	30	0.054	$8.6x10^{-4}$
	8	1	0.80	60	1.6	48	0.054	$3.4x10^{-4}$
WIRE ARRAY AREA	**9**	1	0.10	43	0.20	4.3	0.076	0.030
	10	1	0.050	60	0.10	3.0	0.055	0.086
	11	1	0.10	43	0.20	4.3	0.076	0.030
OUTLET	**12**	1	0.80	60	1.6	48	0.054	$3.4x10^{-4}$
	13	1	0.50	60	0.99	30	0.054	$8.6x10^{-4}$
	14	2	0.50	1.0	1.3	1.0	2.2	0.019
	15	4	0.50	1.0	2.7	2.0	2.2	$4.8x10^{-3}$
	16	8	0.50	1.0	5.3	4.0	2.2	$1.2x10^{-3}$
	17	16	0.50	1.0	11	8.0	2.2	$3.0x10^{-4}$
	18	1	0.50	1.0	0.67	0.50	2.2	0.077
	19	1	-	-	0.79	0.49	2.6	0.064
WASTE	**20**	1	0.040	60	0.080	2.4	0.054	0.13
	21	1	0.50	60	0.99	30	0.054	$8.6x10^{-4}$
	22	1	0.50	60	0.99	30	0.054	$8.6x10^{-4}$
	23	2	0.50	1.0	1.3	1.0	2.2	0.019
	24	4	0.50	1.0	2.7	2.0	2.2	$4.8x10^{-3}$
	25	8	0.50	1.0	5.3	4.0	2.2	$1.2x10^{-3}$
	26	16	0.50	1.0	11	8.0	2.2	$3.0x10^{-4}$
	27	1	0.50	1.0	0.67	0.50	2.2	0.077
	28	1	-	-	0.79	0.49	2.6	0.064

The maximum shear stress values for 385 μL min^{-1} was estimated as 0.13 Pa through the thin waste exit after the wire array (segment #20). This result, location and low value, was expected because it was the region of the device with the smallest hydraulic diameter (80 μm) and flow is creeping. This estimated shear stress value was below in vitro experimental derived hemolytic values (150 Pa)[84]. It is difficult to predict how these forces will scale in a large treatment-sized system without knowing the final design and all the additional components needed. However, the system would likely be modeled after existing, non-hemolytic blood-contacting systems.

3.3.6 metRBC Preparation Results

Six separately prepared batches of metRBCs (approximately 30 mL each) were analyzed by the hemoximeter resulting in 34.9±8.6% Hct, 0.2±0.0% HbO_2, 98.1±0.3% metHb, and 0.8±0.3% RHb. No sample collected from experiments showed visual signs of hemolysis. Figure 28 shows the elongation index (Equation 20) averaged for 50 cells for each cell type and shear rate compared to iRBC results reported for Cranston et al.[8] Cranston et al. reported that trophozoite and schizont iRBC deformability was completely abolished, thus the elongation index is equal to 1 for all three applied shear stresses. Figure 29 shows the cell membrane deformation still frames for hRBCs, metRBCs, and heat-treated metRBCs.

$$\text{elongation index} = \frac{\text{RBC width}}{\text{RBC length}} \qquad [20]$$

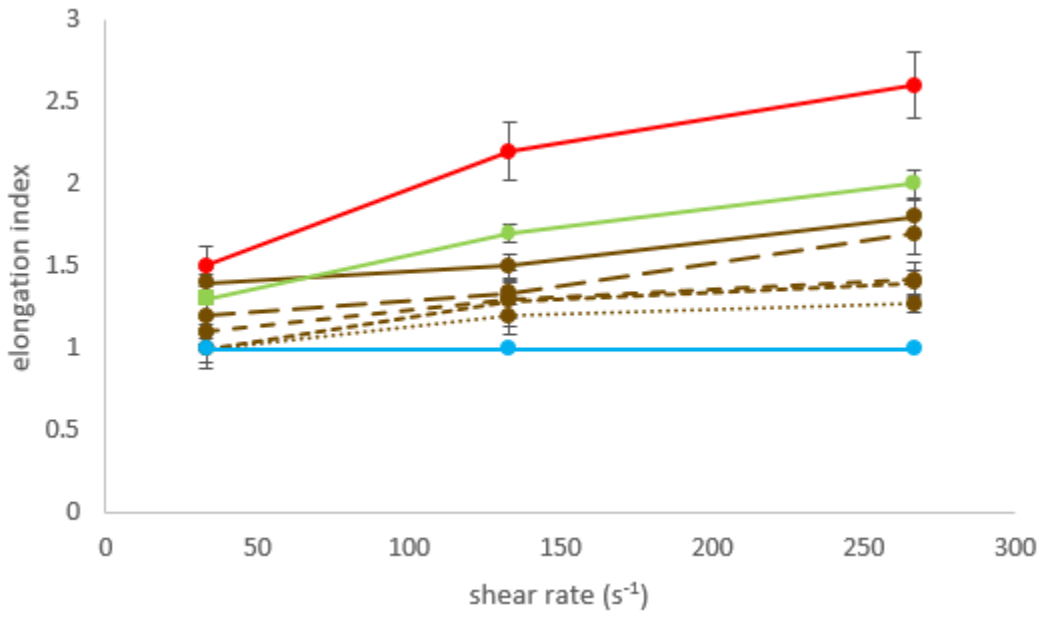

Figure 28. Elongation indices for various RBC types at shear rates for healthy cells (red), ring-stage iRBCs (green)[8], trophozoite and schizont iRBCs (blue, overlapping with no SD reported)[8], and metRBCs (brown) with different heat treatments at 48°C: 0 min (●—●), 15 min (●— —●), 30 min (●– –●), 45 min (●- -●), and 60 min (●. . .●).

Healthy RBCs had the greatest elongation index for each shear rate with values of 1.5, 2.0, and 2.6 at shear rates of 33, 133, and 266 s^{-1}. Unheated metRBCs deformed similarly to the ring-stage iRBCs (1.4, 1.5, 1.8 vs. 1.3, 1.7, 2.0). The heated metRBCs progressively lost deformability with increasing heat

treatment time. The metRBCs heat-treated for one hour became spherical, similarly reported as schizont stage iRBCs[110]. The one hour heat-treated metRBCs still deformed somewhat at 133 and 266 s^{-1} unlike the late-stage trophozoite and schizont iRBCs (1.0 1.2, 1.3 vs. 1.0, 1.0, 1.0). The mPharesis verification experiments were performed at approximately 12 to 60 s^{-1} so deformability measurements at 33 s^{-1} are most relevant this aim and will be applied later in this thesis, as well. Given the similar deformability at low shear rates and magnetic susceptibilities, unheated and heat-treated metRBCs can be applied as non-pathogenic iRBC analogs for HGMS systems.

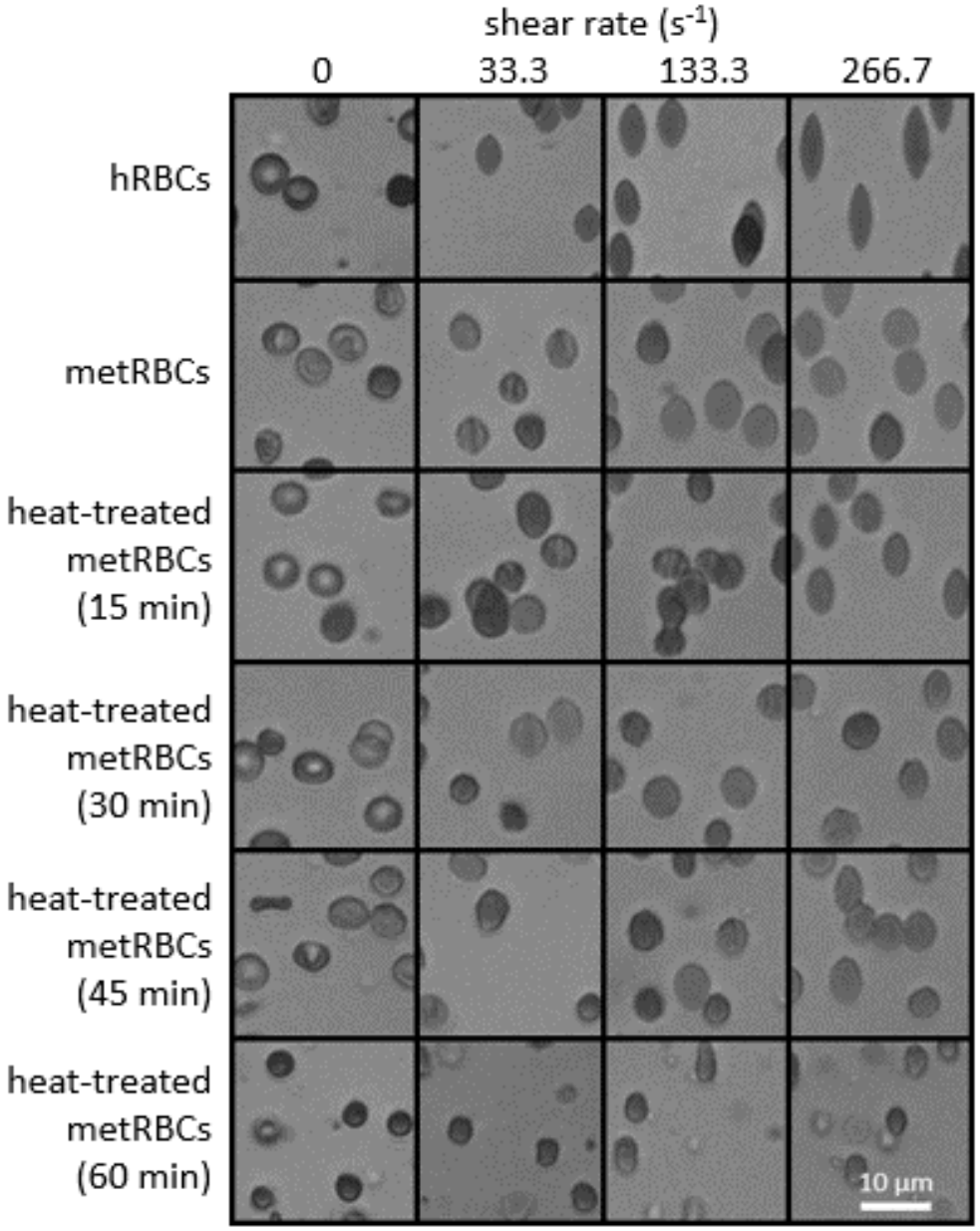

Figure 29. Deformation still frames of hRBCs, metRBCs, and heat-treated metRBCs for 15, 45, and 60 min at shear rates of 0, 33.3, 133.3, and 266.7 s^{-1}.

3.3.7 v5.0 Device Performance Results

Table 8 shows the theoretical range and ideal values for the previously described performance metrics M, η_{remove}, and η_{rescue}. The final results of the optimized v5.0 mesoscale mPharesis device are summarized in Table 8. The measured conservation of cells (M) for each condition was within ±5% which was deemed within an acceptable range of error. The one exception was at the lowest flow rate tested (39 µL min^{-1}) for

10%SR, in which M was over 30%. This was believed to be caused by drag force being insufficient to prevent adhesion of metRBCs to the ferromagnetic wires leading to metRBC build-up in the device.

Table 8. The percentage of metRBCs removed out of the blood returned to the patient (η_{remove}) and the percentage of hRBCs rescued in the waste (η_{rescue}) using for mPharesis verification experiments in a single pass. * indicates rejected results where reasonable conservation of mass was not maintained.

Condition	n	Q (μL min^{-1})	SR	η_{remove}	η_{rescue}
1	3	77	5%	7.2±0.3%	96.3±0.6%
2	21		10%	27.0±2.2%	96.1±1.4%
3	3		20%	21.8±1.7%	96.4±1.3%
4*	3	39	10%	39.0±5.4%*	97.2±1.8%*
5	3	154		14.6±1.0%	96.0±0.7%
6	3	231		16.7±1.2%	96.7±0.8%
7	3	308		15.0±1.8%	97.8±0.5%
8	3	385		11.5±0.3%	97.0±0.3%

Detailed M, η_{remove}, and η_{rescue} values are reported in Appendix B. The measured conservation of mass for each condition was within ±5% which was deemed within an acceptable range of error. The one exception was at the lowest flow rate tested (39 μL min^{-1}) for 10%SR, in which the conservation of mass was greater than -30% for metRBCs. This loss was believed to be caused by drag force being insufficient to prevent adhesion of metRBCs to the ferromagnetic wires leading to metRBC build-up in the device. The resultant average η_{remove} and η_{rescue} values for all conditions with no magnet varied from -3.0 to 3.1% with standard deviations under 1.9%, which was deemed within an acceptable range of error. The η_{remove} and η_{rescue} results for the magnet conditions are listed in **Error! Reference source not found.**. The ondition that exhibited the best performance overall was 77 μL min^{-1} at 10%SR. In this case the reduction in metRBCs measured at the outlet was 27.0% (η_{remove}=-27.0±1.2%) with the %metRBC reduced from 22.1% in the inlet to 19.0% at the outlet. The depletion of healthy RBCs at the outlet was negligibly small (η_{rescue}=2.2±0.5%), while 10% of flow is removed through the waste (since SR=10%) that must be replaced with donor blood, there was nearly zero excess loss of healthy RBCs.

Table 9 compares the paramagnetic RBC removal rate of other HGMS devices compared to mPharesis described with Equation 21.

$$Q_{paraRBC} = Q_{in} * Hct * \eta_{remove} \quad [21]$$

The mPharesis prototype reported here achieved the desired goal of selectively removing paramagnetic RBCs at about 1.2 μL min^{-1}, a removal throughput is approximately 400 to 700 fold greater and provides the advantage of processing whole blood. Additionally, unlike all other successful published continuous paramagnetic RBC HGMS devices, mPharesis is non-dilutive and thus applicable to treatment applications where low Hct is a very common and important concern. Although the performance of the mesoscale v5.0 mPharesis device was far from ideal, it was within the acceptable range for the intended application, i.e. to treat a patient with hyperparasitemia, within 4 hours. Scaling of these results into a treatment system will be discussed in the next chapter.

Table 9. Comparison of mPharesis throughput to other HGMS devices for separation of paramagnetic RBCs.

	mPharesis v5.0	**Nam et al.[65]**		**Han et al.[86]**	**Qu et al.[87]**
paramag RBC type	metRBC	early-stage iRBC	late-stage iRBC	deoxyRBC	metRBC
Q (μL min^{-1})	77	0.08	0.08	0.083	0.23
paramag RBC Hct	6%	0.3%	0.3%	~4%	~1%
η_{remove}	27%	73%	99.2%	93.5%	93.7%
paramag RBC removal rate (Q*Hct*Δ, μL min^{-1})	1.2	0.0018	0.0024	~0.0031	~0.0022

There were many factors not included in this experimental approach that affect separation such as the parasitemia, hematocrit, temperature, and RBC age. For RBC-saline suspensions, the lack of platelets and proteins in whole blood eliminates significant shear-dependent suspension viscosity contributions (particularly with low-shear conditions present in this thesis) and clotting factors. Shear-dependent factors, such as RBC aggregation and shear thinning, affect the motion of RBCs within the separation flow field. The lack of shear-dependent factors could have been mediated by the addition of albumin or fibrinogen to the suspending fluid. However, thesis advisor and expert hemorheologist Dr. Marina V.

Kameneva recommended against albumin, as it is ineffective at significantly replicating the rheologic contributions of plasma, and against fibrinogen, as it degrades rapidly into byproducts that cause super-physiological aggregation. The lack of clotting factors was not a concern because an ultimate treatment-scale system are assumed to be fully anti-coagulated.

Due the high concentration of red blood cells in the flow field, cell-cell collisions likely have a significant role preventing separation of the paramagnetic RBCs. An additional limitation is the use of metRBC and hRBC suspension in PBS as a substitute for whole blood containing iRBCs. However, as stated previously, *P. falciparum* iRBC cultures with elevated parasitemia, as seen in severe malaria-patients, are very difficult to sustain in-vitro. It is likely that the performance can be further improved with continued optimization of the design and fabrication methods.

3.4 Conclusions

In this specific aim, a novel mesoscale HGMS device was designed, fabricated, and experimentally verified using an iRBC analog with 30% Hct blood with 20% metRBCs for a range of hemodynamic parameters. The device was successfully selectively removed 27% of metRBCs entering the device at a rate of 77 $\mu L\ min^{-1}$ and waste split ratio of 10%. A magnet and wire array combination to maximize magnetic force were not intuitive, but implementation of computational simulations described here enabled quick selection. Fabrication of a microfluidic flow field without micron-scale defects proved to be the greatest limitation in this project. The creation of a stable non-infectious iRBC analog, that can be made benchtop in large volumes with the option to further rigidify cells, is an important contribution that now can be used to verify other large scale iRBC HGMS systems. Further improvement of the magnet and wire array design is needed. Experiments using clinically relevant iRBC cultures and whole blood are needed to further verify this device. These successful results prove promising and motivated the development of an iRBC clearance model for severely ill malaria patients treated with a scaled-up mPharesis system, explored in Specific Aim 2.

4 Perform Simulations to Compare the Parasite Clearance and Hemodilution with Combination Exchange Transfusion-Drug and mPharesis-Drug Therapies

4.1 Introduction

Falciparum malaria parasites are incredibly efficient multipliers, often increasing between 5 and 20 times during their 48 hour intra-erythrocytic asexual reproduction cycle. This multiplication is especially evident in many non-immune travelers that acquire the disease during a vacation. Malaria is highly synchronous with marked rises and falls in peripheral parasitemia percentages corresponding to the infection's merogony stage (search for a host RBC for replication) and sequestration in the peripheral capillary beds. In un-treated infections, this cycling eventually settles into a rough plateau followed by a gradual decline in parasite counts over weeks or months during which the parasitemia shows peaks or waves approximately every 9 cycles (18 days). Falciparum malaria is the most rigorous of the malaria species. It only sequesters for half of the life cycle of other *Plasmodium* strains and the parasite burdens are generally heavier.

For non-resistant malaria infections, there is an abrupt and dramatic change of parasitemia in the host's circulating blood once quinine or artemisinin-derived antimalarial drugs are administered to a patient. Parasites, that were previously circulating and unrecognized by the host's immune systems just hours before, are now identified and cleared. No antimalarial drugs act instantaneously, even if given intravenously, thus the decrease in parasitemia is gradual at first. Then, the majority of parasites emerge from their sequestrated "hiding places" over a period of several hours to reproduce and the drug attacks causing a sharp exponential decay in parasitemia as the treatment takes effect[14,105,111,112]. Figure 30 demonstrates parasite clearance curves for different drugs and their approximate parasite reduction ratios (PRR)[113].

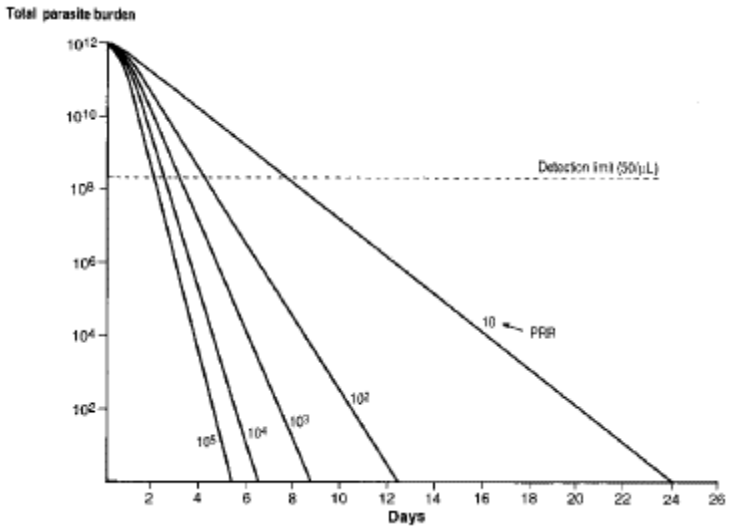

Figure 30. Approximate parasite clearance curves for different drugs and patient conditions[113]. Larger parasite reduction ratio (PRR) values indicate a more effective parasite kill rate by a certain drug.

PRRs do not full describe all aspects of the therapeutic response of the malaria parasite to antimalarials. There are many other patient-specific factors involved: native immunity, sequestration percentages, therapeutic responses to a particular drug, combinatorial drug synergy, development of drug resistance during treatment, etc. The highest PRRs reported of all available antimalarial drugs, such as many combination artesunate-mefloquine therapies, can destroy 99.999% of parasites per cycle (PRR of 10^5 over 48 hours) and maintain parasite-killing levels within the blood for at least 3 cycles. Less effective drug therapies have a PRR of 10^2 meaning the infection is mostly cleared in about 7 days. However, with low PRR values, recrudescence is highly probable[114,115].

While drug therapies have been effective in reducing falciparum malaria mortality since the discovery of quinine centuries ago, the continued rise of quinine and artemisinin resistance has become a lethal problem in endemic regions[11,12]. In patients with high parasitemia (>5%[52]), moderate to severe anemia (less than 30% Hct[52]), or those infected with a drug-resistant malaria strain, exchange transfusion (ET) is a critical treatment option. As discussed previously, many clinicians disagree about the balance between advantages and drawbacks of drug therapies and their associated complications. Nevertheless, clinicians generally agree that new treatment methods must be implemented to attempt to reduce the ongoing malaria epidemic and handle the increasing amount of drug-resistant malaria strains. ET alleviates

concurrent anemia, removes 100% of iRBCs via the blood removed, and replaces the drained blood with healthy cells. However, in malaria endemic regions, a more efficient system is needed to reduce the large volume of blood needed for ET (500 to 10,000 mL or 1 to 20 units of blood[2]) that is often reported used to save critically ill patients.

No treatment system exists to selectively filter out iRBCs from a severe malaria infected patient's blood. mPharesis provides a potential solution. In this specific aim, a novel theoretical model was developed to describe the parasite clearance and Hct level changes in patients receiving combination ET-drug and mPharesis-drug therapies. The model was then calibrated and compared to 10 case studies of severe malaria patients successfully treated with combination ET-drug therapies. The final calibrated model was compared to combination ET-drug treatments across different flow rates, treatment times, initial patient parameters, and mPharesis iRBC removal efficiencies. The goal is to use this model to provide treatment time, donor blood needed, and real-time parasite levels estimates for severely-ill malaria infected patients using a treatment-scale mPharesis procedure.

4.2 Methods

4.2.1 Equation Development

Alexander Wiener and Karl Landsteiner were the first to derive a formula to describe the residual fraction of RBCs during ET with a simple first-order rate equation[116]. This can be written as an exponential decay equation ($C=C_i*e^{-A*t}$) where C is concentration and A is rate of concentration change with time t. For Wiener and Landsteiner, A was simply the ratio of exchanged volume to patient volume. However, this derivation does not consider the difference between the patient's Hct and infused Hct. To begin building a clearance model for ET-drug and mPharesis-drug treatments, the factors effecting the changes in parasitemia (Para) and Hct were visualized in Figure 31. Solid arrows indicate factors described by first-order rate kinetic equations and dashed arrows indicate scalar factors. Parasite clearance was dictated by effectiveness of antimalarials, iRBCs lost in blood drainage, and/or by selective removal such as with mPharesis. The clearance of iRBCs by drugs and other innate factors, lumped together here as A_{drug}, was

simplified with no initial lag period seen in Figure 30. The initial lag period describes the parasite clearance directly after drug is given, often hours before ET is administered, and thus was assumed to not be significant here.

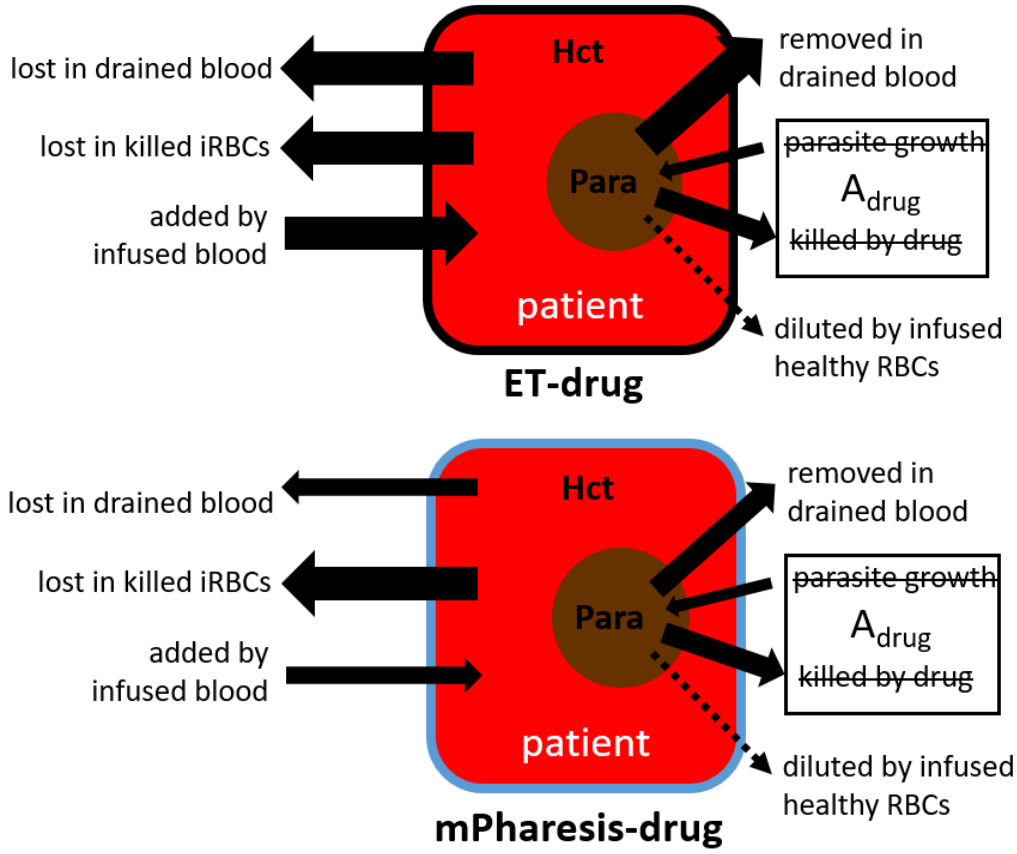

Figure 31. Diagrams describing the factors effecting changes in parasitemia and Hct in patients receiving ET-drug and mPharesis-drug combination therapies. Solid arrows indicate factors described by first-order rate kinetic equations (i.e. exponential decays) and dashed arrows indicate scalar factors. The thickness of each arrow approximates the relative contribution of each factor. Parasite growth and the parasite kill rate term are combined into an A_{drug} term for both therapies.

The contribution of parasite growth was assumed negligible over the short time frame of an ET. Parasite growth is difficult to discern from the drug kill term, thus both were combined into the A_{drug} term in this model.

4.2.1.1 ET-Drug Model

$Para_{ET}$ was the change in parasitemia from the initial value during ET-drug therapy. This value was influenced by the factor A_{drug} ($Para,drug_{ET}$, Equation 22) and iRBCs lost in the ET drainage ($Para,drain_{ET}$, Equation 23). The parasitemia was also influenced by the total Hct, meaning the increase in Hct from

infused blood dilutes and decreases the concentration of circulating iRBCs (Para,dilute$_{ET}$, Equation 24). Para$_{ET}$ was calculated in Equation 25.

$$\text{Para, drug}_{ET}(t) = \text{Para}_i * e^{A_{drug}t} \quad [22]$$

$$\text{Para, drain}_{ET}(t) = \text{Para}_i * e^{\frac{Q_{ET\ drain}}{k*Vol,pt}t} \quad [23]$$

$$\text{Para, dilute}_{ET}(t) = \text{Para}_i \left(\frac{\text{Hct}_i}{\text{Hct}_{ET}(t)}\right) \quad [24]$$

$$\text{Para}_{ET}(t) = \text{Para, drug}_{ET}(t) * \text{Para, drain}_{ET}(t) * \text{Para, dilute}_{ET}(t)$$

$$= \text{Para}_i * e^{\left(\frac{Q_{ET\ drain}}{k*Vol,pt}+A_{drug}\right)t}\left(\frac{\text{Hct}_i}{\text{Hct}_{ET}(t)}\right) \quad [25]$$

Para$_i$ is initial parasitemia, Hct$_i$ is initial Hct, Hct$_{ET}$ is the variable Hct during therapy, $Q_{ET,drain}$ is the ET drainage flow rate, k is the ratio between body and venous Hct (0.91)[117], and Vol,pt is patient blood volume. The contribution of Equation 23 depends on patient blood volume. Patient blood volume was used in the model as opposed to cardiac output. Though cardiac output can be measured precisely in technologically-capable hospitals, these techniques are not available in most malaria-endemic regions. Blood volume can be estimated using gender and age specific equations described by anesthesiologists Morgan et al[118]. The efficiency value of removing iRBCs via drained blood was 100% because all iRBCs in the drained blood are discarded.

Patient hematocrit during ET-drug therapy, Hct$_{ET}$, was increased by the hRBCs given in the donor blood infusion (Hct,infuse$_{ET}$, Equation 26) and iRBCs killed via A_{drug} (Hct,drug$_{ET}$, Equation 27). Hct$_{ET}$ was calculated in Equation 28.

$$\text{Hct, infuse}_{ET}(t) = (\text{Hct}_{ET\ infuse} - \text{Hct}_i)\left(1 - e^{\frac{Q_{ET\ infuse}}{k*Vol,pt}t}\right) \quad [26]$$

$$\text{Hct, drug}_{ET}(t) = \text{Hct}_i * \text{Para}_i - \text{Hct}_{ET}(t)e^{A_{drug}*t}(t) * \text{Para}_i \quad [27]$$

$$\mathrm{Hct_{ET}(t) = Hct_i + Hct, infuse_{ET}(t) - Hct, drug_{ET}(t)}$$
$$= \mathrm{Hct_i} + (\mathrm{Hct_{ET\,infuse}} - \mathrm{Hct_i})\left(1 - e^{\frac{Q_{ET\,infuse}}{k*Vol,pt}t}\right)$$
$$- \left(\mathrm{Hct_i} * \mathrm{Para_i} - \mathrm{Hct_{ET}(t)}e^{A_{drug}*t}(t) * \mathrm{Para_i}\right)$$

[28]

$Hct_{ET\ infuse}$ is the Hct of the infused donor blood during therapy and $Q_{ET,infuse}$ is the ET infusion flow rate.

4.2.1.2 mPharesis-Drug Model

For the mPharesis-drug therapy (mP), $Para_{mP}$ was the change in parasitemia from the initial value during treatment influenced by the factor A_{drug} ($Para,drug_{mP}$, Equation 29) and iRBCs lost in the waste drainage ($Para,drain_{mP}$, Equation 30). iRBCs were removed selectively by the factor A_{mP}, equal to the best performance value η_{remove} from Chapter 3 ($Para,selective_{mP}$, Equation 31). The parasitemia was also influenced by the total Hct ($Para,dilute_{mP}$, Equation 32). $Para_{mP}$ was calculated in Equation 33.

$$\mathrm{Para, drug_{mP}(t) = Para_i} * e^{A_{drug}\,t} \quad [29]$$

$$\mathrm{Para, drain_{ET}(t) = \ Para_i} * e^{(p*SR)\frac{Q_{mP\,drain}}{Vol,pt}t} \quad [30]$$

$$\mathrm{Para, select_{mP}(t) = Para_i} * e^{(1+p*SR)A_{mP}\,t} \quad [31]$$

$$\mathrm{Para, dilute_{mP}(t) = Para_i}\left(\frac{\mathrm{Hct_i}}{\mathrm{Hct_{mP}(t)}}\right) \quad [32]$$

$$\mathrm{Para_{mP}(t) = Para, drug_{mP}(t) * Para, drain_{mP}(t) * Para, selective_{mP}(t) * Para, dilute_{mP}(t)}$$
$$= \mathrm{\ Para_i} * e^{\left(A_{drug}+(p*SR)\frac{Q_{mP\,drain}}{k*Vol,pt}+(1+p*SR)A_{mP}\right)t}\left(\frac{\mathrm{Hct_i}}{\mathrm{Hct_{mP}(t)}}\right)$$

[33]

Hct_{mP} is the variable Hct during therapy and $Q_{mP,drain}$ is the mPharesis drainage flow rate.

A re-filtration step was considered during development of the mPharesis model where p is the number of re-filtration steps. In a re-filtration step, blood removed via the waste exit of the mPharesis system is re-processed in a secondary parallel mPharesis module. The re-filtered blood then joins the primary mPharesis outlet flow and is returned to the patient while the secondary waste was discarded. The addition of a re-filtration step scaled A_{mP} by (1+p*SR) and decreased $Q_{mP\ drain}$ by (p*SR).

Patient hematocrit during mPharesis-drug therapy, Hct_{mP}, was increased by the hRBCs given in the donor blood infusion ($Hct,infuse_{mP}$, Equation 34), iRBCs killed via A_{drug} ($Hct,drug_{mP}$, Equation 35), and iRBCs selectively removed via A_{mP} ($Hct,selective_{mP}$, Equation 36). A_{mP} was negative because it removes iRBCs. Hct_{ET} was calculated in Equation 37.

$$\mathrm{Hct,infuse_{mP}}(t) = (\mathrm{Hct_{mP\ infuse}} - \mathrm{Hct_i})\left(1 - e^{(p*SR)\frac{Q_{mP\ infuse}}{k*Vol,pt}t}\right) \quad [34]$$

$$\mathrm{Hct,drug_{mP}}(t) = \mathrm{Hct_i} * \mathrm{Para_i} - \mathrm{Hct_{mP}}(t)e^{A_{drug}*t}(t) \quad [35]$$

$$\mathrm{Hct,selective_{mP}}(t) = \mathrm{Hct_i} * \mathrm{Para_i} - \mathrm{Hct_{mP}}(t)e^{(1+p*SR)A_{mP}*t}(t) * \mathrm{Para_i} \quad [36]$$

$$\begin{aligned}\mathrm{Hct_{mP}}(t) &= \mathrm{Hct_i} + \mathrm{Hct,infuse_{mP}}(t) - \left(\mathrm{Hct,drug_{mP}}(t) * \mathrm{Hct,selective_{mP}}(t)\right)\\ &= \mathrm{Hct_i} + (\mathrm{Hct_{mP\ infuse}} - \mathrm{Hct_i})\left(1 - e^{(p*SR)\frac{Q_{mP\ infuse}}{k*Vol,pt}t}\right)\\ &\quad - \left(\mathrm{Hct_i} * \mathrm{Para_i} - \mathrm{Hct_{mP}}(t)e^{(A_{drug}+(1+p*SR)A_{mP})t}(t) * \mathrm{Para_i}\right)\end{aligned} \quad [37]$$

$Hct_{mP\ infuse}$ is the Hct of the infused donor blood during therapy and $Q_{mP,infuse}$ is the donor blood infusion flow rate. Equations 25 and 28 as well as Equations 33 and 37 were simultaneously solved in Mathematica (Wolfram, Champaign, IL, USA) to produce Equations 38 through 41.

$$\mathrm{Para_{ET}}(t) = -\frac{e^{-2*A,drug*t-\frac{Q,drain\ ET*}{k*Vol,pt}t+\frac{Q,infuse\ ET}{k*Vol,pt}t}\mathrm{Hct_i}(e^{Adrug*t}-\mathrm{Para_i})\mathrm{Para_i}}{-\mathrm{Hct_i}+\mathrm{Hct_{infuse\ ET}}-e^{\frac{Q,infuse\ ET}{k*Vol,pt}t}\mathrm{Hct_{infuse\ ET}}+e^{\frac{Q,infuse\ ET}{k*Vol,pt}t}\mathrm{Hct_i}\mathrm{Para_i}} \quad [38]$$

$$\mathrm{Hct_{ET}(t)} = -\frac{e^{A,drug*t-\frac{Qinfuse\ ET}{k*Vol,pt}t}(-\mathrm{Hct_i}+\mathrm{Hct_{infuse\ ET}}-e^{\frac{Q,infuse\ ET}{k*Vol,pt}t}\mathrm{Hct_{infuse\ ET}}+e^{\frac{Q,infuse\ ET}{k*Vol,pt}t}\mathrm{Hct_i Para_i})}{e^{A,drug*t}-\mathrm{Para_i}} \quad [39]$$

$$\mathrm{Para_{mP}(t)} = -\frac{e^{-2(1+p*SR)A,device*t-2A,drug*t}\mathrm{Hct_i}(e^{(1+p*SR)A,device*t+A,drug*t}-\mathrm{Para_i})\mathrm{Para_i}}{-\mathrm{Hct_i}+\mathrm{Hct_{infuse\ mP}}-e^{(p*SR)\frac{Q,mP\ drain}{k*Vol,pt}t}\mathrm{H_{infuse\ mP}}e^{(p*SR)\frac{Q,mP\ drain}{k*Vol,pt}t}\mathrm{Hct_i Para_i}} \quad [40]$$

$$\mathrm{Hct_{mP}(t)} = e^{(1+p*SR)A,device*t+A,drug*t-(p*SR)\frac{Q,mP\ drain}{k*Vol,pt}t}(-\mathrm{Hct_i} + \mathrm{Hct_{infuse\ mP}} - e^{(p*SR)\frac{Q,mP\ drain}{k*Vol,pt}t}\mathrm{Hct_{infuse\ mP}} + e^{(p*SR)\frac{Q,mP\ drain}{k*Vol,pt}t}\mathrm{Hct_i Para_i})/(e^{(1+p*SR)A,device*t+A,drug*t} - \mathrm{Para_i}) \quad [41]$$

4.2.2 Model Calibration

Many model parameters listed in the previous section are commonly measured or known in hospital settings and were applied to this model directly. These parameters included initial Hct and Para, final Hct and Para, Q_{drain}, and Q_{infuse}. A_{mP} was constrained from the previous chapter and Vol,pt was calculated as described previously. However, some parameters were unknown such as A_{drug} and the average Hct_{infuse}. Hct_{infuse} is variable throughout ET treatments because donor blood is given as different combinations of whole blood, packed RBCs, FFP, and/or donor platelets. For these unknown parameters, the model was calibrated using published case reports.

10 ET case studies[21,54,55,106,107] were applied to Equations 37 through 40. The case parameters are listed in Table 10. All patients met the WHO's specifications for severe malaria upon admission[52], received antimalarials in the form of intravenous or oral drugs, survived treatment, and made full recoveries. Manual treatments were employed during emergency situations or when automated resources were not available. Automated treatments were implemented using a COBE Spectra automated apheresis system to transfuse to a specific patient hematocrit and volume. Parameters in Table 10 marked with an asterisk (*) were estimated before model calibration. Estimated patient blood volumes were approximated for their given gender, age, height, and weight when given. ET drainage volume, when not reported, was assumed to be equal to infusion volumes for an isovolumetric treatment. Treatment was assumed to be continuous

as the effect of cycling during ET is negligible for large exchanges used with anemic, hyperparasitized malaria patients[119]. The model was calibrated using only two unknown parameters for each case: average Hct_{infuse} (or Hct_f for case 7) and A_{drug} were adjusted until the ET model's final calculated Hct and parasitemia for the matched the reported value (forced interception). The only exception was with the exception of case 7 where infusion Hct is known and final Hct was adjusted. The maximum $Hct_{mP\ infuse}$ was set as 50%, representing the customary reconstituted whole blood Hct used since the 1950s[116]. $Q_{mP\ infuse}$ was set equal to $Q_{mP\ drain}$ for an isovolumetric treatment, which is most common.

Table 10. Case study parameters for 10 patients successfully treated with combination drug and ET therapies. * indicate unreported variables estimated before calibration, ** indicates parameters estimated during calibration.

	1	2	3	4	5	6	7	8	9	10
Author, year	Zhang 2001	Zhang 2001	Zhang 2001	Deshpande 2003	Deshpande 2003	Hall 1985	Boctor 2005	Macallan 1999	Macallan 1999	Macallan 1999
Age, gender	28 yo male	45 yo male	5 yo female	12 yo male	10 yo male	38 yo female	9 yo female	39 yo female	26 yo female	38 yo male
ET type	Auto	Auto	Auto	Auto	Auto	Manual	Manual	Manual	Manual	Manual
Vol,pt (mL)	5000*	5000*	1600*	2500	2800	4800*	2300*	4200*	4200*	5000*
Hct_i	36.6%	24.4%	20%	21%	15%	25.5%	33.2%	19.8%	36.2%	35.9%
Hct_f	36%	29%	30%	33%	26.7%	24.3%	-	26%	36.3%	30.6%
$Para_i$	22.5%	45%	40%	75%	67%	26%	32%	28%	23%	35%
$Para_f$	3%	6.0%	1%	18%	8%	5%	2%	2.4%	2.3%	9%
SR	10%	10%	10%	10%	10%	10%	10%	10%	10%	10%
A_{mP} (% min^{-1})	0.6%	1.4%	0.75%	2.2%	1.21%	0.42%	0.19%	0.47%	0.52%	0.33%
t,ET (min)	83	68	133	90	90	130	240	120	120	120
Vol,ET infuse (mL)	5415	2500	2088	1500	2300	6750	1800	3600	4400	5400
Vol,ET drain (mL)	5415*	2500*	2088*	1700	2400	5000	1200	3000	2800	3500
Average Q,ET infuse (mL min^{-1})	65.2	36.8	15.7	16.7	25.6	51.9	7.5	30.0	36.7	45.0
Average Q,ET drain (mL min^{-1})	-65.2	-36.8	-15.7	-18.9	-26.7	-38.5	-5.0	-25.0	-23.3	-29.2

4.2.3 Treatment Method Comparison

The efficacy of ET-drug and mPharesis-drug therapies was compared for all 10 cases. First, blood access flow rate was constrained to the maximum commonly employed in continuous renal replacement therapy

(CRRT). Q_{max} was calculated as Vol,pt*BAR with blood access ratio (BAR) as approximately 0.1 min^{-1}, an approximate calculation used for CRRT[120]. Then, Hct_{infuse} and time were adjusted until the projected final parasitemia and Hct matched the given values for ET in the case reports (i.e. forced interception). Final donor RBC volumes (equal Hct) and times were compared between treatment types. The inclusion of a re-filtration step was evaluated for case #1 to determine its utility before calibrating the model and comparing all 10 cases.

4.2.4 Treatment-scale System Applications

Two reference charts were created to predict the time and donor blood volumes needed for theoretical treatment-scale mPharesis-drug procedures for a range of patient sizes and disease severities. Initial and final Hct and Para were applied. $Q_{mP\ infuse}$ was chosen based on the results from the previous sections. Treatments were isovolumetric. Two final target treatment parameters were chosen: a standard treatment with the final values for severe malaria and anemia defined by WHO (Para<5% and Hct>30%)[52] as well as a more extensive treatment for increased assurance of long-term patient recovery (Para<1% and Hct>40%). To ensure conservative treatment estimations, A_{drug} was set to the lowest value calculated during ET-drug therapy model calibration the referenced ET case reports.

A final system size for the mPharesis treatment was estimated based on maximum blood access flow rates for CRRT. Size feasibility was discussed. Equation 42 calculated the size of a treatment scale mPharesis system by linearly scaling single mesoscale devices in parallel from Chapter 3.

$$\text{System height} = \frac{Q_{system}}{Q_{mP}} * \frac{W_{system} * L_{system}}{w_{mP} * l_{mP}} * \left(T_{mP} + T_{magnet}\right) \quad [42]$$

w_{mP} is the width of the mesoscale device flow field (43 mm) l_{mP} is the length of the mesoscale flow field (54 mm), T_{mP} is the thickness of the entire mesoscale device (3 mm), and T_{magnet} is the thickness of the magnet array (13 mm). The treatment-scale's footprint size (W_{mP} and L_{system}) was constrained to be 430 mm wide by 540 mm long (10 by 10 mesoscale devices), similar to a common CRRT system footprint.

4.3 Results and Discussion

4.3.1 Model Calibration Values

Figure 32 shows calibration of the ET-drug model for case #1 via forced interception with the reported ET-drug therapy $Para_f$ and Hct_f values (● and ■, respectively). Table 11 lists calibrated parameters (A_{drug}, Hct_{infuse} or Hct_f) for 10 ET-drug case reports.

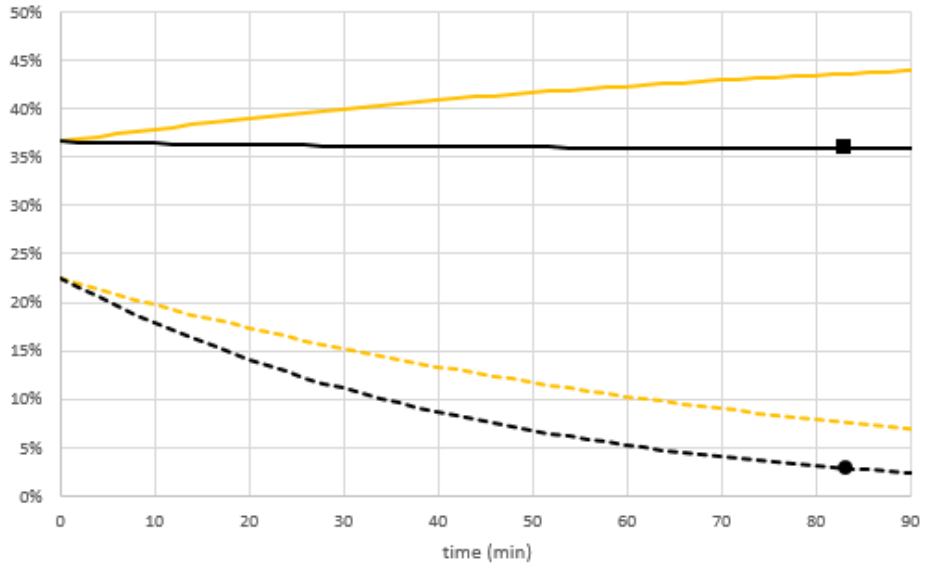

Figure 32. Example of model calibration for ET-drug therapy case #1. Included is the uncalibrated model (Hct,infuse=Hct,i, A,drug=0%) (yellow), the calibrated ET-drug model (black), the reported ET-drug case values Para,f (●) and Hct,f (■). Solid line is Hct(t), dashed is Para(t).

Table 11. Calibration parameters and treatment comparison for 10 patients successfully treated with ET-drug therapies versus mPharesis-drug.

	1	2	3	4	5	6	7	8	9	10
Hct(final)	-	-	-	-	-	-	36%	-	-	-
Hct,ET infuse (avg)	36%	46%	35%	42%	32%	23%	-	32%	39%	30%
A_{drug} (% min^{-1})	-1.4%	-2.3%	-1.7%	-0.8%	-1.1%	-0.7%	-1.0%	-1.3%	-1.5%	-1.0%

For most treatments, final Hct is the limiting variable with final Para reached before anemia is resolved. Otherwise, the infusion Hct is reduced until both final variables are reach simultaneously to minimize the amount of donor cells needed as much as possible. A_{drug} was negative in each case (i.e. exponential decrease) likely because the parasite growth rate was less than the drug and immunologic kill rate in patients receiving chemotherapy and ET in hospital settings. The contribution of iRBC elimination by

A_{drug} is significantly less than that from magnetic apheresis (A_{MA}=-27%) and comparable to cells lost to in the drained blood (Q_{drain}/Vol,pt=-0.22 to -1.3%). The PRR values reported by White et al. correspond to A_{drug} values of -0.16% (10^2, less effective drugs) to -0.4% (10^5, most effective drugs). The A_{drug} values used here range from -0.7% to -2.3%, larger than reported PRR values, thus must not represent PRR solely and, as suspected, includes other innate factors such as parasite growth and immunity. Retrospective reports often state the efficacy of an antimalarial drug is closely related to the rate at which parasites are cleared from the peripheral circulation, however, it is difficult to relate this effect to sequestered parasites[121]. Thus, it is a great likelihood that ET treatment boosts the patient's innate ability to fight the infection beyond simple drug therapy. ET therapies may quickly unload the parasite burden and/or circulating cytotoxins from the patient while also flushing out "hidden" sequestered iRBCs which would have remain dormant and non-targetable with drug therapies. Future clinical studies could be performed to isolate the contribution of these innate factors separately.

4.3.2 Re-filtration Step Consideration

Figure 33 shows case #1 with the inclusion of a single re-filtration step. The flow rate used for the re-filtration model was 500 mL min^{-1} (calculated Q_{max} based on Vol,pt). The inclusion of a re-filtration step here reduced the amount of waste blood by 90% (415 vs. 4150 mL in 83 min) and allowed for an increased parasite removal efficiency. However, even at the maximum flow rate, the modified system was unable to boost patient Hct quickly enough which is absolutely needed for severely anemic patients to survive. This was due to the fact that the rate of blood removal and replacement, even with maximum infusion Hct, was too low. Thus, a re-filtration step was not ultimately included in the final model (i.e. p was set to 0).

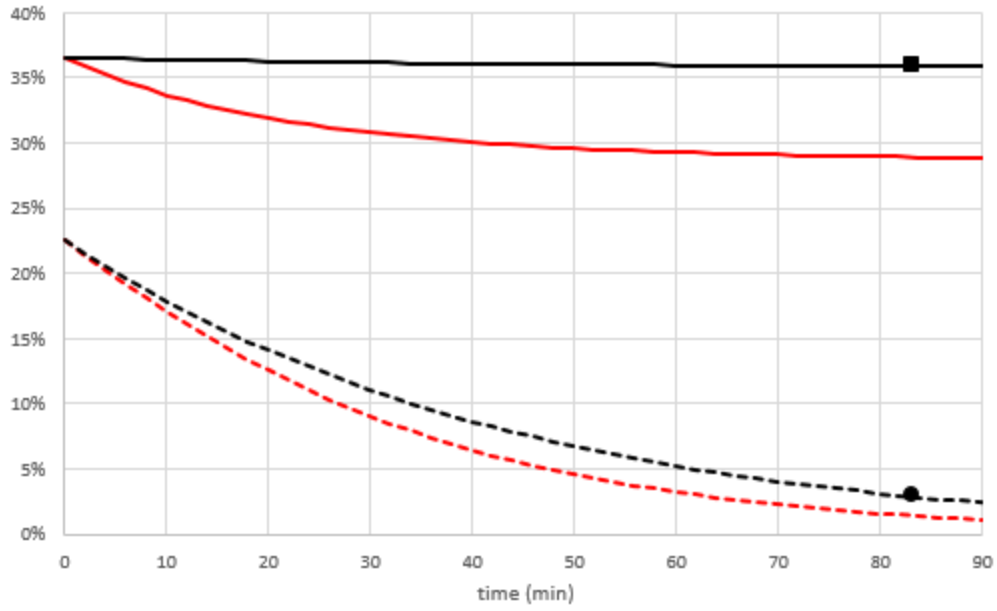

Figure 33. Comparison of ET-drug (black) and mPharesis-drug treatment with a re-filtration step (red) for case #1. The mPharesis treatment was unable to match the ET treatment with maximum constraints here (Hct,infuse=65%, Q,mP infuse=Q,max=455 mL min^{-1}). Reported ET-drug case values Para,f (●) and Hct,f (■). Solid line is Hct(t), dashed is Para(t).

4.3.3 Treatment Method Comparison

Figure 34 shows two examples of the calibrated ET-drug model compared to mPharesis-drug treatments with $Q_{mP,infuse}$ constrained to a maximum. Table 12 lists treatment parameters for calibrated ET-drug and mPharesis-drug treatments. Total donor RBC volumes needed and treatment times (when applicable) were compared between treatment methods.

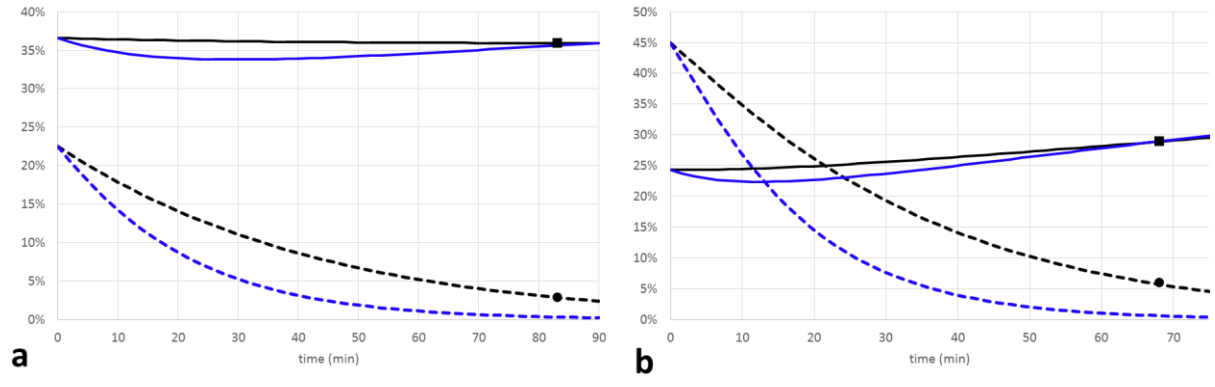

Figure 34. Example of ET-drug therapy compared to mPharesis-drug treatment where time and flow rate are constrained. Included is the calibrated ET-drug model (black), mPharesis-drug model where Q,mP infuse=Q,max (blue). a) Case #1 and b) case #2. Reported ET-drug case values Para,f (●) and Hct,f (■). Solid line is Hct(t), dashed is Para(t).

Table 12. Treatment comparison between mPharesis-drug treatments and 10 patients successfully treated with ET-drug therapies. mPharesis-drug treatments were constrained by Q,mP infuse=Q,max. The ratio of donor RBC volumes are compared between treatment types in **bold**.

		1	**2**	**3**	**4**	**5**	**6**	**7**	**8**	**9**	**10**
ET	**t (min)**	83	68	133	90	90	130	240	120	120	120
	Hct infuse	36%	46%	35%	42%	32%	23%	45%	32%	39%	30%
	Q, ET infuse (mL min^{-1})	65	37	18	17	26	52	8	30	37	45
	Donor packed RBC Vol (mL)	2999	1769	1124	1223	1132	2388	1246	1772	2640	2492
mPharesis Q,mP infuse = Q,max	**t (min)**	41	34	65	167	40	44	61	48	46	34
	Hct infuse	49%	50%	44%	50%	50%	33%	48%	37%	48%	46%
	Q,mP infuse (mL min^{-1})	500	500	160	270	280	480	230	420	420	55
	Donor packed RBC Vol (mL)	1545	1438	704	3815	862	976	1025	1132	1427	1203
	t mP:ET	**0.5**	**0.5**	**0.5**	**1.9**	**0.4**	**0.3**	**0.3**	**0.4**	**0.4**	**0.5**
	Donor Vol mP:ET	**0.5**	**0.8**	**0.6**	**3.9**	**0.8**	**0.4**	**0.8**	**0.6**	**0.5**	**0.5**

When flow rate is maximized to typical CRRT rates, treatment times and needed donor blood volumes were reduced for 9 out of 10 cases. Calculated treatment times for mPharesis were all less than 60% of the reported ET treatments, with times ranging from 28 to 65 minutes, and far less than conventional 3 hour dialysis treatment sessions. Shorter times mean decreased likelihoods for treatment-related complications such as hemorrhaging, thrombosis, or flu-like symptoms. The flow-maximized mPharesis-drug treatments used between 18% to 59% less donor blood than the reported ET-drug treatments. Also, between 704 and 1545 mL of packed donor RBCs (3 to 6 units of whole blood) were calculated to be needed which is less than average ET volumes[2]. Less donor blood was needed when flow rate was maximized (i.e. decreases treatment time) and, as expected, when the patients were small, had a lower initial parasitemia, or higher initial Hct. One case (#4) required much greater donor blood volumes (almost 4 times) and a treatment time twice as long as the reported ET. This was likely due to the patient's unique combination of severe hyperparasitemia (75%) and anemia (21% Hct) which required huge amounts of blood to be replaced rapidly to be successfully treated. However, the magnetic apheresis treatment was nevertheless successful at improving the patient's condition; the final Para value reported for ET (18%) was reached within a

third of the time of ET with 30% less donor blood with no loss of Hct. With an improved HGMS device performance, such as a paramagnetic RBC removal efficiency of 40%, the donor blood needed is 49% less than ET and treatment time is further reduced to 60% of the reported ET time. Even at significantly less than 100% paramagnetic RBC removal efficiency, this continuous HGMS system could provide a useful clinical alternative where time and donor blood is scarce.

4.3.4 Treatment Reference Charts

Two reference tables (Table 13 and Table 14) were generated to quickly reference approximate treatment times and the packed donor RBC volume needed for a treatment scale mPharesis-drug therapy. The two tables examined treatments with target final patient parameters $Para_f$<5%, Hct_f>30% and $Para_f$<1%, Hct_f>40%. A standard, extensive, or custom treatment may be chosen based on a clinician's previous experiences as each patient responds differently to various disease statuses and treatments. A_{drug} was constrained to 1.0%, the most conservative value found during the 10 ET-drug case calibration. The charts were normalized for patient volume and PVR (packed volume ratio) is listed for each condition. The packed donor RBC volume needed for a treatment is equal to PVR*Q_{mP} (typically Vol,pt*0.1 min^{-1}).

Table 13. Standard mPharesis-drug treatment reference chart for time and donor blood volume. $Para_f$<5% and Hct_f>30%. Calculate the packed donor RBC volume needed for a treatment with PVR*Q_{mP}.

Standard $Para_f$<5% Hct_f>30%		**Hct,i**											
		15%		**20%**		**25%**		**30%**		**35%**		**40%**	
		t (min)	**PVR**	**t (min)**	**PVR**	**t (min)**	**PVR**	**t (min)**	**PVR**	**t (min)**	**PVR**	**t (min)**	**PVR**
Para,i	**10%**	38	3.8	28	2.8	16	1.6	13	9.0	18	5.0	21	0.0
	20%	41	4.1	31	3.1	25	2.3	29	2.1	33	1.8	36	1.6
	30%	44	4.4	36	3.6	34	3.1	37	3.0	41	2.9	44	2.8
	40%	48	4.8	42	4.2	40	3.8	44	3.9	48	4.0	50	3.9
	50%	52	5.2	49	4.9	46	4.6	48	4.7	52	4.8	54	5.0
	60%	57	5.7	58	5.8	60	6.0	62	6.2	65	6.5	70	7.0
	70%	63	6.3	68	6.8	75	7.5	85	8.5	100	10.0	124	12.4

Table 14. Extensive mPharesis-drug treatment reference chart for time and donor blood volume. $Para_f$<1% and Hct_f>40%. Calculate the packed donor RBC volume needed for a treatment with PVR*Q_{mP}..

Extensive $Para_f$<1% Hct_f>40%		Hct,i											
		15%		20%		25%		30%		35%		40%	
		t (min)	PVR	t (min)	PVR	t (min)	PVR	t (min)	PVR	t (min)	PVR	t (min)	PVR
Para,i	5%	72	7.2	62	6.2	51	5.1	38	3.8	30	2.7	40	2.9
	10%	74	7.4	66	6.6	55	5.5	42	4.2	45	3.9	58	4.5
	20%	80	8.0	74	7.4	66	6.6	56	5.6	60	5.5	75	6.4
	30%	87	8.7	83	8.3	79	7.9	73	7.3	69	6.8	85	8.2
	40%	94	9.4	94	9.4	95	9.5	95	9.5	96	9.6	97	9.7
	50%	102	10.2	107	10.7	114	11.4	123	12.3	136	13.6	159	15.9
	60%	111	11.1	122	12.2	137	13.7	159	15.9	200	20.0	317	31.7
	70%	121	12.1	139	13.9	166	16.6	216	21.6	400	40.0	-	-

To implement the HGMS treatment reference charts, a hypothetical case is applied: a teenage male arrives for treatment with Hct_i=22%, $Para_i$=27%, and Vol,pt≈4000 mL, showing symptoms of severe falciparum malaria in an endemic region. For a standard treatment, he receives IV drug therapy (e.g. artesunate-mefloquine) and mPharesis treatment at 400 mL min^{-1} (Vol,pt*BAR). Rounding up his disease parameters to 35% initial Hct and 30% initial parasitemia, to overestimate treatment times and volumes, Table 13 indicates a treatment time of 41 minutes with a PVR of 2.9. This leads to a treatment which removes approximately 1640 mL of the patient's blood (t*Q_{mP}*SR), replaced by about 1160 mL of packed donor RBCs (PVR*Q_{mP}) or about 4 whole blood units. An extensive treatment, using Table 14, leads to a 60 minute long treatment, PVR of 5.5, and approximately 2400 mL of the patient's blood removed and replaced by about 2200 mL of packed donor RBCs or about 8 whole blood units.

For extreme cases, such as adults with very high hyperparasitemia and low Hct (e.g. case #4), which the lower right corner of both reference tables with high treatment times and PVR values, ET may be the optimal option. ET can more rapidly replace circulating iRBCs and relieve severe anemia with a high ET flow rate rather than the smaller mPharesis infusion rate. Generally, ET treatments use 1 to 20 units of whole blood with an approximate treatment time of 2 hours. The approximated treatment times and donor

blood volume found from both reference charts are below typical ET values. These findings show a hypothetical treatment-scale mPharesis system could be a better treatment option for severely ill, anemic falciparum malaria infected patients.

4.3.5 Treatment-scale System Size Considerations

From idea to implementation, the creation of a medical device to sustain human life is a long and expensive process. Here, we simply examined the size feasibility of a treatment-scale mPharesis system with a maximum flow rate of 500 mL min^{-1}, the upper limit commonly used in CRRT. The hypothetical system linearly scales a single mesoscale prototype into wide, short parallel wire array layers. The system would not include any layering combinations in series because every additional layer in series would increase the waste drainage by 90% for a single system pass (e.g. 1-SR). This large increase in drainage flow would make the system nearly identical to ET while greatly reducing the system's selective iRBC clearance potential. The system would be stacked together tightly with precisely-designed, limited dead-volume, homogenous inflow system similar to artificial lung and renal devices. The flow rate could be driven by a roller pump powered by widely available car batteries in times of electricity blackouts.

The system would include almost 6500 mesoscale mPharesis units. 10 units would be combined into one wide, short piece stacked 10 units deep within a single layer (540 mm wide and 430 mm long). Each layer would be 3mm thick and lay adjacent to 13 mm thick magnet array, one layer on each magnet array face (i.e. two per array). 65 layers would be stacked within the system's internal blood-processing compartment leading to a 520 mm tall compartment (20 inches). This estimation is less than the size of three stacked briefcases. It was difficult to estimate the prime volume without knowledge of the treatment-scale flow network. Higher purity magnets, though more expensive, would reduce the system size. The system could also feature a scrolled design where a single, very wide array would be rolled around a barrel shaped magnet array. Each layer could share the same magnet array which would greatly reduce the size. However, designing a waste collection system in such a tight space would pose a

significant challenge. Ultimately, the continued development of a microfluidic HGMS blood filtration system for human use would be a considerable challenge beyond the current scope of this project.

4.4 Conclusions

The results from Specific Aim 1 motivated the design of a clearance model for iRBCs and patient Hct levels using a treatment-scale mPharesis system in comparison to reported ET case studies. The model used patient parameters estimated from routine clinical data. With a more extensive retrospective search and the collection of more detailed parasitemia data in the future, this basic model can easily be expanded upon. Clearance factors could be further detailed such as the complex interdependent iRBC infection characteristics, patient-specific responses to different drug combinations, the effects of variable ET infusion profiles, variability between different parasite strains, variations with a single individual over time, etc. While the calibrated models described here may not appropriately reflect actual treatment clearances, this provided a robust mathematical framework for further development into a useful prediction for treatment outcomes in ET and apheresis patients.

5 Perform a Parametric Study of Key Rheologic and Fluid Dynamic Factors Affecting the Efficiency of HGMS with Paramagnetic Red Blood Cells Using a Novel HGMS Device

5.1 Introduction

The efficiency of an HGMS device is highly dependent on its hemodynamic and geometric parameters. The ability to directly observe magnetophoretic separation in real-time was a continual objective during the development of the mesoscale mPharesis device in Specific Aim 1. Microscopic observation of the mPharesis flow field could elucidate the motion of metRBCs and hRBCs within the magnetophoretic flow field, allow for CFD model verification, and potentially aid in hemodynamic and geometric parameter optimization. However, due to the opacity limitations of the mesoscale device, direct microscopic observation was not possible. Many research groups have developed HGMS devices to selectively separate paramagnetic RBCs[23–25,73–81,88,108,122] and, to our knowledge, only three published continuous HGMS separators featured the ability to observe separation in real-time (shown in Figure 35).

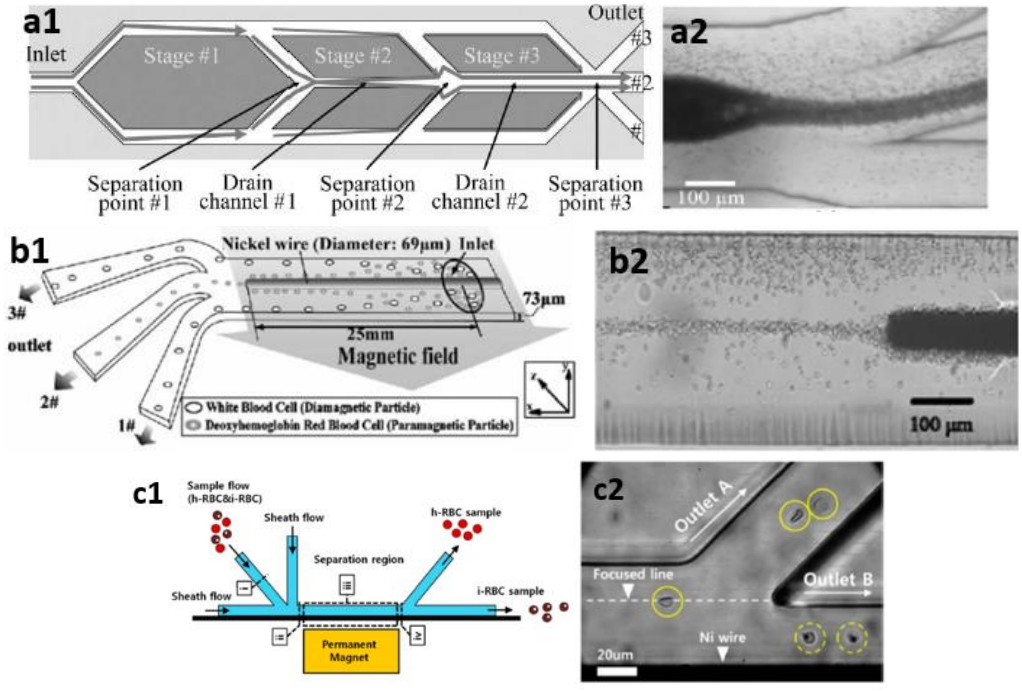

Figure 35. Three published continuous HGMS devices for paramagnetic RBC separation viewed via microscopy. a) Han et al. shows deoxyRBCs actively separated via a single stage separator featuring nickle plated islands. b) Qu et al.'s device separating deoxyRBCs using a stainless steel wire. c) Nam et al.'s device separating iRBCs with a nickel wire. All three use external PMs and dilute cell suspensions.

Han et al. created a multi-step cascade separator with specially shaped electroplated nickel islands to efficiently collect deoxyRBCs and white blood cells[86]. Qu et al. concentrated deoxyRBCs along the centerline of a microfluidic field and collected the cells in the center of three outlet paths[87]. Nam et al. designed a microfluidic separator with a nickel wire and a saline buffer layer parallel to the flow path edge to quickly clear captured target cells. This design enabled a high capture efficiency of early and late-stage iRBCs[65]. This design was referred to as an "H-filter" and has also been used by other research groups to capture magnetic particles attached to target cells for sepsis treatment[27]. Although highly efficient, H-filters encounter similar issues with hemodilution as HGMS batch separators. Microscopic visualization can be used to study the relation between cell motion, such as magnetophoretic mobility and cell sedimentation, and various rheological properties. Additionally, visualization can enable deliberate HGMS optimization while reducing needless trial-and-error prototyping.

Most reported continuous HGMS devices are made using standard PDMS soft-lithography fabrication methods. Inclusion of the secondary ferromagnetic element is often difficult as it must be in or directly adjacent to the flow field to be effective, as discussed in Specific Aim 1. Ultimately, fabrication of these devices with precisely aligned micron-scale metal elements are time consuming and involve sunstantial trial-and-error to assemble a successful device. Soft-lithography and micropatterning techniques are expensive, time consuming, and offer no flexibility for quick design changes.

A opportunity exists to a create an inexpensive, benchtop-fabricated continuous HGMS device that can be visualized microscopically and modified easily for rapid design optimization. This specific aim presents the design, fabrication, and microscopic visualization of such a device. This proof-of-concept device is then implemented to observe separation differences between various mixtures of metRBCs (heat-treated and un-heated) and transparent ghost RBCs (near zero hemoglobin) at several flow rates to test its utility. This work can be applied to rapidly improve and design mesoscale HGMS devices, such as mPharesis, to enable rapid innovation in the magnetic bio-separation field.

5.2 Materials and Methods

5.2.1 Device Fabrication

The same ferromagnetic photoetched array from Specific Aim 1 was used in this specific aim. The gaps in the photoetched wire array were filled with Smooth-Cast 300 two part fast-setting resin (Smooth-On Inc., Macungie, PA, USA). During the curing process, the resin-array was sandwiched between two 6 mm pieces of acrylic primed with mold release and clamped with four large binder clips. The filled wire array was then trimmed within approximately 1 mm of the wire array pockets edge using a benchtop mini shear. The top and bottom plate were laser cut with a laser cutter (Zing, Epilog) from 3 mm cast acrylic sheet. Silicone gaskets, used to seal the device, were laser cut from 125 µm thick gloss silicone sheets (BioPlexus Corporation, Venture, CA, USA). This silicone brand, thickness, and finish was chosen for its high purity and optical transparency. The flow shim was cut from 125 µm thick polyethylene shim stock using a CNC cutting machine (Cameo, Silhouette). Soft silicone tubing (0.8 mm ID) was glued into inlet ports using Loctite 420 cyanoacrylate. The assembly was clamped together with 4-40 socket head screws and nuts, tightened gently by hand. The final device is shown in Figure 36.

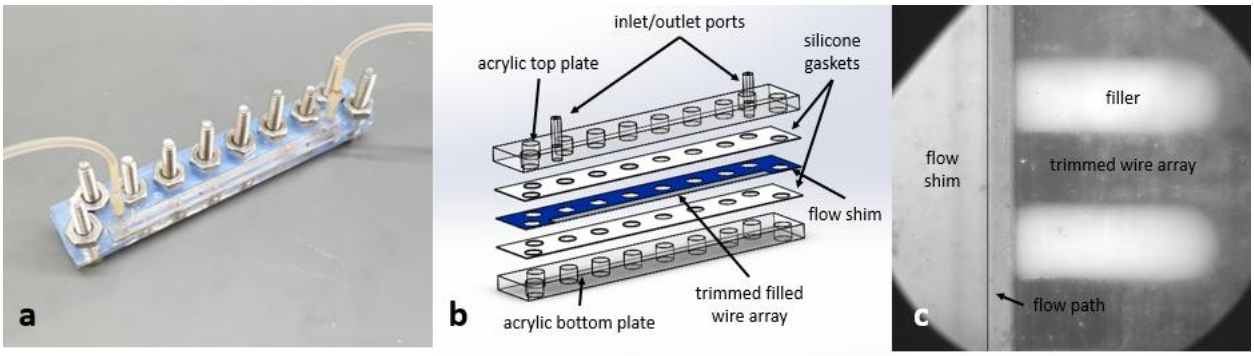

Figure 36. a) Benchtop-fabricated continuous HGMS device for microscopy visualization. b) Exploded CAD model of design. c) Double bright field (below and above) view of device at 200x.

5.2.2 Experiment Parameters and Setup

Preparation of metRBCs was described in Specific Aim 1. Transparent ghost RBCs, used to maintain opacity in the microfluidic flow field at physiological RBC concentrations, were created using the protocol created by Jamiolkowski et al.[123] Table 15 lists the test parameters for the 36 videos were

recorded: 3 different RBC mixtures at 3 different flow rates, without and with a magnet, and with an inlet and outlet observation for each. Viscosity versus shear rate curves were obtained for each sample using a Brookfield Viscometer (Brookfield AMETEK, Middleboro, MA, USA).

Table 15. Test conditions for benchtop HGMS microscopy studies.

#	metRBC Hct	ghost RBC Hct	Q (µL min^{-1})	heat-treat metRBCs 1hr @ 48C
1	0.5%	0%	0.4	No
2	0.5%	0%	0.6	No
3	0.5%	0%	0.8	No
4	0.5%	30%	0.4	No
5	0.5%	30%	0.6	No
6	0.5%	30%	0.8	No
7	0.5%	30%	0.4	Yes
8	0.5%	30%	0.6	Yes
9	0.5%	30%	0.8	Yes

The experiment setup is pictured in Figure 37. Flow was pulled through the device using a Harvard Apparatus PhD Ultra syringe pump with a 0.1 mL glass syringe. Flow was visualized with a high-speed camera (Fastcam SA4, Photron, San Diego, CA) attached to an inverted microscope (Olympus IX-70) with bright-field microscopy at 200x. The flow and magnetic separation were allowed to reach steady state to before filming. 750 frames were captured per video at a constant of about 32 frames per µL min^{-1} to ensure the same RBC did not overlapped itself between two adjacent frames. The inlet and outlet videos for each condition were filmed within 60 seconds of each other to ensure reasonable comparison.

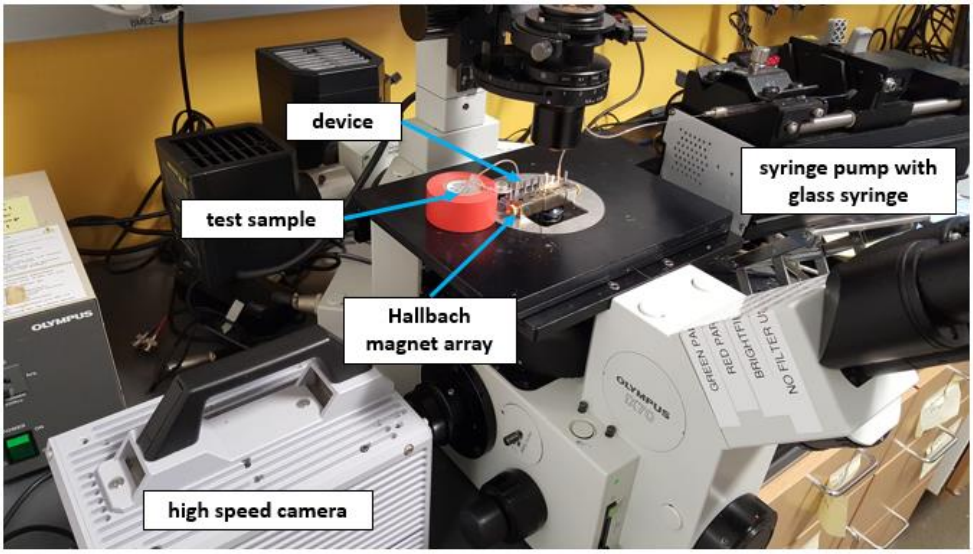

Figure 37. Experiment setup for benchtop HGMS microscopy studies.

5.2.3 Video Analysis and Cell Counting

An automated RBC counting method is described here. Videos were first processed with the "Find edges" feature in ImageJ (National Institutes of Health, Bethesda, MD, USA) and then contrast was increased to maximum. Next, a transverse line of fixed-width was drawn across the flow path and was applied to the entire video (using the "Draw" feature, Figure 38). This was repeated for two other transverse lines (n=3 per video). These "lines of interest" were used to count passing cells and were placed at a location where no cell or non-cellular particulate became stuck during the video.

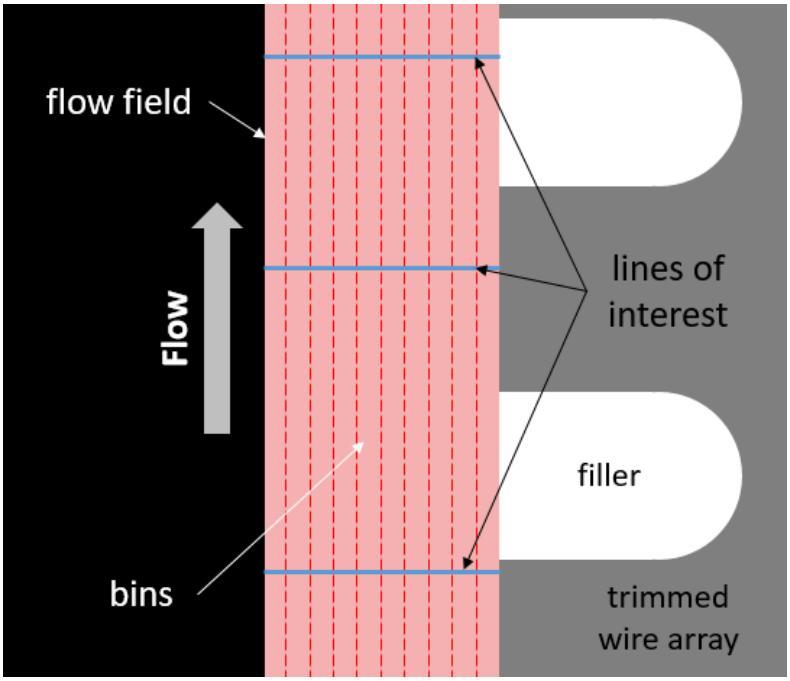

Figure 38. Diagram of microscopy flow field used for cell counting algorithm. Lines of interest are indicated with blue lines. Bins, used to partition cell counts into concentration profile plots, are indicated with red dashed lines (not to scale).

A macro named "Stack Profile Data" (see Appendix C) was applied to plot the intensity across lines of interest for each frame then concatenated into a single 2D matrix (Figure 39). The matrix was processed in Matlab, simplifying each cell into one point while recognizing various "inner tube" RBC shapes as one cell (see Appendix D). Cells were 3 to 8 pixels wide. 1 and 2 pixel wide noise was removed. The simplified data was then summed across ten bins for all frames. Final bin sums were compared inlet to outlet. The differences between inlet and outlet was added to the bin adjacent to the trimmed wire array to account for "invisible" cells unseen in the high packing densities from magnetic separation. This automated cell count was compared with manual counting (using the Manual Tracking feature in ImageJ) for one line of interest in three arbitrary videos.

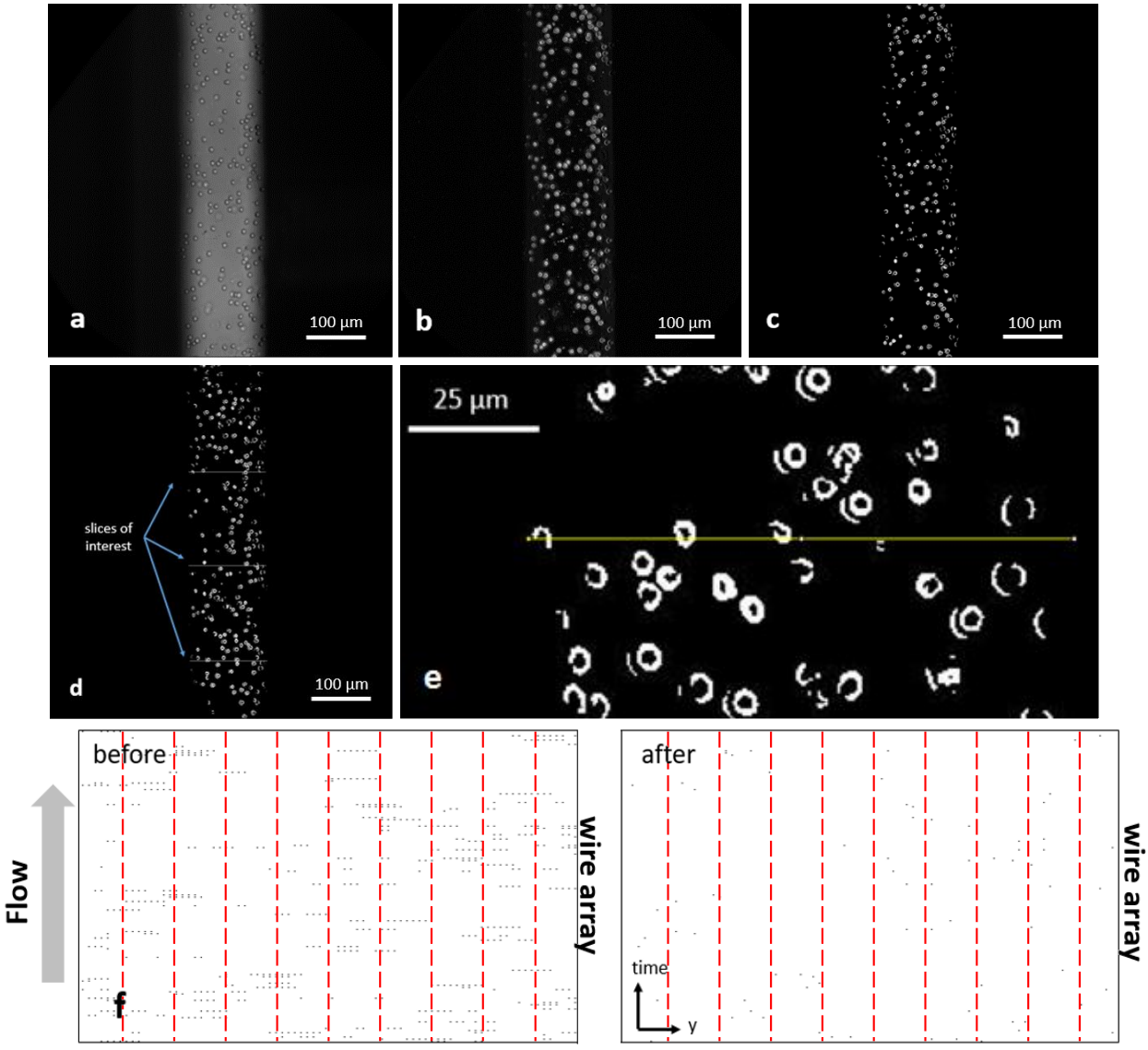

Figure 39. Image processing procedure using ImageJ. a) Original. b) "Find edge" applied. c) Adjusted to maximum contrast. d) Three "lines of interest" are chosen to obtain intensity profiles across for the whole video. e) Close-up of d. f) Before and after intensity data processing to simplify to single cells in Microsoft Excel with binning (red dashed lines).

Each binned count was normalized so the sum of all bins equaled 1. The normalized cell concentration profile, the bar graph of cell counts for 10 bins, for each condition was plotted. The degree of separation (DOS) was measured by the ratio of the averages of the cell count of the bin adjacent to the wire array versus the remaining 9 bins (Equation 43).

$$\mathrm{DOS} = \frac{\text{average cell count of bin adjacent to wire array}}{\text{average cell count of remaining bins}} \qquad [43]$$

DOS was compared in four ways: inlet and outlet for the same videos, no magnet and magnet for the same condition, flow rates for the same RBC conditions, and different RBC mixtures for the same flow rates.

5.3 Results and Discussion

Fabrication of this device required approximately 6 hours of manual labor by a person with moderate manual skill and minimal practice. In this time, the wire array was trimmed, the various component layers were cut, glue the inlet tubing, and everything was assembled followed by an overnight cure of the resin. The device could be quickly taken apart to clean or modify the flow path width or angle. Cost was minimal; off-the-shelf stock materials and supplies were used in addition to the custom trimmed photoetched wire array ($2 per array). The voids between the wires were filled for two reasons: metRBCs would collect in the voids and thus could not be collected later on. Also, some metRBCs, previously concentrated on wire array surface, would enter and exit the inter-wire void rapidly undoing the useful separation of the device (shown in Figure 40). These reasons were similar in Specific Aim 1 where the voids where also filled.

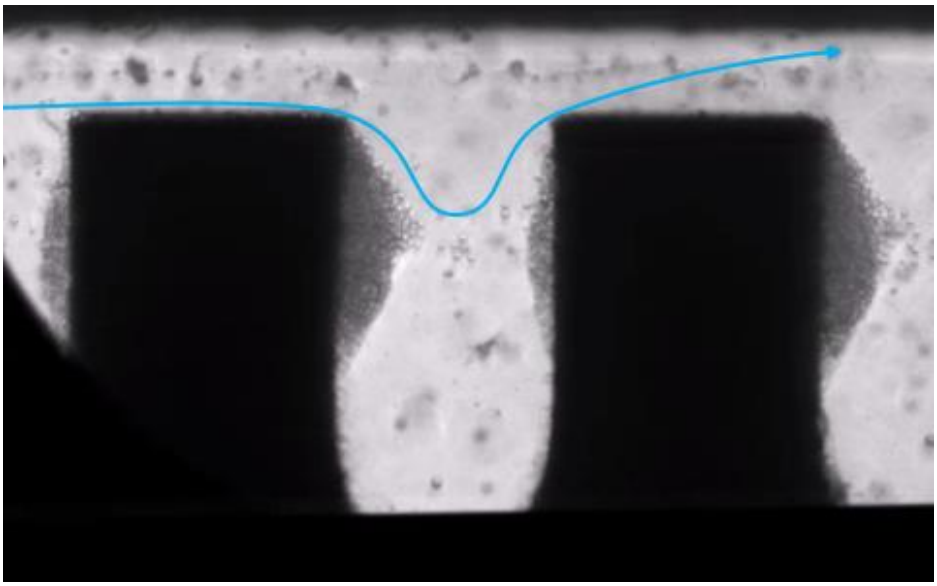

Figure 40. View of trimmed wire array with 0.5% metRBCs collection in inter-wire voids. Blue line indicates path of separated free-flowing metRBC becoming un-captured by inertial force while exiting the void.

5.3.1 Viscosity vs. Shear Rate Plot

Viscosity versus shear rate graphs for every test condition are shown in Figure 41. Readings where torque was below 10% were omitted due likelihood of large viscosity reading errors. Measurements were taken between 23.1 and 25.7 °C depending on room temperature. Device experiments in this aim were performed at approximately 20 to 60 s^{-1}, but the viscometer used was unable to obtain reliable measurements (i.e. greater than 10% torque) in that range. Thus, results were compared at higher shear rates. 0.5% metRBC was chosen because it was the limit of opacity in this microfluidic device. 30% total Hct was chosen as a similar condition average reported values for severe infected malaria patients[21,55,103–107]. Values for 28% Hct whole blood from Wells et al. were included as benchmark for non-diluted whole blood[124].

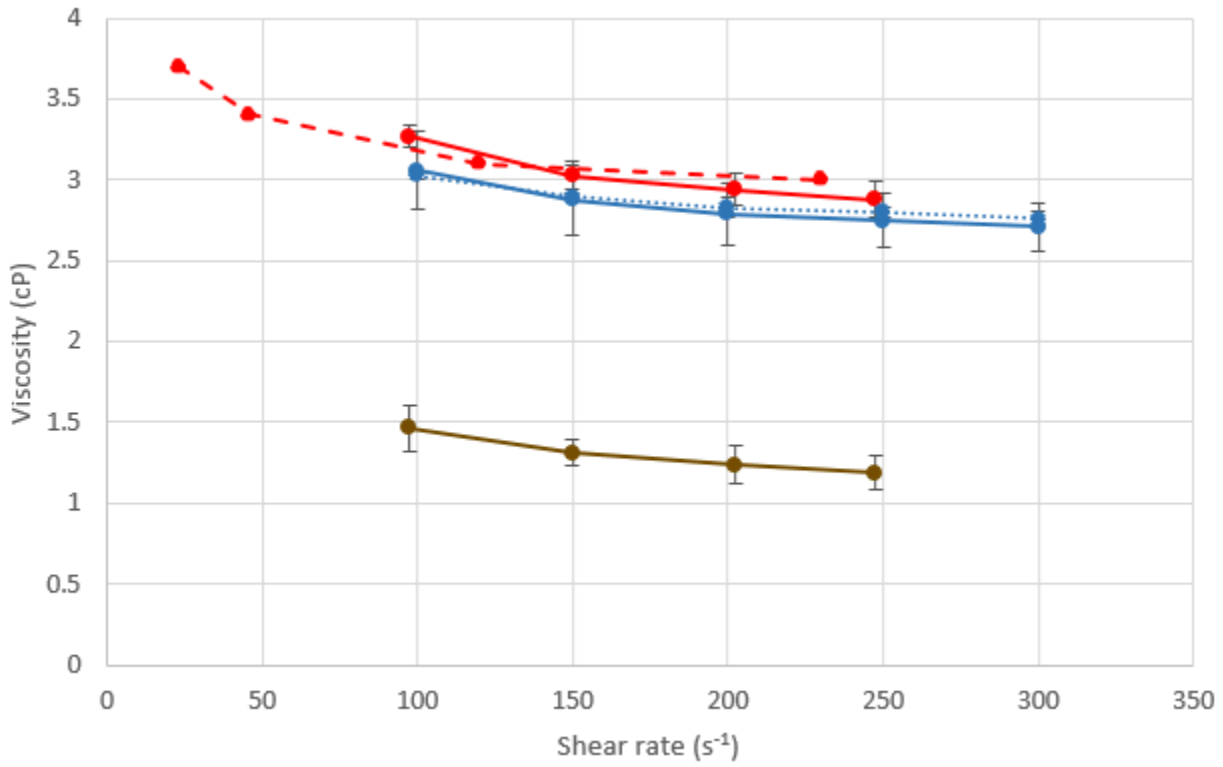

Figure 41. Viscosity vs. shear rate graphs for 30% Hct diluted whole blood (red solid), 28% Hct whole blood (red dash)[124], 0.5% Hct metRBCs (brown), 0.5% metRBCs + 30% ghost RBCs (blue solid), and 0.5% heat treated (60 min) metRBCs + 30% ghost RBCs (blue dots).

Results were predictable: the 0.5% metRBC suspension was significantly less viscous than the whole blood and metRBC-ghost RBC suspensions. Although hardened RBCs are known to increase suspension viscosities[125,126], there was very little difference between the un-heated and heat-treated metRBCs at such a low concentration. The 30% ghost RBC and metRBC suspensions were within approximately 0.2 cP (within 6%) of the diluted whole blood samples at room temperature, likely measurement error and/or the difference in RBC donors and the older age of the ghosts. This was suspected because ghost RBCs are reported to have very similar shear rate curves as native RBCs[123].

5.3.2 Image Analysis Results

Table 16 shows the image processing procedure using ImageJ and Matlab. The results of comparing manual counts to the automated algorithm from three randomly chosen videos are in Table 16. When manually counting, only foreground cells with clearly defined borders were counted. Out-of-focus background metRBCs were easily mistaken for ghost RBCs even when the ghost cells were in the foreground. The automated method appeared, qualitatively, to recognize and count foreground cells with decent accuracy. The difference between the two was likely due to the edges of the channel causing foreground cells to appear blurry and be filtered out by the image processing algorithm. Likewise, both with manual and automated counting, it was not possible to get an accurate count of the number of cells rolling along the face of the trimmed wire array. Thus, comparison between inlet and outlet was needed to estimate that number and likely contributes to counting errors.

Table 16. Comparison for cell counts between manual and automated methods (n=3).

	Video 1	Video 2	Video 3
Manual total	852	940	349
Automated total	782	879	319
Difference (diff/manual)	70 (8.2%)	61 (6.5%)	30 (7.5%)

5.3.3 Cell Concentration Profiles

The automated counting algorithm underestimated actual counts and thus needs further improvement, but nevertheless facilitated rapid analysis of the 48 microscopy videos taken at three transverse lines. The total channel height was approximately 150 μm at the inlet and 130 μm wide at the outlet with a thickness (z-direction) of 125 μm. Figure 42 shows the normalized cell concentration plots comparing inlet and outlet with no magnet (control) to magnet condition at the outlets, one plot for each RBC mixture type. Figure 43 compares the outlets across all conditions with a magnet.

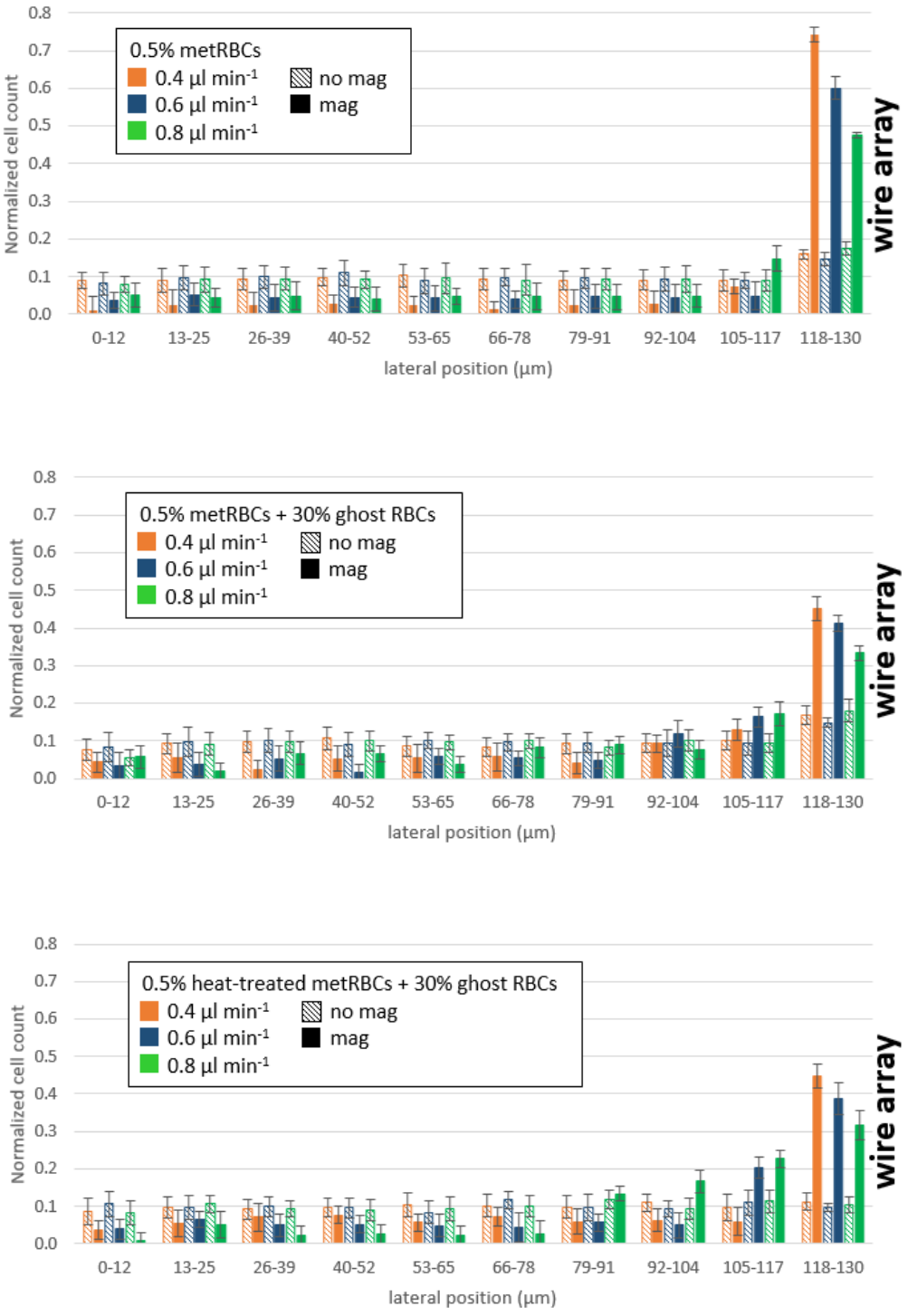

Figure 42. Cell concentration profiles across HGMS device for four blood mixtures conditions: 0.5% metRBCs, 0.5% metRBCs and 30% ghost RBCs, and 0.5% heat-treated (60 min) metRBCs and 30% ghost RBCs. Each plot compares metRBC separation at three flow rates: 0.4, 0.6 and 0.8 µL min^{-1}; no magnet (dashed) versus magnet (solid). Cell counts were summed across 10 bins across all video frames.

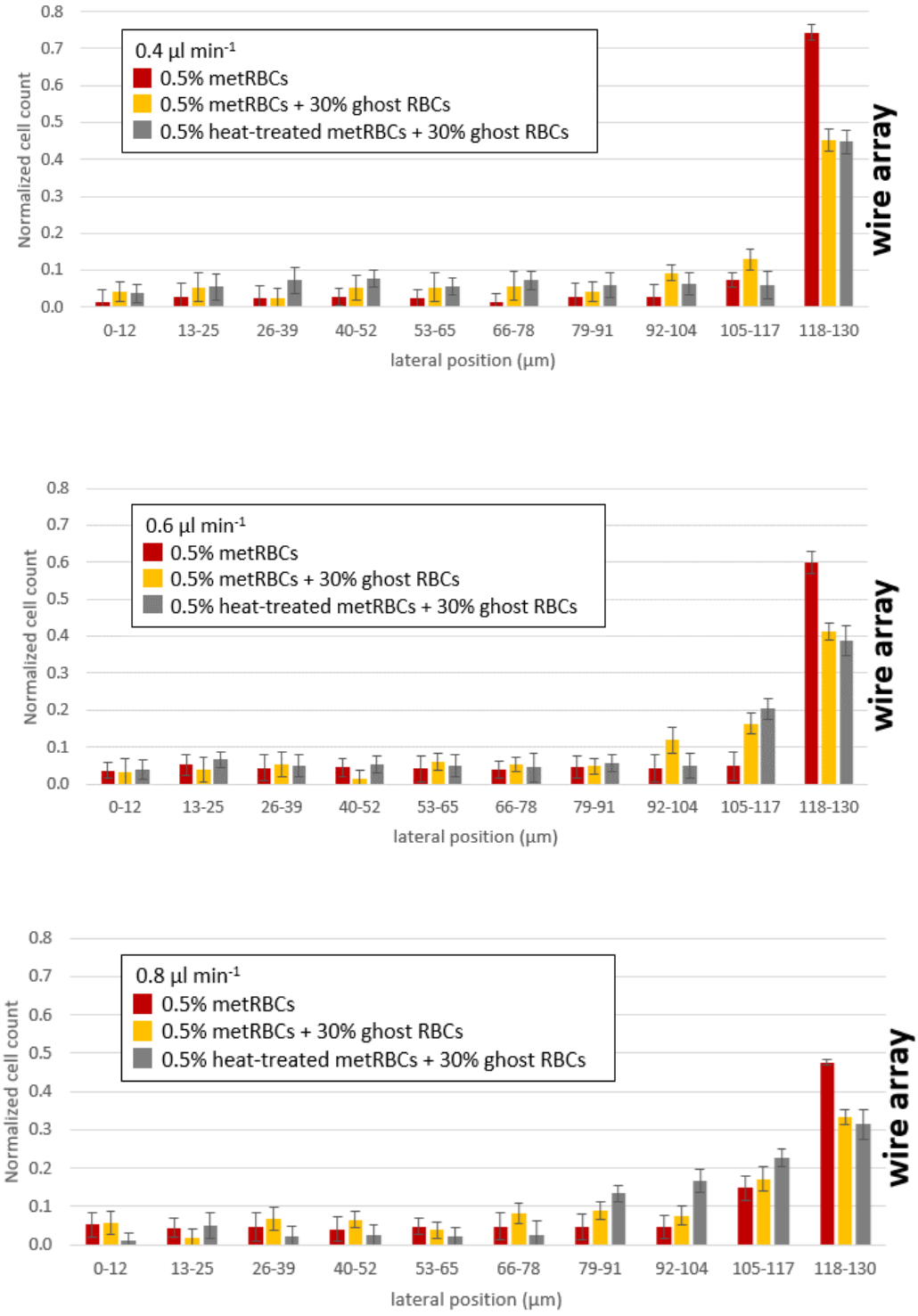

Figure 43. Cell concentration profiles across HGMS device for three flow conditions: 0.4, 0.6 and 0.8 µL min^{-1}. Each plot compares four blood suspension mixtures: 0.5% metRBCs, 0.5% metRBCs and 30% ghost RBCs, and 0.5% heat-treated (60 min) metRBCs and 30% ghost RBCs; with a magnet applied. Cell counts were summed across 10 bins across all video frames.

To compare the cell concentration profiles quantitatively, degree of separation (DOS, ratio of averages of the bin adjacent to the wire vs the remaining bins) values were compared. Table 17 lists the DOS values for all conditions, no magnet and magnet at the inlet and outlet. DOS=0 if no cells were present in the bin adjacent to the wire array. DOS=1 if the cell concentration profile was homogenous across the channel, not considering the cell-free 2 to 4 μm wide half-RBC regions at either edge. DOS→∞ when all cells concentrated in the bin adjacent to the wire array.

Table 17. Degree of separation (DOS) for HGMS microseparator experiments with three RBC mixtures in saline (0.5% metRBCs, 0.5% metRBCs + 30% ghost RBCs, and 0.5% heat-treated metRBCs + 30% ghost RBCs) for 3 flow rates (n=3).

	INLET		**OUTLET**	
#	**DOS no magnet**	**DOS magnet**	**DOS no magnet**	**DOS magnet**
1 0.5% met 0.4 μL min^{-1}	1.1 ± 0.2	2.0 ± 0.5	2.4 ± 0.4	26 ± 2.7
2 0.5% met 0.6 μL min^{-1}	1.0 ± 0.3	1.9 ± 0.6	2.0 ± 0.6	14 ± 3.0
3 0.5% met 0.8 μL min^{-1}	1.0 ± 0.3	1.1 ± 0.5	1.8 ± 0.6	8.2 ± 1.8
4 0.5% met + 30% ghost 0.4 μL min^{-1}	1.2 ± 0.2	1.6 ± 0.8	2.0 ± 0.5	7.4 ± 2.0
5 0.5% met + 30% ghost 0.6 μL min^{-1}	1.1 ± 0.1	1.4 ± 0.7	1.8 ± 0.4	6.3 ± 1.8
6 0.5% met + 30% ghost 0.8 μL min^{-1}	0.95 ± 0.3	1.2 ± 0.8	1.3 ± 0.8	4.5 ± 1.5
7 0.5% heat-met + 30% ghost 0.4 μL min^{-1}	1.0 ± 0.3	1.5 ± 0.6	1.5 ± 0.6	7.3 ± 2.0
8 0.5% heat-met + 30% ghost 0.6 μL min^{-1}	1.0 ± 0.1	1.3 ± 0.7	1.6 ± 0.4	5.7 ± 1.5
9 0.5% heat-met + 30% ghost 0.8 μL min^{-1}	1.0 ± 0.2	1.1 ± 0.8	1.4 ± 0.5	4.1 ± 1.4

The average DOS values for the inlet no magnet conditions ranged from 0.9 to 1.2. The inlet flow was developed by the filming location 5 mm into the separation area (Re=0.01 to 0.03, $L_{entrance}$=0.2 mm). These DOS values are close to the expected value of 1 as expected for a homogenous cell concentration profile with no magnetophoretic force present. The average inlet DOS value for the magnet conditions ranged from 1.0 to 2.0, higher than the inlet no magnet values because some magnetophoretic separation occurs in the 5 mm length before the filming location. The average DOS values for the magnet condition

was slightly higher for the low flow rates and without ghost RBC conditions where paramagnetic RBCs could most easily separate with increased Hct. There was not a significant difference with the addition of a heat-treatment step for the metRBCs. The average DOS values for outlet no magnet conditions ranged from 1.3 to 2.9. Those values are likely non-zero, again, due to magnetic remanence left in the trimmed wire array causing some separation. The average DOS values for the outlet magnet conditions ranged from 4.1 to 26.0. The effect of flow rate, Hct, and heat-treatment on DOS was similar as explained for the magnet inlet conditions for both magnet and no magnet conditions at the outlet.

The greatest separation occurred for 0.4 μL min^{-1} flow rate for all three RBC suspension mixtures. This flow rate had a similar average flow velocity as the mPharesis device described in Specific Aim 1 (0.3 vs 0.4 mm s^{-1} here). Below 0.4 μL min^{-1}, the metRBCs would visibly sediment, thus that flow rate was not included in this study. As expected, the best separation occurred for the 0.5% metRBCs suspension for all three flow rates. Without ghost RBCs, Hct was very low, enabling fast metRBC separation to the wire array surface and minimized remixing from cell-cell interactions. Separation was not 100% efficient, likely due to some disruptive cell-cell interactions occurring and the channel height (H=130 μm) exceeding the maximum capture reach of the magnet. This maximum capture width was previously found to be about 50 to 70 μm in Specific Aim 1. The addition of 30% ghost RBCs decreased the separation somewhat, but not as to the degree that was expected. Although disruptive cell-cell interactions are guaranteed with the addition of ghost RBCs, the same interactions were likely beneficial by nudging distal cells into the magnetic force capture reach. The separation efficiency between heat-treated and non-heated cells was not significant. Fully stiffened metRBCs have been shown to increase the viscosity of their solutions and aggregate differently than hRBCs[125,126], which would affect separation, but these properties are not exhibited in low concentration RBC suspensions. Figure 44 shows a two select still frames from the microscopy videos.

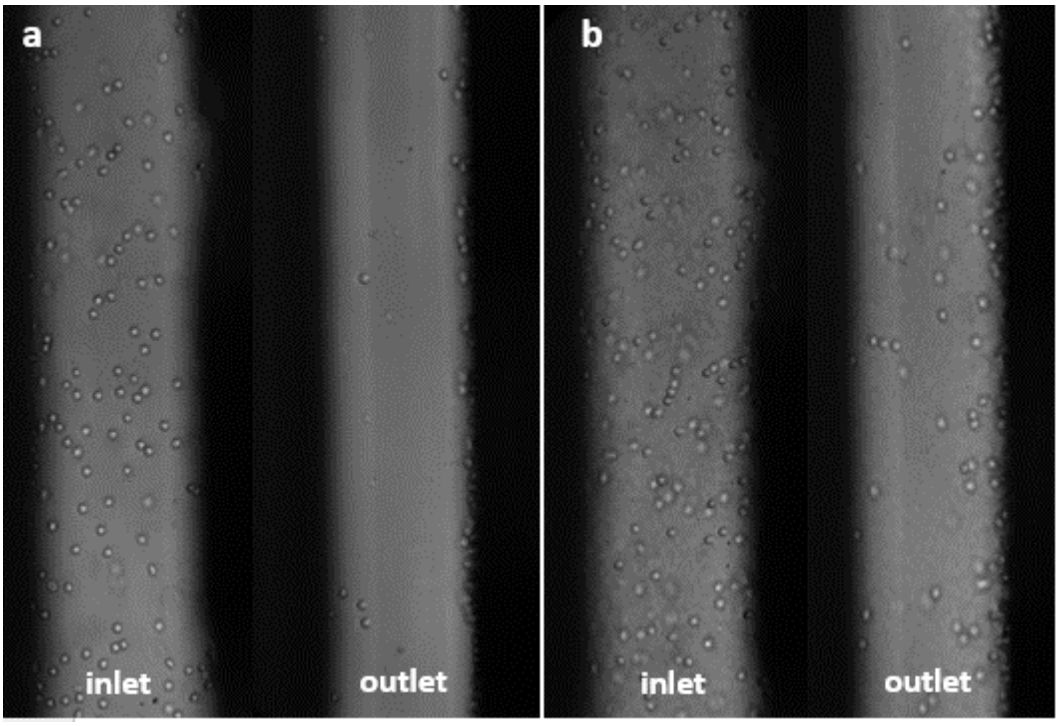

Figure 44. Three still frame sets from the continuous HGMS microscopy videos: a) 0.5% metRBC and b) 0.5% metRBCs + ghost RBCs; each with the magnet present at 0.4 μL min^{-1}.

5.4 Conclusions

The primary objective of this Specific Aim was the creation of a continuous HGMS device for microscopic visualization. Proof-of-concept experiments successfully proved this novel device's utility to directly observe magnetophoretic separation in real time while varying rheological and hemodynamic parameters, such as Hct and flow rate. This device and simple fabrication protocol can be a very useful tool for bioseparator optimization and research. These modifications can then be applied to a larger device such as the mPharesis mesoscale separator featured in Specific Aim 1. The automated RBC counting method described here enabled quick analysis and provided reasonable results. Future microscopy studies are recommended to better understand the relationship between various rheological and hemodynamic parameters, especially the interaction forces between metRBCs and hRBCs at physiological concentrations.

6 SUMMARY

Almost half a million deaths are caused annually by falciparum malaria. Despite being a centuries old epidemic, malaria has yet to be eradicated. Drug-resistant malaria strains have begun spreading throughout sub-Saharan Africa and southeast Asia, thus new treatments options must be developed. While ET methods are sometimes effective to save severely ill patients from the brink of death, no treatment option exists to filter out the infected red blood cells from a patient's circulation while saving precious donor blood. This thesis described the creation of a continuous high gradient magnetophoretic separation device to selectively remove iRBCs from blood at physiological concentrations.

The first aim of this thesis involved the creation of mPharesis, a mesoscale microfluidic continuous HGMS device, which capitalizes on iRBC's unique paramagnetic property. A mesoscale prototype device was designed, computationally optimized, and fabricated. The device was verified, successfully removing a fraction of paramagnetic RBCs in one pass without excessive loss of healthy cells. The second aim involved describing a novel parasite clearance and Hct model to compare the prototype results with published ET case studies. The model predicted mPharesis would be a viable, effective option in most cases compared to ET and drug-resistant patients. The third aim involved the design of an inexpensive, benchtop-fabricated HGMS device for microscopic visualization. Parametric studies were performed with various RBC types and conditions then processed with a custom cell counting algorithm. Resulting videos and cell concentration profiles were predictable yet motivating. This aim lays significant groundwork for future HGMS visualization and optimization studies.

While mPharesis may currently be beyond the scope of a clinically implemented treatment system, the work in this thesis established an innovative method for HGMS design and scaling that has great potential for further growth and other applications.

7 LIMITATIONS

The present study involved several assumptions and trade-offs in both experiments and mathematical models. Listed below are study limitations.

Limitations in magnetic force design

1. Magnetic force was described using perfectly square, pure neodymium magnets with 90 degree corners, likely amplifying the gradient force magnitude for the entire flow field. More accurate, detailed magnetic modeling is needed.
2. The magnetic field was only modeled in 2D, neglecting variations in transverse forces across the mPharesis device and edge effects. This lacking was limited by implementing a magnet array 27% wider than the flow field.

Limitations in experiments

1. Experiments were performed using washed human RBC suspensions as a substitute for whole blood to in order to prevent clotting during proof-of-concept experiments. The lack of serum proteins and other significant rheological factors present in whole blood likely affected the results of the mesoscale device and continuous HGMS microscopy experiments. RBC suspensions do not exhibit aggregation, which affects low-shear viscosities that the experimental conditions described in this thesis operate.
2. Malaria-infected RBC cultures were not used due to difficulty of culture management and lack of access to experienced malaria-culturing lab resources. iRBCs have time dependent magnetic susceptibility and cell wall properties, not reflected in the metRBC analog.
3. For the HGMS microscopy studies, only foreground cells were counted as they were the only layer that could be effectively focused upon. These cells were the cells rolling along the bottom of the microfluidic channel and likely did not represent the flow or separation characteristics of the bulk fluid.

Limitations of clearance model

1. MetRBC removal results from Specific Aim 1, obtained from the results of one experimental condition (n=11), were directly applied without modification to Specific Aim 2. This parameter would change with different initial patient conditions, such as parasitemia and Hct, and further studies are needed to solve this variability.
2. While case reports with many of the necessary patient parameters were specifically selected, several parameters were estimated including patient volume (8 out of 10 cases), infusion Hct (9 out of 10), ET drain volume (3 out of 10), and parasite clearance efficiency via drugs and innate factors (10 out of 10). Patient blood volume and ET drain volume were not modified after an initial estimate. These assumed and calibrated parameters enabled coercing of the model to fit reported ET results before proceeding. Future prospective studies, where specific parameters could be collected, would alleviate this issue.
3. Parasite clearance via drug and drainage factors and Hct increases from donor blood were modeled as simple first order rate equations. This assumption likely vastly oversimplifies the actual dynamics of the variables.
4. The clearance model accounts for "other variables" like drug-resistance, co-infections, and native immunity with a single factor (A_{drug}). A_{drug} was proven to be overestimated in this thesis as compared to reported values[113]. Further research and clinical data is needed to part out A_{drug} into more variables and avoid generalized "calibration" terms.

REFERENCES

1. *World Malaria Report*.; 2015.

2. Phillips P, Nantel S, Benny W. Exchange transfusion as an adjunct to the treatment of severe falciparum malaria. *Rev Infect Dis*. 1990;12(6):1100-1108. http://www.ncbi.nlm.nih.gov/pubmed/1623091.

3. Dondorp AM, Kager PA, Vreeken J, White NJ. Abnormal blood flow and red blood cell deformability in severe malaria. *Parasitol Today*. 2000;16(6):228-232. http://www.ncbi.nlm.nih.gov/pubmed/10827427.

4. Dondorp AM, Pongponratn E, White NJ. Reduced microcirculatory flow in severe falciparum malaria: Pathophysiology and electron-microscopic pathology. *Acta Trop*. 2004;89(3):309-317.

5. MacPherson GG, Warrell MJ, White NJ, Looareesuwan S, Warrell DA. A Quantitative Ultrastructural analysis of Parasitized Erythrocyte Sequestration. *AJP*. 1985;119(3):385-401.

6. Ponsford MJ, Medana IM, Prapansilp P, et al. Sequestration and microvascular congestion are associated with coma in human cerebral malaria. *J Infect Dis*. 2011;205(4):663-671. doi:10.1093/infdis/jir812.

7. Shelby JP, White J, Ganesan K, Rathod PK, Chiu DT. A microfluidic model for single-cell capillary obstruction by Plasmodium falciparum-infected erythrocytes. *Proc Natl Acad Sci U S A*. 2003;100(25):14618-14622. doi:10.1073/pnas.2433968100.

8. Cranston H, Boylan C, Carroll G, et al. Plasmodium falciparum maturation abolishes physiologic red cell deformability. *Science*. 1984;223(4634):400-403. http://www.ncbi.nlm.nih.gov/pubmed/6362007.

9. Lee WG, Kim Y-G, Chung BG, Demirci U, Khademhosseini A. Nano/Microfluidics for diagnosis of infectious diseases in developing countries. *Adv Drug Deliv Rev*. 2010;62(4-5):449-457. doi:10.1016/j.addr.2009.11.016.

10. Trampuz A, Jereb M, Muzlovic I, Prabhu RM. Clinical review: Severe malaria. *Crit Care*. 2003;7(4):315-323. doi:10.1186/cc2183.

11. Dondorp AM, Nosten F, Yi P, et al. Artemisinin Resistance in Plasmodium falciparum Malaria. *N Engl J Med*. 2012;361(5):455-467.

12. Ashley EA, Dhorda M, Fairhurst RM, et al. Spread of Artemisinin Resistance in Plasmodium falciparum Malaria. *N Engl J Med*. 2014;371(5):411-423. http://www.nejm.org/doi/abs/10.1056/NEJMoa1314981.

13. Nieuwenhuis JA, Meertens JHJM, Zijlstra JG, Ligtenberg JJM, Tulleken JE, van der Werf TS. Automated erythrocytapheresis in severe falciparum malaria: A critical appraisal. *Acta Trop*. 2006;98(3):201-206. doi:10.1016/j.actatropica.2006.05.003.

14. Kreeftmeijer-Vegter AR, Melo MDM, de Vries PJ, Koelewijn R, van Hellemond JJ, van Genderen PJJ. Manual blood exchange transfusion does not significantly contribute to parasite clearance in artesunate-treated individuals with imported severe Plasmodium falciparum malaria. *Malar J*. 2013;12:115. doi:10.1186/1475-2875-12-115.

15. Pasvol G. The treatment of complicated and severe malaria. *Br Med Bull*. 2005;75-76(1):29-47. doi:10.1093/bmb/ldh059.

16. Omari A, Garner P. Malaria : severe , life-threatening Search date December 2009 Infectious diseases Malaria : severe , life-threatening. *Clin Evid (Online)*. 2007;913(December 2007).

17. Shelat SG, Lott JP, Braga MS. Considerations on the use of adjunct red blood cell exchange transfusion in the treatment of severe Plasmodium falciparum malaria. *Transfusion*. 2010;50(4):875-880. doi:10.1111/j.1537-2995.2009.02530.x.

18. Vachon F, Wolff M, Clair B, Regnier B. Letter to the Editor: Treatment of Severe Malaria by Exchange Transfusion. *N Engl J Med*. 1990;322(1):58-59.

19. van Genderen PJJ, Hesselink D a, Bezemer JM, Wismans PJ, Overbosch D. Efficacy and safety of exchange transfusion as an adjunct therapy for severe Plasmodium falciparum malaria in nonimmune travelers: a 10-year single-center experience with a standardized treatment protocol. *Transfusion*. 2010;50(4):787-794. doi:10.1111/j.1537-2995.2009.02488.x.

20. White NJ. What is the future of exchange transfusion in severe malaria? *J Infect*. 1999;39(3):185-186. http://www.ncbi.nlm.nih.gov/pubmed/10714792.

21. Zhang Y, Telleria L, Vinetz JM, Yawn D, Rossmann S, Indrikovs AJ. Erythrocytapheresis forPlasmodium falciparum infection complicated by cerebral malaria and hyperparasitemia. *J Clin Apher*. 2001;16(1):15-18. doi:10.1002/jca.1002.

22. Riddle MS, Jackson JL, Sanders JW, Blazes DL. Exchange Transfusion as an Adjunct Therapy in Severe Plasmodium falciparum Malaria: A Meta-analysis. *Mikrobiyol Bul*. 2012;46(3):493-498.

23. Bhakdi SC, Ottinger A, Somsri S, et al. Optimized high gradient magnetic separation for isolation of Plasmodium-infected red blood cells. *Malar J*. 2010;9:38.

24. Moore LR, Fujioka H, Williams PS, et al. Hemoglobin degradation in malaria-infected erythrocytes determined from live cell magnetophoresis. *FASEB J*. 2006;20(6):747-749.

25. Ribaut C, Berry A, Chevalley S, et al. Concentration and purification by magnetic separation of the erythrocytic stages of all human Plasmodium species. *Malar J*. 2008;7(1):45. doi:10.1186/1475-2875-7-45.

26. Pamme N, Wilhelm C. Continuous sorting of magnetic cells via on-chip free-flow magnetophoresis. *Lab Chip*. 2006;6(8):974. http://xlink.rsc.org/?DOI=b604542a.

27. Kang JH, Super M, Yung CW, et al. An extracorporeal blood-cleansing device for sepsis therapy. *Nat Med*. 2014;20(10):1211-1216. http://www.nature.com/doifinder/10.1038/nm.3640.

28. Brandl M, Mayer M, Hartmann J, Posnicek T, Fabian C, Falkenhagen D. Theoretical analysis of ferromagnetic microparticles in streaming liquid under the influence of external magnetic forces. *J Magn Magn Mater*. 2010;322(17):2454-2464. http://dx.doi.org/10.1016/j.jmmm.2010.02.056.

29. Furdui VI, Harrison DJ. Immunomagnetic T cell capture from blood for PCR analysis using microfluidic systems. *Lab Chip*. 2004;4(6):614-618.

30. Hayes MA, Polson NA, Phayre AN, Garcia AA. Flow-Based Microimmunoassay. *Anal Chem*. 2001;73(24):5896-5902.

31. Inglis DW, Riehn R, Austin RH, Sturm JC. Continuous microfluidic immunomagnetic cell separation. *Appl Phys Lett*. 2004;85(21):5093-5095.

32. Berger M, Castelino J, Huang R, Shah M, Austin RH. Design of a microfabricated magnetic cell separator. *Electrophoresis*. 2001;22(18):3883-3892.

33. Chen H, Bockenfeld D, Rempfer D, Kaminski MD, Rosengart AJ. Three-dimensional modeling of a portable medical device for magnetic separation of particles from biological fluids. *Phys Med Biol*. 2007;52(17):5205-5218. http://www.ncbi.nlm.nih.gov/pubmed/17762081.

34. Lim J, Lanni C, Evarts ER, Lanni F, Tilton RD, Majetich S a. Magnetophoresis of nanoparticles. *ACS Nano*. 2011;5(1):217-226.

35. Earhart CM, Wilson RJ, White RL, Pourmand N, Wang SX. Microfabricated magnetic sifter for high-throughput and high-gradient magnetic separation. *J Magn Magn Mater*. 2009;321(10):1436-1439.

36. Hahn YK, Jin Z, Kang JH, et al. Magnetophoretic immunoassay of allergen-specific IgE in an enhanced magnetic field gradient. *Anal Chem*. 2007;79(6):2214-2220. http://www.ncbi.nlm.nih.gov/pubmed/17288405.

37. Xia N, Hunt TP, Mayers BT, et al. Combined microfluidic-micromagnetic separation of living cells in continuous flow. *Biomed Microdevices*. 2006;8(4):299-308.

38. Yung CW, Fiering J, Mueller AJ, Ingber DE. Micromagnetic-microfluidic blood cleansing device. *Lab Chip*. 2009;9(9):1171-1177.

39. Kim KS, Park J-K. Magnetic force-based multiplexed immunoassay using superparamagnetic nanoparticles in microfluidic channel. *Lab Chip*. 2005;5(6):657-664.

40. Cowman AF, Crabb BS. Invasion of Red Blood Cells by Malaria Parasites. *Cell*. 2006;124(4):755-766. http://linkinghub.elsevier.com/retrieve/pii/S0092867406001814.

41. WHO. Malaria: Report By the Secretariat. In: *Sixty-Sixth World Health Assembly*. ; 2013:A66/21. doi:10.1080/00382167.1988.9630350.

42. Fedosov DA, Lei H, Caswell B, Suresh S, Karniadakis GE. Multiscale Modeling of Red Blood Cell Mechanics and Blood Flow in Malaria. *PLoS Comput Biol*. 2011;7(12):e1002270. http://dx.plos.org/10.1371/journal.pcbi.1002270.

43. Kilejian a. Characterization of a protein correlated with the production of knob-like protrusions on membranes of erythrocytes infected with Plasmodium falciparum. *Proc Natl Acad Sci U S A*. 1979;76(9):4650-4653. doi:10.1073/pnas.76.9.4650.

44. Moody A. Rapid Diagnostic Tests for Malaria Parasites Rapid Diagnostic Tests for Malaria Parasites. *Clin Microbiol Rev*. 2002;15(1):66-78. doi:10.1128/CMR.15.1.66.

45. Maltha J, Gillet P, Jacobs J. Malaria rapid diagnostic tests in endemic settings. *Clin Microbiol Infect*. 2013;19(5):399-407. doi:10.1111/1469-0691.12151.

46. Weissbuch I, Leiserowitz L. Interplay between malaria, crystalline hemozoin formation, and antimalarial drug action and design. *Chem Rev*. 2008;108(11):4899-4914. doi:10.1021/cr078274t.

47. White N. The Treatment of Malaria. *N Engl J Med*. 1996;335:800-806.

48. Bonington A, Davidson R, Winstanley P, Pasvol G. Fatal quinine cardiotoxicity in the treatment of falciparum malaria. *Trans R Soc Trop Med Hyg*. 1996;90:305-307.

49. White N. Clinical pharmacokinetics and pharmacodynamics of artemisinin and derivatives. *Trans R Soc Trop Med Hyg*. 1994;88(s1):41-43.

50. Gyr K, Speck B, Ritz R, Cornu P, Buckner C. Cerebral tropical malaria with blackwater fever: a current diagnostic and therapeutic problem. *Schweiz Med Wochenschr*. 1974;104:1628-1630.

51. Omodeo-Salè F, Motti A, Basilico N, Parapini S, Olliaro P, Taramelli D. Accelerated senescence of human erythrocytes cultured with Plasmodium falciparum. *Blood*. 2003;102(2):705-711. doi:10.1182/blood-2002-08-2437.

52. World Health Organization. *Guidelines for the Treatment of Malaria*. Geneva; 2006.

53. Alfandari S, Dixmier G, Guery B, Leroy O, Georges H, Beaucaire G. Exchange Transfusion for Severe Malaria. *Infection*. 2001;29(2):96-97. http://link.springer.com/10.1007/s15010-001-1040-y.

54. Boctor FN. Red blood cell exchange transfusion as an adjunct treatment for severe pediatric falciparum malaria, using automated or manual procedures. *Pediatrics*. 2005;116(4):e592-5. doi:10.1542/peds.2005-0314.

55. Deshpande A, Kalgutkar S, Udani S. Red cell exchange using cell separator (therapeutic erythrocytapheresis) in two children with acute severe malaria. *J Assoc Physicians India*. 2003;51(September):925-926. http://www.ncbi.nlm.nih.gov/entrez/query.fcgi?cmd=Retrieve&db=PubMed&dopt=Citation&list_uids=14710987.

56. Eisenträger A, Vella D, Griffiths IM. Particle capture efficiency in a multi-wire model for high gradient magnetic separation. *Appl Phys Lett*. 2014;105(3):33508. http://scitation.aip.org/content/aip/journal/apl/105/3/10.1063/1.4890965.

57. Miller K, Greensburg A, Campbell C. Treatment of Severe Malaria in the United States with a Continuous Infusion of Quinine Gluconate and Exchange Transfusion. *N Engl J Med*. 1989;321(2):65-70.

58. Molla S, de la Rubia J, Arriaga F, Fernandez MJ, Carpio N, Marty ML. Role of exchange transfusion in patients with severe Falciparum malaria: report of six cases. *heamatologica*. 2001;86(2):989-990.

59. Hoontrakoon S, Suputtamongkol Y. Exchange transfusion as an adjunct to the treatment of severe falciparum malaria. *Trop Med Int Heal*. 1998;3(2):156-161. http://www.ncbi.nlm.nih.gov/pubmed/1623091.

60. Reisinger E, Silly H, Smolle G, Krejs G. Exchange transfusion for severe falciparum malaria? (letter). *Infection*. 1992;20:174.

61. Burchard GD, Kröger J, Knobloch J, et al. Exchange blood transfusion in severe falciparum malaria: retrospective evaluation of 61 patients treated with, compared to 63 patients treated without, exchange transfusion. *Trop Med Int Health*. 1997;2(8):733-740. doi:10.1046/j.1365-3156.1997.d01-375.x.

62. Roth E, Brotman D, Vanderberg J, Schulman S. Malarial pigment-dependent error in the estimation of hemoglobin content in plasmodium-falciparuminfected red-cells - implications for metabolic and biochemical-studies of the erythrocytic phases of malaria,. *Am J Trop Med Hyg*. 1986;906-911(35).

63. Heidelberger M, Mayer MM, Demarest CR. Studies in Human Malaria: I. The Preparation of Vaccines and Suspensions Containing Plasmodia. *J Immunol*. 1946;52(4):325-330.

64. Oka T, Kanayama H, Fukui S, et al. Application of HTS bulk magnet system to the magnetic separation techniques for water purification. *Phys C Supercond its Appl*. 2008;468(15-20):2128-2132.

65. Nam J, Huang H, Lim H, Lim C, Shin S. Magnetic separation of malaria-infected red blood cells

in various developmental stages. *Anal Chem*. 2013;85(15):7316-7323.

66. Fuh CB, Tsai HY, Lai JZ. Development of magnetic split-flow thin fractionation for continuous particle separation. *Anal Chim Acta*. 2003;497:115-122. http://linkinghub.elsevier.com/retrieve/pii/S0003267003011000.

67. Sinha A, Ganguly R, De KA, Puri KI. Single magnetic particle dynamics in a microchannel. *Phys Fluids*. 2007;19(11):5-10.

68. Smistrup K, Lund-Olesen T, Hansen MF, Tang PT. Microfluidic magnetic separator using an array of soft magnetic elements. *J Appl Phys*. 2006;99(2006):100-102.

69. Pekas N, Granger M, Tondra M, Popple A, Porter MD. Magnetic particle diverter in an integrated microfluidic format. *J Magn Magn Mater*. 2005;293(1):584-588.

70. Kose AR, Fischer B, Mao L, Koser H. Label-free cellular manipulation and sorting via biocompatible ferrofluids. *Proc Natl Acad Sci U S A*. 2009;106(51):21478-21483.

71. Bu M, Christensen TB, Smistrup K, Wolff A, Hansen MF. Characterization of a microfluidic magnetic bead separator for high-throughput applications. *Sensors Actuators A Phys*. 2008;145-146:430-436. http://linkinghub.elsevier.com/retrieve/pii/S0924424707008953.

72. Deng T, Prentiss M, Whitesides GM. Fabrication of magnetic microfiltration systems using soft lithography. *Appl Phys Lett*. 2002;80(3):461-463.

73. Trang DTX, Huy NT, Kariu T, Tajima K, Kamei K. One-step concentration of malarial parasite-infected red blood cells and removal of contaminating white blood cells. *Malar J*. 2004;3(1):7. doi:10.1186/1475-2875-3-7.

74. Zborowski M, Ostera GR, Moore LR, Milliron S, Chalmers JJ, Schechter AN. Red blood cell magnetophoresis. *Biophys J*. 2003;84(4):2638-2645. http://dx.doi.org/10.1016/S0006-3495(03)75069-3.

75. Ahn SY, Shin MY, Kim Y a., et al. Magnetic separation: A highly effective method for synchronization of cultured erythrocytic Plasmodium falciparum. *Parasitol Res*. 2008;102(6):1195-1200.

76. Nalbandian RM, Sammons DW, Manley M, et al. A Molecular-based Magnet Test for Malaria. *Am J Clin Pathol*. 1995;103(1):57-64.

77. Owen CS. High gradient magnetic separation of erythrocytes. *Biophys J*. 1978;22(2):171-178. doi:10.1016/S0006-3495(78)85482-4.

78. Melville D, Paul F, Roath S. Direct magnetic separation of red cells from whole blood. 1975.

79. Paul F, Roath S, Melville D, Warhurst DC, Osisanya JOS. Separation of malaria-infected erythrocytes from whole blood: use of a selective high-gradient magnetic separation technique. *Lancet*. 1981;318(8237):70-71.

80. Graham MD. Efficiency comparison of two preparative mechanisms for magnetic separation of erythrocytes from whole blood. *J Appl Phys*. 1981;52(3):2578-2580.

81. Iliescu C, Xu G, Barbarini E, Avram M, Avram A. Microfluidic device for continuous magnetophoretic separation of white blood cells. *Microsyst Technol*. 2009;15(8):1157-1162.

82. Karl S, Davis TME, St Pierre TG. Parameterization of high magnetic field gradient fractionation columns for applications with Plasmodium falciparum infected human erythrocytes. *Malar J*.

2010;9:116. doi:10.1186/1475-2875-9-116.

83. Gulati S, Lall N. Hemodialysis in children: A simplified approach. *J Int Med Sci Acad*. 2012;25(2):101-105.

84. Leverett LB, Hellums JD, Alfrey CP, Lynch EC. Red Blood Cell Damage By Shear Stress. *Biophys J*. 1972;12:257-273. doi:10.1016/S0006-3495(72)86085-5.

85. Gandini A, Weinstein R, Sawh R, Parks D. Blood purification method and apparatus for the treatment of malaria. 2013.

86. Han K-H, Frazier AB. Paramagnetic capture mode magnetophoretic microseparator for high efficiency blood cell separations. *Lab Chip*. 2006;6(2):265-273.

87. Qu BY, Wu ZY, Fang F, Bai ZM, Yang DZ, Xu SK. A glass microfluidic chip for continuous blood cell sorting by a magnetic gradient without labeling. *Anal Bioanal Chem*. 2008;392(7-8):1317-1324. doi:10.1007/s00216-008-2382-4.

88. Takayasu M, Duske N, Ash SR, Friedlaender FJ. HGMS studies of blood cell behavior in plasma. *IEEE Tr*. 1982;18(6):1520-1522.

89. Granger RA. Chapter 10: Laminar Pipe Flow. In: *Fluid Mechanics*. ; 1985:481-540.

90. Wu W-T, Martin AB, Gandini A, Aubry N, Massoudi M, Antaki JF. Design of microfluidic channels for magnetic separation of malaria-infected red blood cells. *Microfluid Nanofluidics*. 2016;20(2):1-11. doi:10.1007/s10404-016-1707-4.

91. Link JM, Cuypers LA, Deen NG, Kuipers JAM. Flow regimes in a spout-fluid bed: A combined experimental and simulation study. *Chem Eng Sci*. 2005;60(13):3425-3442. doi:10.1016/j.ces.2005.01.027.

92. Rusche H, Issa RI. The Effect of Void age on the Drag Force on Particles, Droplets and Bubbles in Dispersed Two-Phase Flow. *Japanese Eur Two-Phase Flow Meet*. 2000;(1).

93. Cundall PA, Strack ODL. A Discrete Numerical Model for Granular Assemblies. *Geotechnique*. 1979;29(1):47-65.

94. Tsuji Y, Tanaka T, Ishida T. Lagrangian numerical simulation of plug flow of cohesionless particles in a horizontal pipe. *Powder Technol*. 1992;71(3):239-250. doi:10.1016/0032-5910(92)88030-L.

95. van der Hoef MA, Ye M, van Sint Annaland M, Andrews AT, Sundaresan S, Kuipers JAM. *Computational Fluid Dynamics*. Vol 31. Elsevier; 2006. doi:10.1016/S0065-2377(06)31002-2.

96. Han K-H, Frazier AB. Continuous magnetophoretic separation of blood cells in microdevice format. *J Appl Phys*. 2004;96(10):5797-5802.

97. Oshima S, Sankai Y. Improvement of the accuracy in the optical hematocrit measurement by optimizing mean optical path length. *Artif Organs*. 2009;33(9):749-756.

98. Dulińska I, Targosz M, Strojny W, et al. Stiffness of normal and pathological erythrocytes studied by means of atomic force microscopy. *J Biochem Biophys Methods*. 2006;66(1-3):1-11.

99. Dean D, Hemmer J, Vertegel A, Laberge M. Frictional Behavior of Individual Vascular Smooth Muscle Cells Assessed By Lateral Force Microscopy. *Materials (Basel)*. 2010;3(9):4668-4680.

100. Ye SH, Johnson CA, Woolley JR, et al. Simple surface modification of a titanium alloy with

silanated zwitterionic phosphorylcholine or sulfobetaine modifiers to reduce thrombogenicity. *Colloids Surfaces B Biointerfaces*. 2010;79(2):357-364. doi:10.1016/j.colsurfb.2010.04.018.

101. Hackett S, Hamzah J, Davis TME, St Pierre TG. Magnetic susceptibility of iron in malaria-infected red blood cells. *Biochim Biophys Acta - Mol Basis Dis*. 2009;1792(2):93-99. http://dx.doi.org/10.1016/j.bbadis.2008.11.001.

102. Coryell C, Stitt F, Pauling L. The magnetic properties and structure of ferrihemoglobin (methemoglobin) and some of its compounds. *J Am Chem Soc*. 1937;3(3):633. http://pubs.acs.org/doi/abs/10.1021/ja01283a012.

103. Kramer SL, Campbell CC, Moncrieff RE. Fulminant Plasmodium falciparum infection treated with exchange blood transfusion. *J Am Med Assoc*. 1983;249:244-245. doi:10.1001/jama.1983.03330260062034.

104. Boctor FN. Red blood cell exchange transfusion as an adjunct treatment for severe pediatric falciparum malaria, using automated or manual procedures. *Pediatrics*. 2005;116(4):e592-5. http://www.ncbi.nlm.nih.gov/pubmed/16166388.

105. Chotivanich K, Udomsangpetch R, Simpson J a, et al. Parasite multiplication potential and the severity of Falciparum malaria. *J Infect Dis*. 2000;181(3):1206-1209. doi:10.1086/315353.

106. Hall A. Exchange transfusion and quinine concentrations in falciparum malaria. *Br Med J*. 1985;291:1169-1170.

107. Macallan DC, Pocock M, Bishop E, et al. Automated erythrocytapheresis in the treatment of severe falciparum malaria. *J Infect*. 1999;39(3):233-236. http://www.ncbi.nlm.nih.gov/pubmed/10714802.

108. Chikov V, Kuznetsov A, S A. Single cell magnetophoresis and its diagnostic value. *J Magn Magn Mater 122*. 1993;122(1093):367-370.

109. Karl S, David M, Moore L, et al. Enhanced detection of gametocytes by magnetic deposition microscopy predicts higher potential for Plasmodium falciparum transmission. *Malar J*. 2008;7:66. doi:10.1186/1475-2875-7-66.

110. Fedosov D a., Dao M, Karniadakis GE, Suresh S. Computational biorheology of human blood flow in health and disease. *Ann Biomed Eng*. 2014;42(2):368-387.

111. Chotivanich K, Udomsangpetch R, Dondorp A, et al. The Mechanisms of Parasite Clearance after Antimalarial Treatment of Plasmodium falciparum Malaria. *J Infect Dis*. 2000;182(2):629-633. doi:10.1086/315718.

112. Karunajeewa H a. Parasite clearance after malaria therapy: staying a step ahead of drug resistance. *BMC Med*. 2015;13(1):251. doi:10.1186/s12916-015-0486-1.

113. White NJ. Assessment of the pharmacodynamic properties of antimalarial drugs in vivo. *Antimicrob Agents Chemother*. 1997;41(7):1413-1422.

114. ter Kuile F, Nosten F, Thieren M, et al. High dose mefloquine in the treatment of multidrug resistant falciparum malaria. *J Infec Dis*. 1992;166:1393-1400.

115. Shute P, Maryon M. A contribution to the problem of strains of human plasmodium. *Riv Malariol*. 1954;23:1-21.

116. Wiener A, Wexler I, Brancato G. Treatment of erythroblastosis fetalis by exchange transfusion. Statistical analysis of results. *J Pediatr*. 1954;5:546-568.

117. Mollison P, Engelfriet C, Contreras M. *Blood Transfusion in Clinical Medicine.* 10th ed. Oxford, Great Britain: Blackwell Science; 1997.

118. Morgan GJ, Mikhail M, Murray M. *Clinical Anesthesiology*. 3rd ed.; 2001.

119. Reverberi R, Reverberi L. Removal kinetics of exchange transfusion. *Blood Transfus*. 2007;5(2):93-101. doi:10.2450/2007.0018-07.

120. Banks AA of B. *Technical Manual of the American Association of Blood Banks*. 11th ed.; 1993.

121. Gravenor MB, van Hensbroek MB, Kwiatkowski D. Estimating sequestered parasite population dynamics in cerebral malaria. *Proc Natl Acad Sci U S A*. 1998;95(13):7620-7624. doi:10.1073/pnas.95.13.7620.

122. Furlani EP. Magnetophoretic separation of blood cells at the microscale. *J Phys D Appl Phys*. 2007;40(5):1313-1319. http://stacks.iop.org/0022-3727/40/i=5/a=001.

123. Jamiolkowski MA, Pedersen DD, Antaki JF, Wagner WR. Real-time analysis of flow-induced thrombus formation within defined crevices. In: *ASAIO Annual Conference*. Chicago, IL; 2015.

124. Wells RE, Marrill EW. Shear Rate Dependence of the Viscosity of Whole Blood and Plasma. *Science (80-)*. 2016;133(3455):763-764.

125. Chien S, Usami S, Dellenback R, Gregersen M. Blood viscosity: Influence of erythrocyte deformation. *Science (80-)*. 1967;157:827-829.

126. Brooks DE, Goodwin JW, Seaman G V. Interactions among erythrocytes under shear. *J Appl Physiol*. 1970;28(2):172-177.

127. Noland GS, Briones N, Sullivan DJ. The shape and size of hemozoin crystals distinguishes diverse Plasmodium species. *Mol Biochem Parasitol*. 2003;130(2):91-99. doi:10.1016/S0166-6851(03)00163-4.

APPENDIX A: FEMM simulation results and magnetic force plots for six permanent magnet arrays

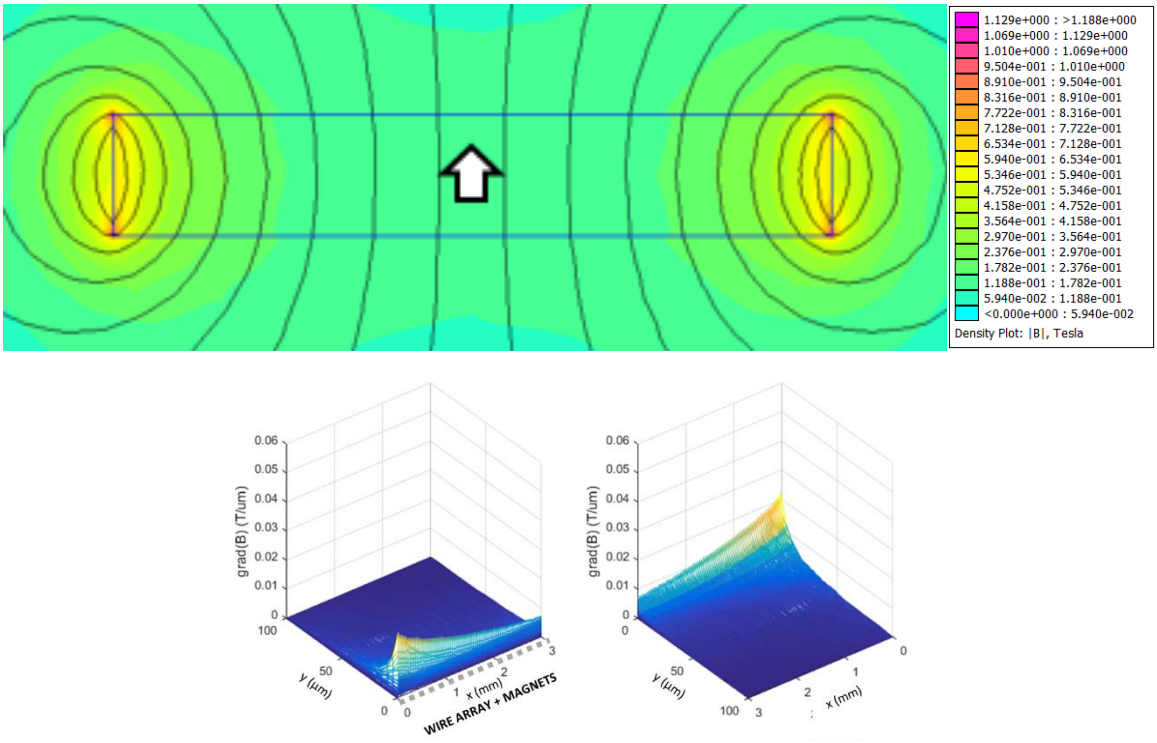

Single 76.2 mm x 12.7 mm N40 permanent magnet

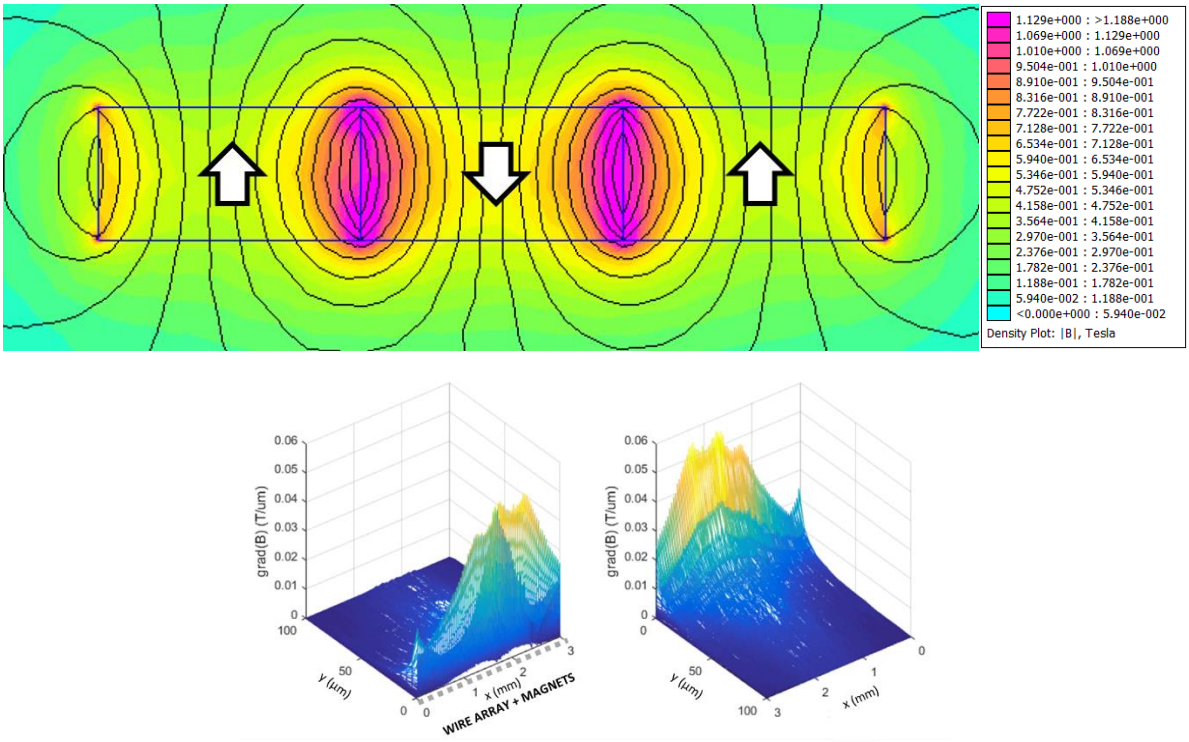

Three alternating 25.4 mm x 12.7 mm N40 permanent magnets

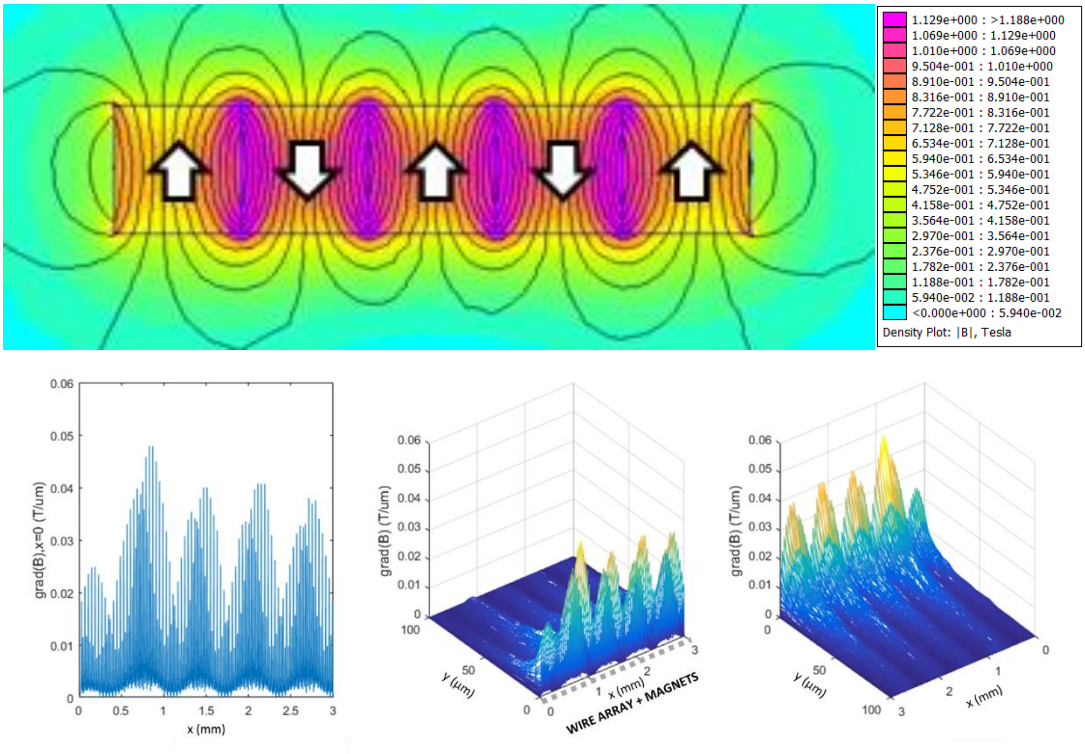

Five alternating 12.7 mm x 12.7 mm N40 permanent magnets

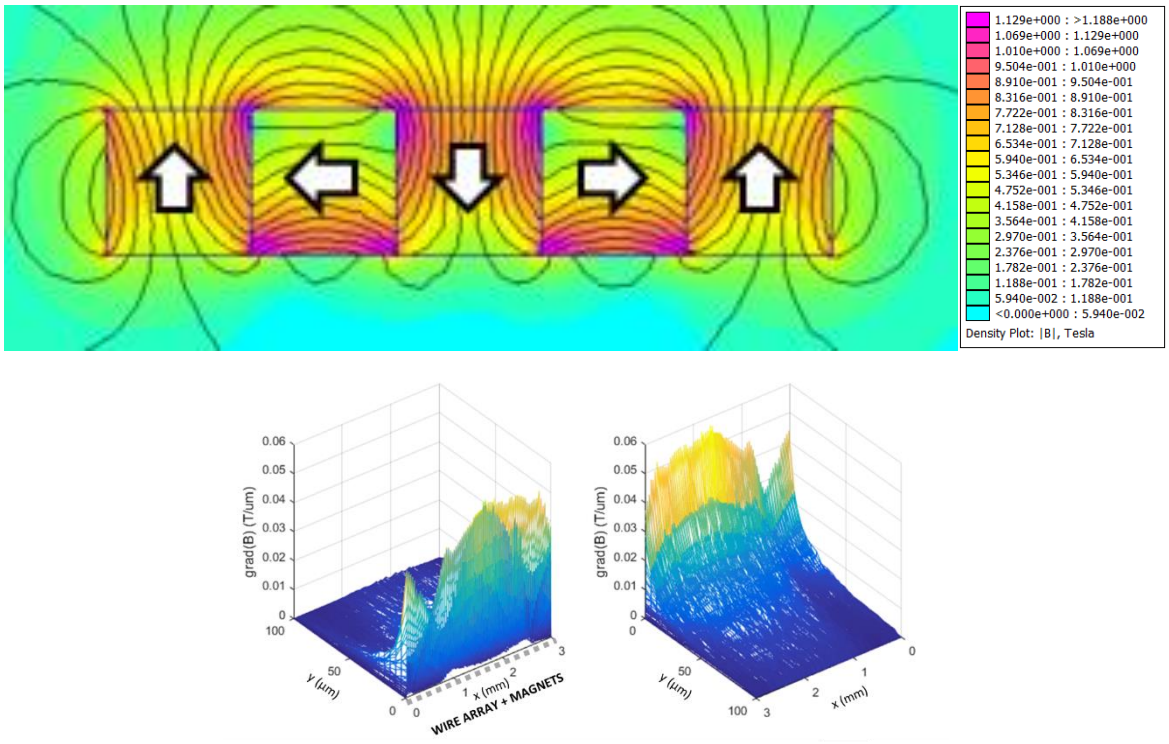

Five Hallbach-configuration 12.7 mm x 12.7 mm N40 permanent magnets

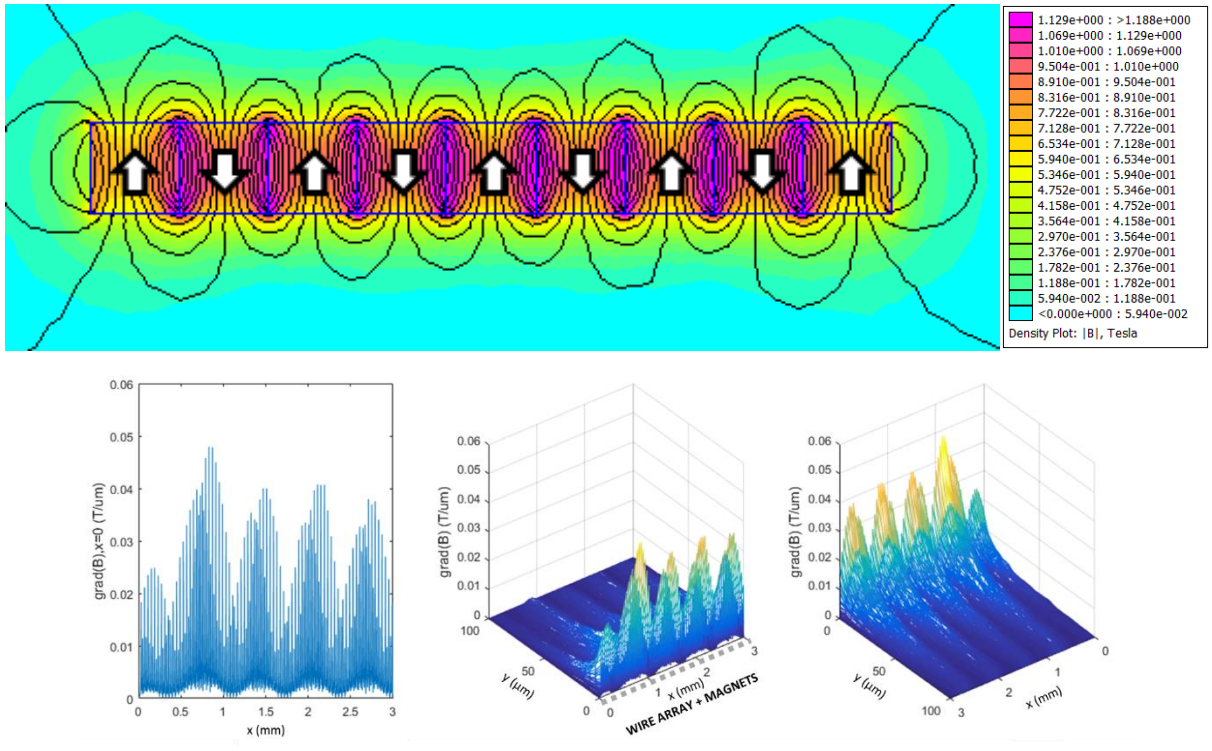

Nine alternating 6.3 mm x 6.3 mm N40 permanent magnets

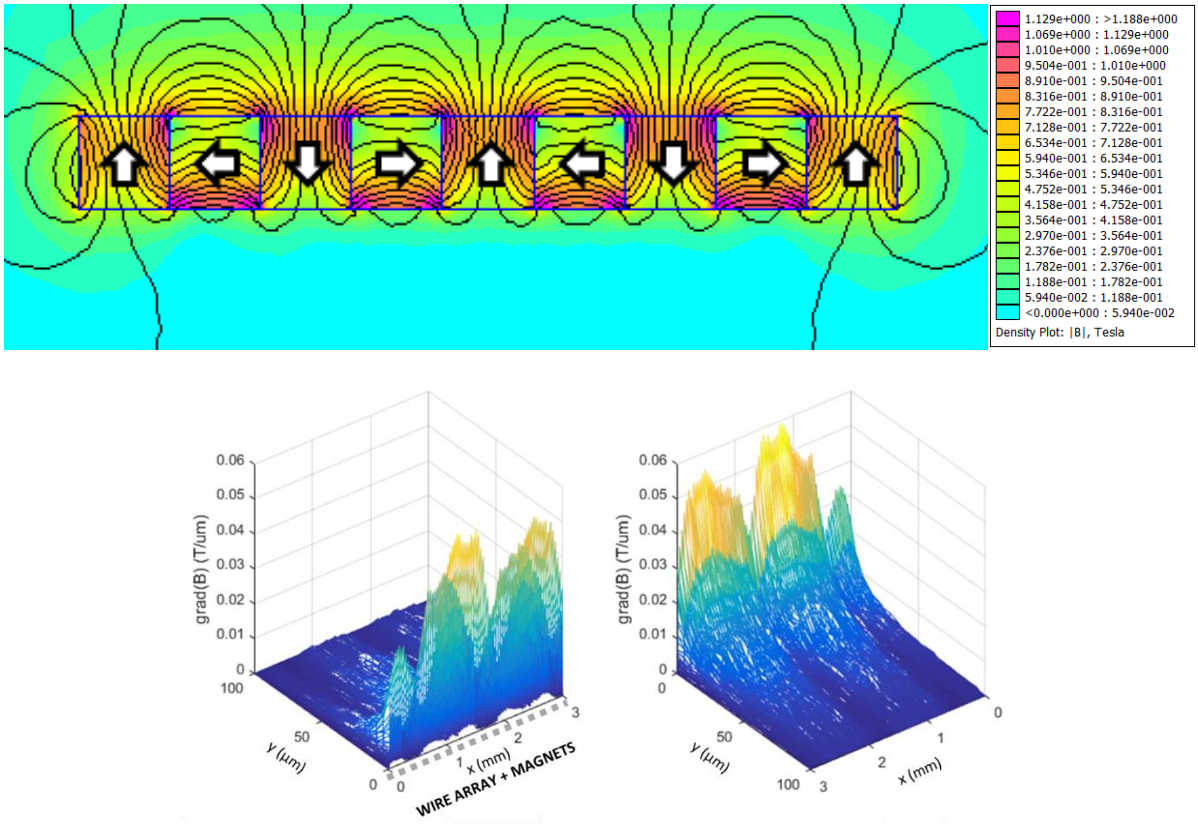

Nine Hallbach-configuration 6.3 mm x 6.3 mm N40 permanent magnets

APPENDIX B: Averaged conservation of mass (M) and RBC changes in outlet results for mesoscale mPharesis verification

N	Q (μL/min)	SR (%)	M,metRBCs (%)				M,hRBCs (%)			
			no magnet		magnet		no magnet		magnet	
			Avg	*Stdev*	Avg	*Stdev*	Avg	*Stdev*	Avg	*Stdev*
3	**39**	**10**	1.9	*0.3*	-30.3*	*0.7**	-3.1	*3.1*	-0.1	*1.1*
3	**154**		0.6	*0.6*	-4.4	*0.1*	1.3	*0.7*	1.6	*0.7*
3	**231**		3.3	*2.1*	-3.1	*0.5*	0.7	*2.3*	-0.1	*1.6*
3	**308**		-3.7	*0.6*	-2.8	*1.3*	-2.4	*1.4*	-0.1	*0.7*
3	**385**		-4.1	*1.1*	-2.2	*1.5*	-1.1	*0.9*	-0.9	*0.4*
3	**77**	**5**	0.1	*2.3*	-2.5	*0.4*	2.5	*1.7*	-1.6	*1.1*
21		**10**	-3.0	*3.1*	-1.9	*2.7*	1.5	*1.4*	-0.5	*2.2*
3		**20**	-1.3	*3.7*	2.5	*4.2*	-3.4	*0.9*	-1.3	*3.2*

N	Q (μL/min)	SR (%)	η_{remove}				η_{rescue}			
			no magnet		magnet		no magnet		magnet	
			Avg	*Stdev*	Avg	*Stdev*	Avg	*Stdev*	Avg	*Stdev*
3	**39**	**10**	0.7	*1.9*	39.0*	5.4*	98.3	*1.1*	95.9	*0.6*
3	**154**		-3.0	*1.1*	14.6	1.0	100.6	*1.4*	96.8	*0.7*
3	**231**		3.1	*0.4*	16.7	1.2	102.9	*0.8*	96.1	*1.3*
3	**308**		-2.2	*1.1*	15.0	1.8	99.4	*0.4*	96.5	*1.4*
3	**385**		3.1	*0.5*	11.5	0.3	98.3	*0.9*	96.2	*0.6*
3	**77**	**5**	0.4	*0.6*	7.2	0.3	99.2	*1.2*	96.3	*0.3*
21		**10**	1.6	*0.7*	27.0	2.2	100.3	*0.9*	97.8	*0.5*
3		**20**	3.0	*0.8*	21.8	1.7	98.5	*0.7*	96.3	*0.8*

*indicates conservation of mass for this condition is out of reasonable range

APPENDIX C: Stack Profile Data macro for ImageJ

```
// StackProfileData
// This ImageJ macro gets the profile of all slices in a stack
// and writes the data to the Results table, one column per slice.
//
// Version 1.0, 24-Sep-2010 Michael Schmid

macro "Stack profile Data" {
    if (!(selectionType()==0 || selectionType==5 || selectionType==6))
      exit("Line or Rectangle Selection Required");
    setBatchMode(true);

    run("Plot Profile");
    Plot.getValues(x, y);
    run("Clear Results");
    for (i=0; i<x.length; i++)
       setResult("x", i, x[i]);
    close();

    n = nSlices;
    for (slice=1; slice<=n; slice++) {
       showProgress(slice, n);
       setSlice(slice);
       profile = getProfile();
       sliceLabel = toString(slice);
       sliceData = split(getMetadata("Label"),"\n");
       if (sliceData.length>0) {
          line0 = sliceData[0];
          if (lengthOf(sliceLabel) > 0)
             sliceLabel = sliceLabel+ " ("+ line0 + ")";
       }
```

```
        for (i=0; i<profile.length; i++)
            setResult(sliceLabel, i, profile[i]);
    }
    setBatchMode(false);
    updateResults;
}
```

APPENDIX D: Matlab code to remove noise and simplify intensity plots for cell counts

```
clc
close all
clear all

%remove 1 and 2 point noise
data = importdata('Results.txt');
data = transpose(data);
[m,n] = size(data);
data = round(data./255);
[m,n] = size(data);

%recognize "inner tubes", 3 types
for p=1:m
   for q=1:n-7
   if data(p,q:q+7)==[1 1 1 0 0 1 1 1];
      data(p,q:q+7)=[1 0 0 0 0 0 0 0];
   else
   end
   end
end
for p=1:m
   for q=1:n-6
   if data(p,q:q+6)==[1 1 0 0 0 1 1];
      data(p,q:q+6)=[1 0 0 0 0 0 0];
   else
   end
   end
end
for p=1:m
```

```
    for q=1:n-5
    if data(p,q:q+5)==[1 1 0 0 1 1];
        data(p,q:q+5)=[1 0 0 0 0 0];
    else
    end
    end
end

%simplify cells from 9 pixels long to 3 long
 for p=1:m
    for q=1:n-8
    if sum(data(p,q:q+8))==9;
        data(p,q:q+8)=[1 0 0 0 0 0 0 0 0];
    else
    end
    end
end
for p=1:m
    for q=1:n-7
    if sum(data(p,q:q+7))==8;
        data(p,q:q+7)=[1 0 0 0 0 0 0 0];
    else
    end
    end
end
for p=1:m
    for q=1:n-6
    if sum(data(p,q:q+6))==7;
        data(p,q:q+6)=[1 0 0 0 0 0 0];
    else
    end
```

```
    end
end
for p=1:m
    for q=1:n-5
    if sum(data(p,q:q+5))==6;
        data(p,q:q+5)=[1 0 0 0 0 0];
    else
    end
    end
end
for p=1:m
    for q=1:n-4
    if sum(data(p,q:q+4))==5;
        data(p,q:q+4)=[1 0 0 0 0];
    else
    end
    end
end
for p=1:m
    for q=1:n-3
    if sum(data(p,q:q+3))==4;
        data(p,q:q+3)=[1 0 0 0];
    else
    end
    end
end
for p=1:m
    for q=1:n-2
    if sum(data(p,q:q+2))==3;
        data(p,q:q+2)=[1 0 0];
    else
```

```
    end
    end
end
for p=1:m
    for q=1:n-1
    if sum(data(p,q:q+1))==2;
        data(p,q:q+1)=[1 0];
    else
    end
    end
end

%bin data
B = ceil(m/10);

data_sum = sum(data,2);
data_tot_sum = [sum(data_sum(1:B,1))
sum(data_sum(B:2*B,1))
sum(data_sum(2*B:3*B,1))
sum(data_sum(3*B:4*B,1))
sum(data_sum(4*B:5*B,1))
sum(data_sum(5*B:6*B,1))
sum(data_sum(6*B:7*B,1))
sum(data_sum(7*B:8*B,1))
sum(data_sum(8*B:9*B,1))
sum(data_sum(9*B:m,1))]

%save to file
filename = 'smooth.xlsx';
xlswrite(filename,data);
```